University of Nottingham
UK | CHINA | MALAYSIA

The Structural Evolution of Galaxies at $z < 7$

Amy Nicole Whitney

Thesis submitted to the University of Nottingham
for the degree of Doctor of Philosophy

May 2021

Remember to look up at the stars and not down at your feet. Try to make sense of what you see and wonder about what makes the universe exist. Be curious. And however difficult life may seem, there is always something you can do and succeed at. It matters that you don't just give up.

– Stephen Hawking

Supervisors:	Prof. Christopher Conselice	
	Dr. James Bolton	
Examiners:	Dr. John Stott	(Lancaster University)
	Prof. Alfonso Aragón-Salamanca	(University of Nottingham)
Submitted:	28th May 2021	
Examined:	3rd August 2021	
Final version:	28th October 2021	

Contents

List of Tables

List of Figures

Abstract

This thesis utilises all five fields of the CANDELS survey to probe galaxy evolution out to redshift $z \sim 7$ in the context of size, surface brightness, and structure. Both the optical and ultraviolet (UV) rest-frames are used depending on the context.

We present a size analysis of a sample of $\sim$ 49,000 galaxies from the CANDELS GOODS-North and GOODS-South fields using redshift-independent relative surface brightness metrics to determine an unbiased measure of the differential size evolution of galaxies at $1 < z < 7$. We introduce a novel method for removing foreground objects from distant galaxy ($z > 3$) images that makes use of the Lyman break at 912 Å, in what we call '2D Lyman-break Imaging'. The images used are in the rest-frame optical at $z < 3$ and progressively bluer bands at $z > 3$. We separately consider a mass-selected sample (with masses in the range $10^9 M_\odot < M_* < 10^{10.5} M_\odot$) and a number density-selected sample (using a constant number density of $n = 1 \times 10^{-4}$ Mpc^{-3}).

We use the redshift-independent Petrosian radius as a proxy for size. We use different definitions of the Petrosian radius to measure the inner and outer radii to determine where size change occurs within a galaxy. The evolution of the measured size can be described by a power-law of the form $R_{\rm Petr} = \alpha(1+z)^\beta$ kpc where $\beta < 0$. We find that the outer radius increases more rapidly, suggesting that as a galaxy grows, mass is added to its outer regions via an inside-out growth mechanism. This growth is stronger for the number density selected sample, with the outer radii changing by a factor of ~ 3.4 compared to ~ 2.6 for the inner radii. We test and confirm these results using a series of image simulations.

Next, we investigate the rest-frame UV surface brightness (SB) evolution of galaxies up to $z \sim 6$ using a variety of deep *Hubble Space Telescope* (*HST*) imaging. We find a very strong evolution in the intrinsic SB distribution with a decrease of 4-5 mag arcsec^{-2} between $z = 6$ to $z = 1$. This change is much larger than expected in terms of the evolution in UV luminosity, sizes or dust extinction and we demonstrate that this evolution is 'unnatural' and due to selection biases. We also find no strong correlation

between mass and UV SB and thus, deep *HST* imaging is unable to discover all of the most massive galaxies in the distant universe. Through simulations we show that only $\sim$ 16% of galaxies that we can detect at $z = 2$ would be detected at high-z. We furthermore explore possible origins of high SB galaxies at high-z by investigating the relationship between intrinsic SB and star formation rates. We conclude that ultra-high SB galaxies are produced by very gas rich dense galaxies which are in a unique phase of evolution, possibly produced by mergers. Analogues of such galaxies do not exist in the relatively nearby universe.

Finally, we explore the quantitative non-parametric structural evolution of $\sim 16,000$ galaxies up to $z \sim 3$ in all five CANDELS fields. A fundamental feature of galaxies is their structure and how this evolves, yet we are just now deriving this evolution in quantitative ways. Our goal is to investigate how the structure changes with time with a focus on how the concentration and asymmetry of light evolve in the rest-frame optical.

To interpret our galaxy structure measurements, we also run and analyse 300 simulation realisations from IllustrisTNG to determine the timescale of mergers for the CAS system. We measure that from $z = 0 - 3$, the median asymmetry merger timescale is $0.56^{+0.23}_{-0.18}$ Gyr, and find it does not vary with redshift. Using these data, we find that galaxies become progressively asymmetric at a given mass at higher redshifts and we derive merger rates which scale as $\sim (1+z)^{1.87\pm0.04}$ Gyr^{-1}, which agrees well with recent machine learning and galaxy pair approaches, removing previous inconsistencies. We also show that far-infrared selected galaxies that are invisible to *HST* have a negligible effect on our measurements. Furthermore, we find that galaxies are more concentrated at higher redshifts. This is interpreted as a sign of how their formation occurs from a smaller initial galaxy that later grows into a larger one through mergers, consistent with the size growth of galaxies from 'inside-out', suggesting that the centres are the oldest parts of most galaxies.

Acknowledgements

First and foremost, I would like to thank Chris for being such a supportive supervisor. Without your guidance, encouragement, and helpful advice, the work I have completed over past three and a half years would not have been possible. I would also like to thank Jamie for your support, particularly over the past year.

There are many people I would like to thank for helping me get to this point and through my PhD; thank you to the Conselice group (CB, Leonardo, Sunny, Alex, Ulli, Florian, Rach) for all the insightful discussions during our group meetings. Thank you to the regular tea group (Lizzie, Simon, Tom, CB, Roan, Karel) for providing much needed breaks during the day and for the conversations about anything and everything. Thanks to the CC gang (Roan, CB, Kellie, Finlay, Charutha) firstly for teaching me how to do cryptic crosswords and also for the procrastination when work got tough. I would also like to thank everyone I shared B112 with over the years (CB, Roan, Alex, Joel, Benji, Daniela, Finlay, Charutha, Jake). I've enjoyed all our conversations both work-related and not. Taking part in the Inflativerse has been a highlight of my PhD; thank you to the team (Roan, CB, Kellie, Jake, Rachel, Tom), it's been so much fun working together and getting other people excited about astronomy has made all the hard work worth it.

I would also like to express my gratitude to my parents, grandparents, and extended family for always taking an interest in whatever it is I'm working on and trying to understand it. Thank you for encouraging me every step of the way, and always believing in me. Finally, I'd like to thank Sam for your unwavering support, patience, and giving me the confidence to keep going.

Published works

The majority of the material presented in this thesis has already been published in — or has been submitted to — a journal as the following three works.

I **Whitney A.**, Conselice C. J., Bhatawdekar R., Duncan K., 2019, ApJ, 887, 2: *'Unbiased Differential Size Evolution and the Inside-out Growth of Galaxies in the Deep CANDELS GOODS Fields at $1 \leq z \leq 7$'*.

II **Whitney A.**, Conselice C. J., Duncan K., Spitler L. R., 2020, ApJ, 903, 1: *'Surface Brightness Evolution of Galaxies in the CANDELS GOODS Fields up to $z \sim 6$: High-z Galaxies are Unique or Remain Undetected'*.

III **Whitney, A.**, Ferreira L., Conselice C. J., Duncan K., *submitted*: *Galaxy Evolution in all Five CANDELS Fields and IllustrisTNG: Morphological, Structural, and the Major Merger Evolution to $z \sim 3$*

Chapter 2 is based on material published in Paper I, Chapter 3 on that in Paper II, and Chapter 4 on that in Paper III.

The vast majority of work presented here was carried out by the author, with advice from the paper authors above. The photometric redshifts, stellar mass estimates, and star formation rates were determined by Kenneth Duncan. The IllustrisTNG simulations described in Chapter 4 were compiled by Leonardo Ferreira.

Chapter 1

Introduction

1.1 The Λ-CDM Cosmological Model

The Universe began 13.8 billion years ago with the Big Bang, a primordial singularity with infinite temperature and density. For a period of approximately 380,000 years following the Big Bang, the Universe expanded and all baryonic matter which was initially in a 'primordial soup' of protons, neutrons, electrons, and photons, cooled, allowing the formation of neutral atoms. Further cooling allowed the radiation field to decouple from the baryons. This process, known as recombination (Peebles, 1968a,b), allowed the cosmic microwave background (CMB) to propagate freely throughout the Universe. It is this radiation that reveals the initial conditions of the Universe.

The CMB was first discovered inadvertently in 1964 by Arno Penzias and Robert Wilson (Penzias & Wilson, 1965) and presented itself as a source of excess noise in radio wavelength observations. This excess noise was found to be uniform across the sky, no matter the time of day, and this discovery lead to the pair receiving the Nobel Prize in Physics in 1978. Since this initial measurement of the CMB, further, more

detailed measurements have been made; the Cosmic Microwave Background Explorer (COBE; Mather et al., 1990) satellite determined that the CMB is almost completely uniform in temperature, with extremely small fluctuations of $\Delta T/T \sim 10^{-5}$. The Wilkinson Microwave Anisotropy Probe (WMAP; Bennett et al., 2003) and Planck (Planck Collaboration et al., 2014) have confirmed and measured these anisotropies to extremely high precision. Figure 1.1 shows the increase in the angular resolution for each successive CMB satellite. Measurements of these CMB anisotropies from Planck (Planck Collaboration et al., 2014), along with angular diameter distances from measurements of baryon acoustic oscillations (BAO) from surveys like the 6dF Galaxy Survey (Beutler et al., 2011) and SDSS's Baryon Oscillation Spectroscopic Survey (BOSS; Alam et al., 2017), and luminosity distances from Type Ia supernovae such as those from the Pantheon sample (Scolnic et al., 2018), can be combined to give constraints on parameters for a scenario typically known as the Λ-Cold Dark Matter (Λ-CDM) model. This model predicts that the Universe is currently made up of 31.66 ± 0.84% matter, with the remaining percentage made up of an unknown entity known as dark energy (Λ) (Planck Collaboration et al., 2020). Of the ~30% matter, just 5% consists of visible stars, gas, and dust. 25% of matter is cold dark matter (CDM) which, like dark energy, is an unknown.

The anisotropies present in the CMB are a result of quantum fluctuations in the very early Universe and these primordial fluctuations had a key part to play in the formation of structure. Prior to recombination, the primordial elements (helium, deuterium, and lithium) were formed from the 'primordial soup' via big bang nucleosynthesis (Burles et al., 2001) and were coupled to the CMB. This radiation pressure prevented baryonic matter from collapsing. Dark matter, an unknown entity making up the majority of the matter in the Universe, was decoupled from the electromagnetic radiation and as such, was able to form small over-densities, known as dark-matter halos, around the

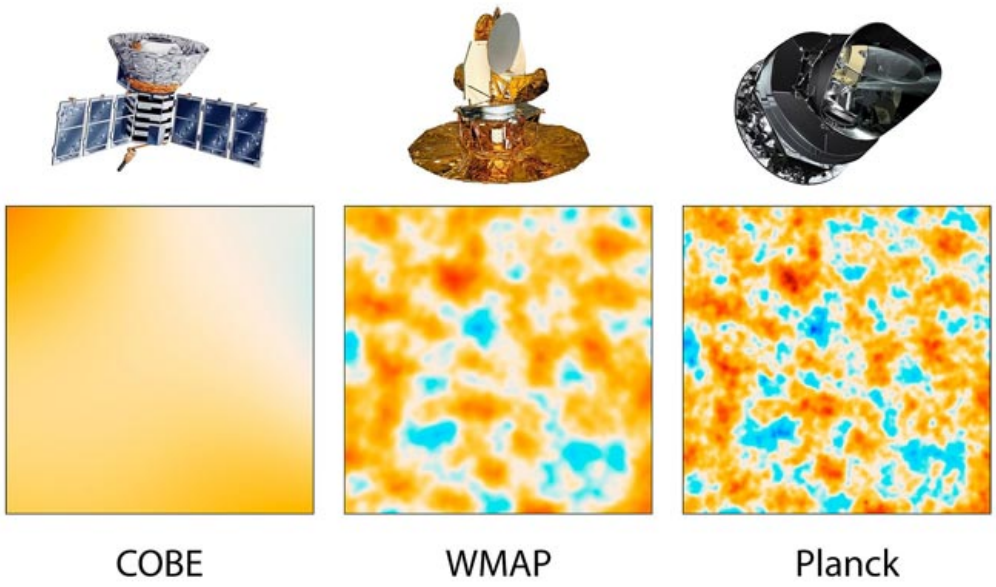

Figure 1.1: Illustration of the increase in precision and angular resolution of the anisotropies measured within the CMB by COBE (left), WMAP (centre), and Planck (right). The blue and red regions indicate the small variations in temperature of a fraction of a degree. Image credit: NASA/JPL-Caltech/ESA.

small fluctuations in density due to their own gravity. Recombination then allowed the baryonic matter to collapse under gravity and fall into the gravitational potentials created by the dark-matter halos. Thus began the several million year long 'Dark Ages' (Miralda-Escudé, 2003), so-called due to the lack of obvious sources of light. During this time, the over-densities continued to grow in a hierarchical manner, whereby the smaller halos collapsed first and merged together to form the larger halos. The baryonic matter that had fallen into these gravitational potentials was able to fall further into these dense regions by radiative cooling. This process gave rise to the filamentary structure seen in the distribution of galaxies and stars today. Eventually, the most dense concentrations of baryonic and non-baryonic matter had the conditions necessary for nuclear fusion and thus, the first stars and galaxies were born .

As these stars emitted ultraviolet (UV) radiation, the previously neutral intergalactic medium (IGM) was ionised during an era known as the Epoch of Reionisation (EoR).

This era began at $z \sim 15$ and ended at $z \sim 6$ and was the last major phase change of the Universe (Thomas et al., 2009; Kulkarni et al., 2017). The time frame for reionisation is most strongly constrained by the Gunn-Peterson trough seen in the spectra of distant quasars due to the presence of neutral hydrogen (Gunn & Peterson, 1965; Fan et al., 2006). Figure 1.2 shows the timeline of these events from the Big Bang, to the present day.

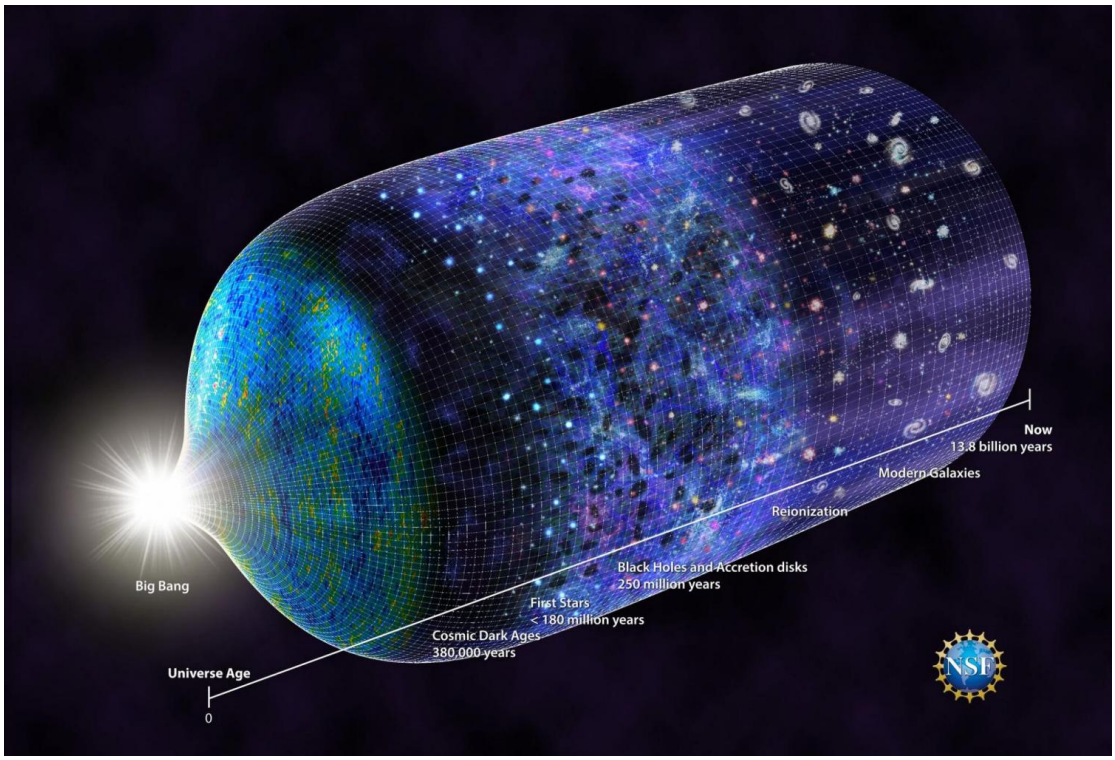

Figure 1.2: A timeline of the evolution of the Universe, showing the various stages. It starts with the Big Bang on the left, followed by the time period known as inflation where the Universe rapidly expanded. It then progresses to the Dark Ages 380,000 years after the formation of the Universe. Following that is the formation of the first stars, reionisation, and the formation of galaxies. It ends on the right with the present day, approximately 13.8 billion years after the Big Bang. This thesis focuses on the time period from the end of reionisation to the present day. Image credit: N.R. Fuller, National Science Foundation.

1.2 Galaxy Formation and Evolution Models

The hierarchical Λ-CDM model is the most widely accepted theory of structure formation within the Universe (White & Frenk, 1991), and there have been many attempts to recreate such a formation scenario using numerical simulations (e.g., Cole et al., 2000; Springel et al., 2005; Nelson et al., 2019a). Such simulations act as a bridge between the theory and observations. They provide the ability to track galaxies through time to help us to understand the physical processes that produce the galaxies seen today. It is possible to simulate galaxies as if they were imaged with specific instruments and telescopes, which allows comparisons to be made with observational results.

IllustrisTNG (Nelson et al., 2019a) is a recent suite of cosmological, gravo-magnetohydrodynamical simulations that have been used to model a number of galaxy properties and their evolution. Genel et al. (2018) use TNG100 to examine the evolution history of galaxy sizes with stellar mass, star formation rate, and redshift and compare the results to observations. The size-mass relation is found to be relatively flat up to $M_* = 10^{10.5}$ $M_\odot$ and steeper at higher masses. I explore this relation in §2.4.3 for a sample of galaxies in the CANDELS GOODS fields. For any given mass, the galaxies at lower redshifts are larger than their higher redshift counterparts. These results largely agree with observational results, such as those found by van der Wel et al. (2014). Along with observable quantities such as size, simulations can also be used in the context of morphological and structural parameters. For example, Huertas-Company et al. (2019) train a convolutional neural network (CNN) on the visual morphologies of galaxies at $z \sim 0$ in the Sloan Digital Sky Survey (SDSS) and applied the same network to a sample of 12,000 galaxies within the IllustrisTNG simulation that have been post-processed to appear as if they were from the same survey. The range of morphologies seen in the observational data is mirrored in the simulations.

The Evolution and Assembly of Galaxies and their Environments (EAGLE) simulation suite (Schaye et al., 2015; Crain et al., 2015) is another example of a cosmological hydrodynamical simulation. The simulation is in a box of size 100 Mpc h^{-1} on a side which contains 10,000 galaxies with a size equal to or greater than that of the Milky Way. Like IllustrisTNG, EAGLE has been used to examine galaxy properties; Furlong et al. (2017) determine the evolution of galaxy sizes from $z \sim 2$ to $z \sim 0$ for both passive and actively star forming galaxies within the simulation. The trends found in the size-mass relation are consistent with observations and are within 0.1 dex for $z < 1$ and 0.2-0.3 dex for $1 < z < 2$. The galaxy size is found to increase with decreasing redshift, as expected.

As simulations allow the tracking of individual galaxies within it, the state of a given galaxy is known at all times. As such, new techniques used to measure or identify stages of a galaxy's lifetime can be tested; Lotz et al. (2008) use GADGET hydrodynamical simulations (Springel et al., 2001) with the dust radiative transfer code SUNRISE (Jonsson, 2006) to create a sample of merging galaxies, the images of which are processed to match the specifications of SDSS g-band imaging. Quantitative measures of galaxy morphology such as asymmetry, concentration, Gini, and M_{20} and their dependence on a range of parameters, including the merger stage, are examined. The asymmetry is a measure of the degree to which the light within a galaxy is rotationally symmetric (Abraham et al., 1996; Conselice, 2003). Concentration is a measure of the ratio of two radii containing given fractions of the light within a galaxy Kent (1985). The Gini coefficient is the ratio of the distribution of light within a galaxy and a perfectly even flux distribution (Lotz et al., 2004). M_{20} is the second-order moment of the brightest 20% of a galaxy's flux (Lotz et al., 2004). I explore the asymmetry and concentration in more detail in Chapter 4. By identifying mergers in multiple ways, it is possible to determine the mean timescale for such mergers to occur, and the timescale is found

to depend on the method used to find mergers. These timescales can then be used to determine merger rates if a merger fraction has already been measured.

In summary, there are a wide range of simulations available and these simulations can be extremely useful for testing hypotheses. Observations make it possible to fine-tune the parameters the simulations are based upon and therefore gain further insight into the theory of galaxy formation.

1.3 Galaxy Detection

High-redshift galaxies are key to understanding galaxy evolution and there are multiple methods of for detecting such galaxies. One of the most popular is the Lyman-break method that makes use of the Lyman limit at 912 Å and was first implemented by Guhathakurta et al. (1990) and Steidel & Hamilton (1992). Light emitted at higher energies than this limit is absorbed by the neutral hydrogen gas surrounding star-forming galaxies and this causes the blue regions of a galaxy's spectral energy distribution (SED) to appear to be missing. This missing region is called the Lyman break. At higher redshifts the light is observed at longer, redder wavelengths. As such, the Lyman break occurs at redder wavelengths the higher the redshift, and an object will appear to drop-out in a certain filter. This can be used to identify high redshift galaxies by using images of galaxies in multiple filters. Figure 1.3 shows an example of a galaxy spectrum and how it appears in different *Hubble Space Telescope* (*HST*) filters.

Such a method revolutionised the detection and study of galaxies in the early Universe. Imaging of the Hubble Deep Field (HDF; Williams et al., 1996) and Hubble Deep Field South (HDF-S; Ferguson et al., 2000; Casertano et al., 2000) using the *HST* Wide Field and Planetary Camera 2 (WFPC2) allowed the detection of galaxies out to $z \sim 5$ (Madau et al., 1996). Further development of instruments aboard *HST* (e.g. the

Near-Infrared Camera and Multi-Object Spectrometer (NICMOS) and the Advanced Camera for Surveys (ACS)) pushed the detection of galaxies out to $z \sim 6$ (e.g., Bouwens et al., 2003; Thompson, 2003; Bunker et al., 2003; Stanway et al., 2004a,b).

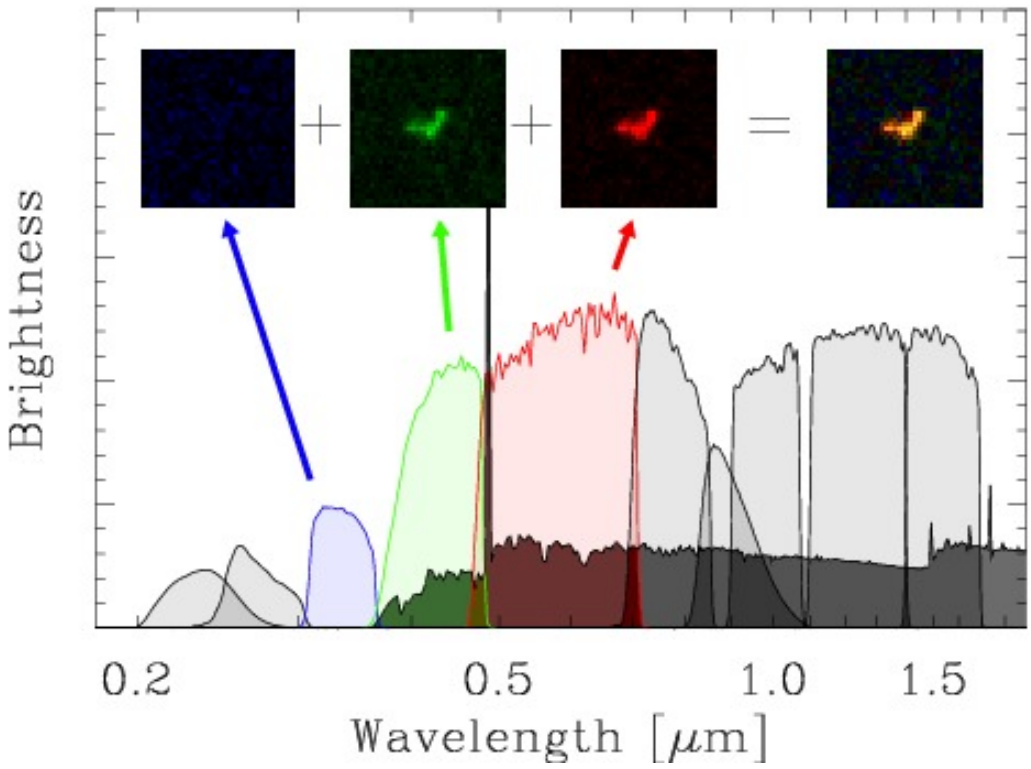

Figure 1.3: An example spectrum of a galaxy showing that the bluer wavelength light is absorbed and as such, the galaxy only appears in redder filters. Image credit: CANDELS Collaboration.

At higher redshifts, the Lyman break has been redshifted from optical to near-infrared wavelengths and as such, prior to the advent of instruments such as the Wide Field Camera 3 (WFC3) on *HST*, galaxy detections at $z > 6$ were limited. The infrared capabilities of this camera enabled the detection of galaxies out to $z \sim 7$ and beyond (e.g., Finkelstein et al., 2010; Wilkins et al., 2010; Oesch et al., 2010, 2012; Bouwens et al., 2010).

Another method of detecting high redshift galaxies is by the Lyman-α method. The neutral hydrogen atoms within the gas surrounding galaxies are ionised by the UV light

from ongoing star formation, creating Lyman-α absorption lines. This causes a break at a rest-frame wavelength of 1216 Å instead of at 912 Å as for the Lyman break due to the Lyman-α forest absorption for high-z galaxies. Galaxies can also be selected based on the redshifted Lyman-α emission lines and such galaxies are known as Lyman-α emitters. This technique was first suggested as an indication of young galaxies by Partridge & Peebles (1967).

Along with techniques such as the Lyman-break method, there are other factors that affect the detectability of a galaxy; for example, surface brightness effects will affect how well a galaxy can be observed. These effects are explored in Chapter 3.

1.4 Observable Properties of Galaxies

There are many properties that can be measured using available telescopes and instruments, and such properties can be used to infer the processes that galaxies undergo during their evolution.

1.4.1 Morphology

One of the first galaxy properties to be measured was morphology. Galaxies are broadly separated into two distinct classes; elliptical galaxies and spiral galaxies. Elliptical galaxies are primarily bulge-dominated and are ellipsoidal in shape. Spiral galaxies are typically disk-dominated and feature one or more spiral arms. These classifications were most famously visualised by Edwin Hubble (Hubble, 1926) in Hubble's 'tuning fork' diagram where galaxies lie on a sequence from the bulge-dominated ellipticals to disks, with a combination of the two in between. This schematic is shown in Figure 1.4, starting with elliptical galaxies on the left and progressing to the more disk-like

spiral galaxies on the right. The spiral category is separated further into pure spirals and those with a bar through the central bulge. However, this Hubble sequence is not representative of all galaxy populations. Some galaxies fit neither the elliptical or spiral definition and are known as irregular or peculiar galaxies. Such galaxies have many components such as tails and irregular structure and they are typically associated with interactions and mergers with other galaxies (Toomre & Toomre, 1972; Schweizer, 1982). In Chapter 4, I explore a non-parametric measure of structure and morphology for a sample of galaxies at $0.5 < z < 3$ within all five CANDELS fields.

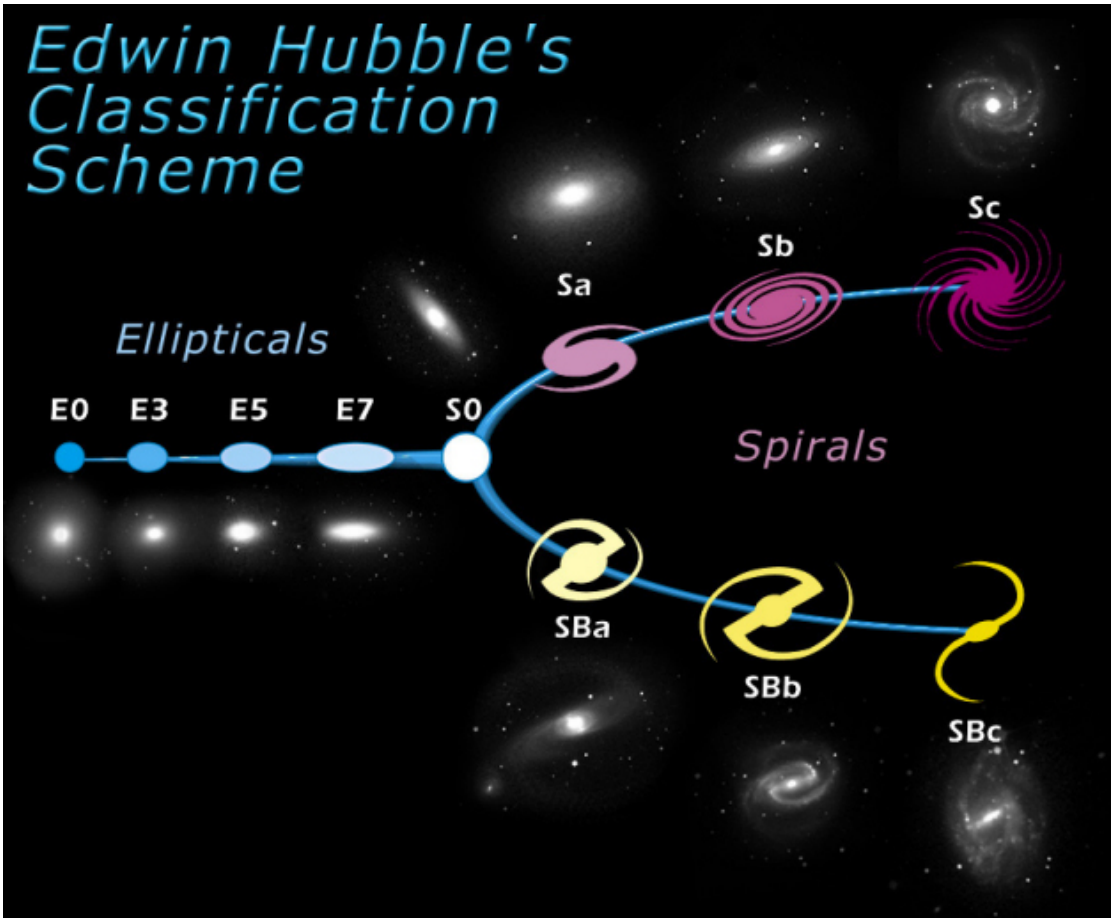

Figure 1.4: An example of the Hubble 'tuning fork' showing the two broad galaxy classifications beginning with elliptical galaxies on the left and becoming more disk-like to the right. The spiral galaxies are split into two further categories; spirals with many spiral arms and spirals with a bar and two spiral arms. Image credit: NASA & ESA.

1.4.2 Colour

Along with morphology, galaxies also display a wide range of colours, a property that is defined by the ratio of the galaxy's flux or luminosity in two different photometric filters. Colour is closely linked to galaxy morphology whereby early-type galaxies, which include ellipticals and lenticulars, typically appear redder than late-type galaxies, which include spirals and peculiars. Therefore, an early-type galaxy will have a higher luminosity in a redder, longer wavelength filter than a bluer, shorter wavelength filter (Roberts & Haynes, 1994). This bimodality can be seen in a galaxy colour-magnitude diagram, an example of which is shown in Figure 1.5; the two groups - the red sequence, home to early-type galaxies and the blue cloud, home to late-type galaxies - are easily distinguishable.

The observed colour is also indicative of the age of stellar populations within a galaxy; redder, early-type galaxies tend to be older compared to the bluer, late-type galaxies. Therefore, early-type galaxies must have ceased their star formation earlier than late-type galaxies. This difference in colour, and therefore age, suggests a difference in the process and formation histories between the two types. By examining various galaxy properties, it is possible to begin to determine the cause of these differences.

1.4.3 Size

Galaxy size is one of the simplest properties to measure, and can be taken directly from galaxy images. The evolution of galaxy size is important in understanding the processes that galaxies undergo to produce the galaxies we see today. Size has been shown to increase with time, primarily by measuring the effective radius of a sample of galaxies. Studies using the *Hubble Space Telescope's* Advanced Camera for Surveys and Near Infrared Camera and Multi-Object Spectrometer have shown that there is strong

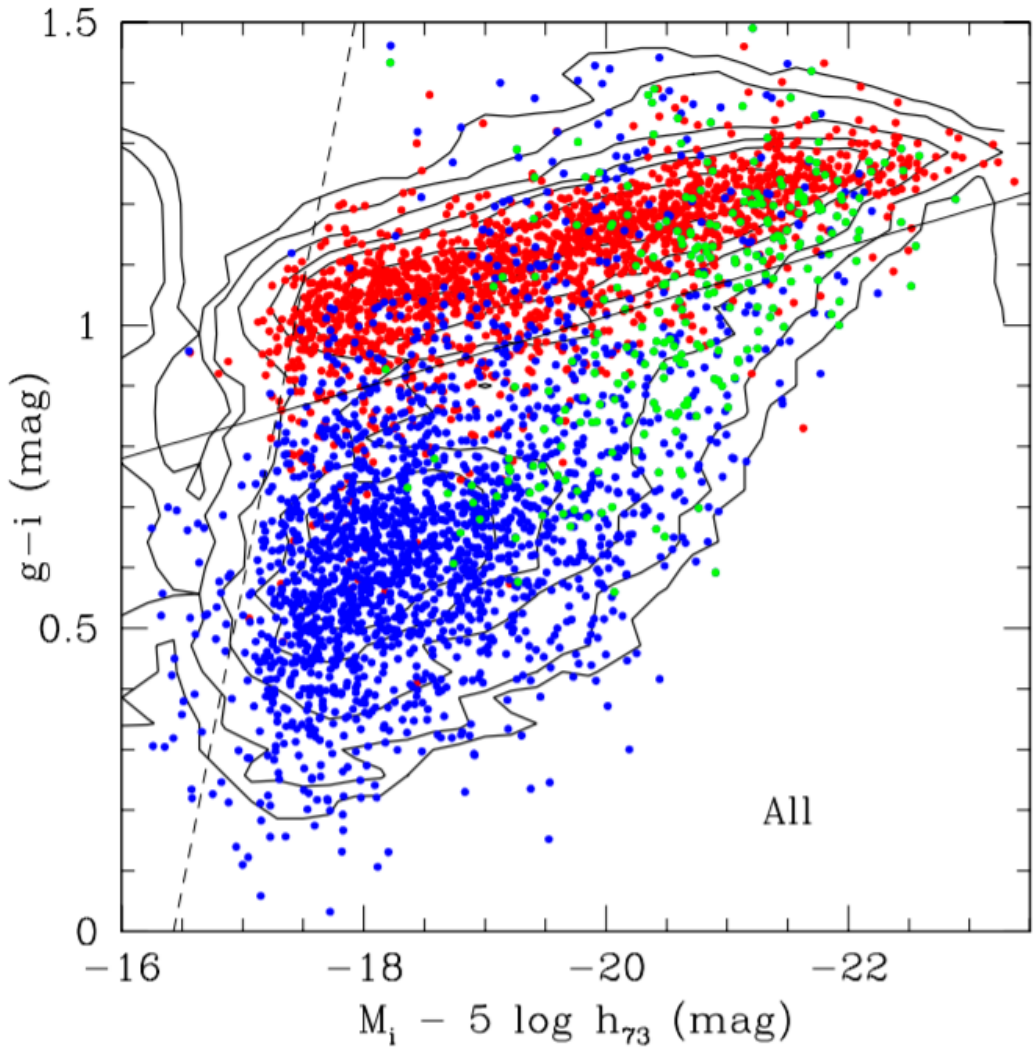

Figure 1.5: Colour ($g - i$) vs i-band absolute magnitude for galaxies from SSDS DR7 within the Coma supercluster. Each galaxy is coded depending on its morphological type with early-type galaxies in red and late-type galaxies in blue. Green points indicate bulge-dominated galaxies. The two types can be easily distinguished as two separate groups; the red sequence and the blue cloud. Figure from Gavazzi et al. (2010).

evolution of the effective radius since $z \sim 3$ (Trujillo et al., 2007; Buitrago et al., 2008; Cassata et al., 2013). Other studies involving the CANDELS survey have also shown this evolution (Buitrago et al., 2008; Bruce et al., 2012; Buitrago et al., 2013; Patel et al., 2013; van der Wel et al., 2014). Along with space based observations, ground based observations also show such an evolution (van Dokkum et al., 2010; Carrasco et al.,

2010). Although these previous works show an evolution, the factor by which the size changes across this redshift range of $0 < z < 3$ varies between a factor of 2 (van der Wel et al., 2008) and a factor of ∼7 (Buitrago et al., 2008).

Once higher redshifts are reached, the size evolution becomes less steep compared to that seen at lower redshifts. The size is found to evolve as $(1 + z)^{\beta}$ up to $z \sim 7$ where $\beta \simeq 1$ (Bouwens et al., 2004; Oesch et al., 2010; Straatman et al., 2015; Curtis-Lake et al., 2016; Allen et al., 2017). The effect of galaxy mass has also been explored; massive galaxies are more compact at higher redshifts than those of a similar mass at low redshift (Ferguson et al., 2004; Cimatti et al., 2008).

This observed size evolution is thought to be due to the accretion of gas and dust from the intergalactic medium and through the merging with other galaxies (e.g., Ferreras et al., 2009; López-Sanjuan et al., 2012). Accretion has been found to be the most significant formation scenario amongst massive galaxies (Conselice et al., 2013; Ownsworth et al., 2016) and mergers have been suggested to be the predominant cause of the size growth of massive galaxies (Bluck et al., 2012). Simulations also confirm that mergers are a significant cause for galaxy growth (e.g., Wellons et al., 2016).

Previous works use the effective, or half-light, radius as a measure of size. However, such measurements can be subject to biases as a result of redshift and cosmological dimming. These issues can be resolved by instead using the redshift-independent Petrosian radius that is determined by the ratio of the surface brightness at a given radius to the surface brightness within that radius (e.g., Bershady et al., 2000; Conselice, 2003). This method of measuring size allows us to probe where in the galaxy the size grows the most and can indicate how galaxies grow with time.

In Chapter 2, I explore this size evolution using the Petrosian radius, a redshift-independent measure of size, for a sample of mass-selected galaxies and a sample of

number density-selected galaxies at $1 < z < 7$ within the GOODS-North and GOODS-South fields of the CANDELS survey, and examine possible causes for the observed evolution (Whitney et al., 2019)

1.4.4 Surface Brightness

Galaxy surface brightness, a measure of luminosity per unit area, has previously been studied at low redshifts in both the optical and near-infrared (e.g., Schade et al., 1995; Roche et al., 1998; Labbé et al., 2003; Barden et al., 2005). The advent of larger and deeper surveys like CANDELS provide the ability to look to higher redshifts to explore the surface brightness evolution in the early Universe. The results of the low redshift studies have been varied and there is no consensus as to how the evolution of surface brightness occurs. Schade et al. (1996) examine a sample of galaxies using ground-based imaging and find a relatively strong evolution of 1.6 mag since $z \sim 1$. Other works such as those conducted by Schade et al. (1995), Lilly et al. (1998), Roche et al. (1998) and Barden et al. (2005) use *Hubble Space Telescope* observations and find a slightly shallower but similar evolution in the surface brightness of 1 mag since $z \sim 1$. These results are confirmed by models; Bouwens & Silk (2002) model disk evolution in two ways, with both suggesting that the surface brightness changes by 1.5 mag since $z \sim 1$. Other studies argue that selection effects must be taken into account when examining this evolution; Simard et al. (1999) initially find a change of 1.3 mag over the same redshift range. However, once selection effects are considered, no evolution is found in the surface brightness. Ravindranath et al. (2004) find similar results; a change of < 0.4 mag over $0.2 < z < 1.25$ for disk-like galaxies is found.

These works are limited to the optical rest-frame however, there is important information to be gleaned from other wavelengths such as the UV. Surface brightness in the

UV has been shown to correlate with star formation and gas densities (Schmidt, 1959; Kennicutt, 1998) and so can be used to determine how these parameters evolve with cosmic time.

In Chapter 3, I examine the evolution of the surface brightness and its relationship with star formation for a mass-selected sample of galaxies at $1 < z < 6$ within the GOODS-North and GOODS-South fields of the CANDELS survey. I also explore the effects of incompleteness and galaxy detectability on the results (Whitney et al., 2020).

1.4.5 Luminosity Function

Another crucial measurement is to ascertain the number of galaxies per luminosity bin; the luminosity function (LF). By determining how the LF evolves with time and luminosity, insight into the star formation histories of galaxies can be gained. It can also help to better understand reionisation; studies of extremely high redshift galaxies suggest the population of faint galaxies at these redshifts that dominate the LF are good candidates for the driving force behind reionisation (e.g., McLure et al., 2013). The luminosity function for Lyman break galaxies is typically measured at $\lambda_{\rm rest} \sim 1500$ Å or $\lambda_{\rm rest} \sim 1600$ Å.

The UV luminosity function is well fit by a Schechter function (Schechter, 1976) of the form

$$\phi(L) = \phi^* \left(\frac{L}{L^*}\right)^{\alpha} \exp\left(-\frac{L}{L^*}\right). \tag{1.1}$$

This function can also be expressed in log space as

$$\phi(M) = 0.4\ln(10)\phi^* 10^{-0.4(M-M^*)(\alpha+1)} \exp\left(-10^{-0.4(M-M^*)}\right) \tag{1.2}$$

where ϕ^* is a normalisation factor, M^* is the characteristic magnitude where the function turns over from a power law into an exponential, and α is the faint-end slope of the luminosity function. This value is typically negative, suggesting there is an abundance of galaxies with low luminosities. Figure 1.6 shows an example luminosity function fit with a Schechter function and how it evolves with redshift.

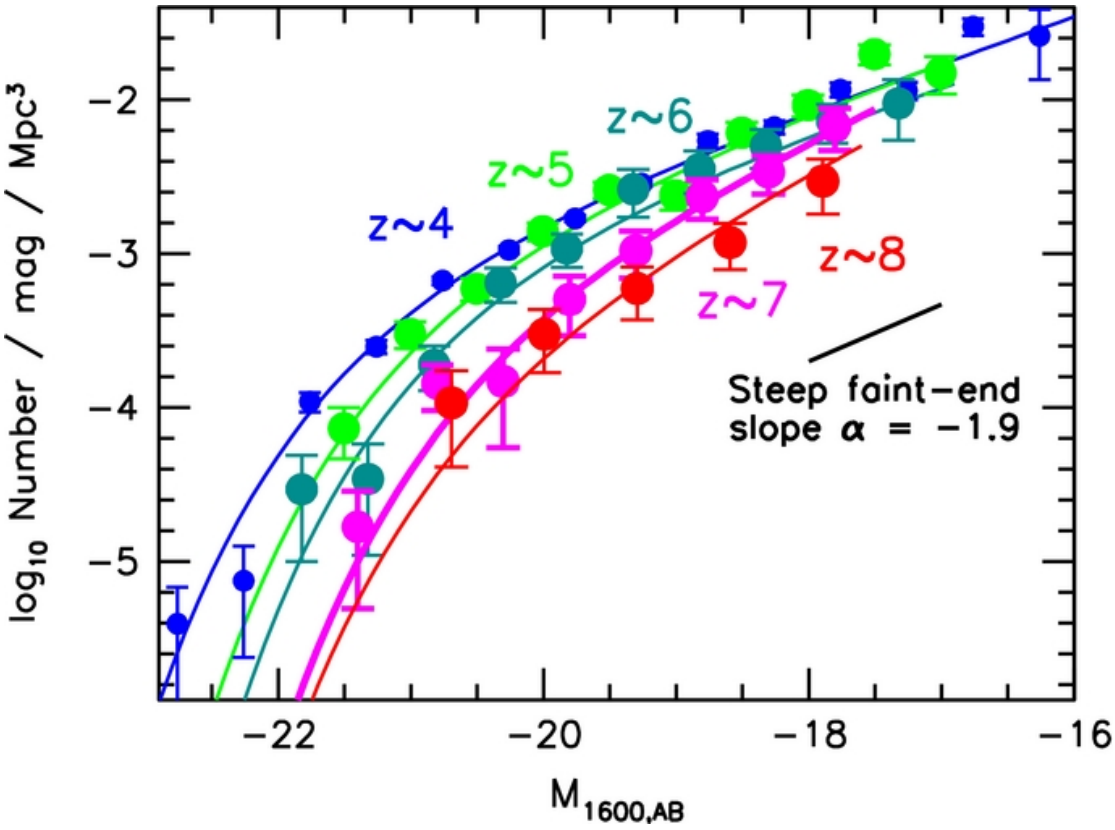

Figure 1.6: Evolution of the ultraviolet luminosity function from $z \sim 4$ to $z \sim 8$. Each redshift is fit with a Schechter function (solid lines), given in Equation 1.2. This fit shows the steep faint-end slope, indicating that there is a considerable contribution from low luminosity galaxies. It also shows the steepening of the faint-end slope as redshift increases. Figure from Bouwens et al. (2012).

The UV luminosity function has been shown to evolve with a steeper faint end slope at higher redshift (shown in Figure 1.6) and a non-linear change in the characteristic magnitude, whereby there is a brightening of the characteristic magnitude with cosmic time (e.g., Arnouts et al., 2005; Bouwens et al., 2006; McLure et al., 2009; Bouwens

et al., 2015).

1.4.6 Star Formation Rate Density

Another measurement that can provide information about the history of the Universe is the star formation rate density. Through observations of the star formation rate density, it has been shown that star formation peaked at $z \sim 2-3$, approximately two to three billion years after the Big Bang, as shown in Figure 1.7. These star formation rate density measurements, along with measurements of the stellar mass density, indicates that the majority of stellar mass was formed after $z \sim 2$ (Madau & Dickinson, 2014).

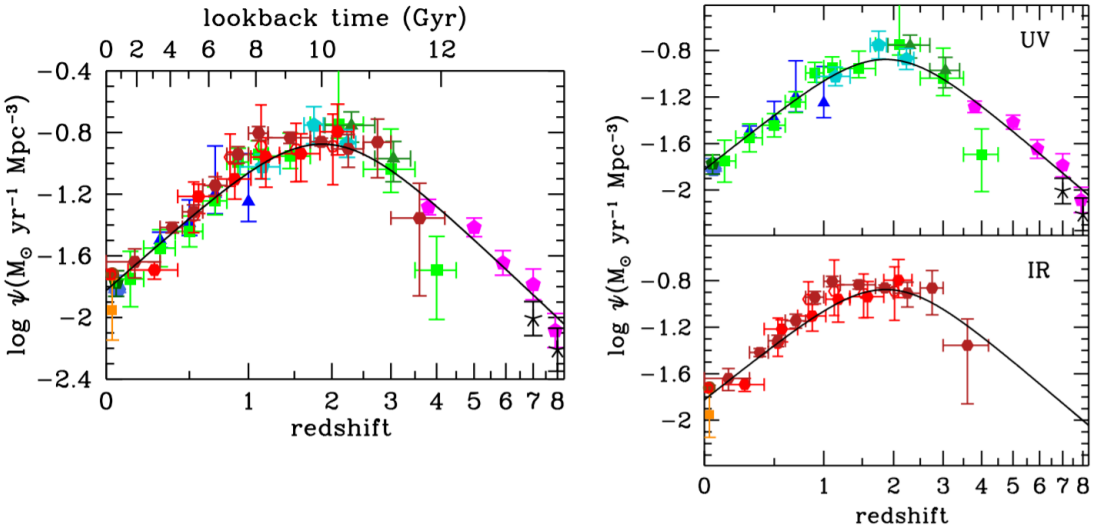

Figure 1.7: History of cosmic star formation in ultraviolet (top right panel), infrared (bottom right panel) and a combination of the two (left panel). The solid line in each panel indicates the best fit to the star formation rate density. Figure from Madau & Dickinson (2014), see the references therein for individual data points.

1.4.7 Galaxy Mergers

The way in which galaxy mass is assembled is an important piece of the galaxy formation puzzle. It is known to happen in two different ways; by the accretion of gas from the surrounding environment, and through the merging and interacting of galaxies. Mergers are direct evidence for the hierarchical assembly of structure in the Universe where galaxies and dark matter halos coalesce to form more massive systems. Merger fractions and rates can provide insight into the state of the Universe at particular redshifts, and give a better understanding of galaxy evolution. Mergers are typically identified in two ways. One such method is to find pairs of galaxies that are close together in terms of redshift and angular separation. This has enabled merger fractions and rates to be determined at a range of redshifts (e.g., Bluck et al., 2009, 2012; Mundy et al., 2017; Duncan et al., 2019). Another method used to identify mergers is to select galaxies that exhibit signs consistent with morphological disturbances (e.g., Conselice et al., 2003; Lotz et al., 2011). It is also possible to identify mergers using Deep Learning methods (Ferreira et al., 2020). Merger fractions and rates have been shown to decrease with cosmic time using multiple methods of merger identification. A comparison of the merger rates and fractions determined using different methods is shown in Figure 1.8.

In Chapter 4 of this thesis, I examine the evolution of the merger fraction and rate in more detail using the non-parametric method of identifying galaxies by their asymmetry.

1.5 The CANDELS Survey

The *Hubble Space Telescope* (*HST*) has played a key part in the study of galaxy formation and evolution. It has been able to observe areas of the sky, such as the The Great Observatories Origins Deep Survey (GOODS) fields (Giavalisco et al., 2004) to great

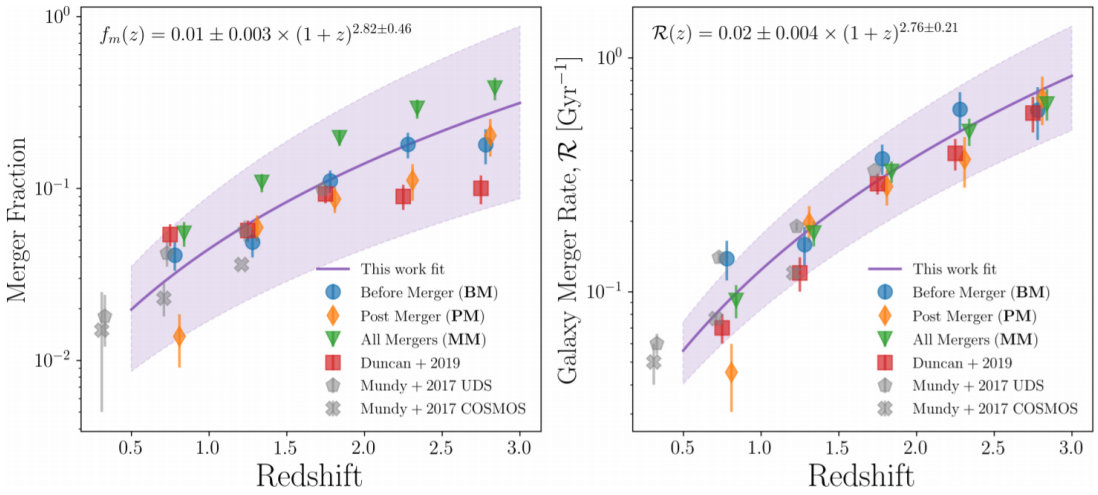

Figure 1.8: Evolution of the merger fraction (left) and merger rate (right) for a sample of galaxies in the CANDELS fields. Mergers are identified using a convolutional neural network trained on simulated galaxies from the IllustrisTNG cosmological simulation. The galaxies are identified as being either pre-merger (blue circles) or post-merger (yellow diamonds). These two categories are combined into one large category of a merger in any state (green triangles). The purple line of best-fit is fit to all three categories, and the purple region surrounding this fit is one standard deviation from the fit. Also shown are a comparison of results from other works that use different methods to identify mergers. Figure from Ferreira et al. (2020), see the references therein for individual data points.

depths and at a range of wavelengths. However, the GOODS-North and GOODS-South fields only cover a relatively small region of the sky (~320 arcmin^2) which leads to inaccurate galaxy counts due to cosmic variance.

Hubble's Advanced Camera for Surveys (ACS) was designed to survey large areas of the sky at optical wavelengths and is 10 times more efficient than its predecessor, the Wide Field Camera 2 (WFC2). It allowed the detection of galaxies out to $z \sim 6$ using the Lyman break selection technique and provided morphologies in the rest-frame optical at lower redshifts. However, near-infrared observations are required to do the same at higher redshifts. The NICMOS camera enabled the extension of observations of galaxies into the near-infrared, however the efficiency was not comparable to the optical observations of ACS. The GOODS NICMOS Survey (GNS; Conselice et al., 2011a)

observed 45 arcmin^2 of the GOODS fields in a single filter to a depth of $H_{AB} \approx 26.5$ and required 180 *HST* orbits in order to do so. The Wide Field Camera 3 (WFC3/IR) greatly improves on the capabilities of the NICMOS camera. It enables the detection of galaxies in the near-infrared at an efficiency comparable to that of ACS and to depths of $H_{AB} \gtrsim 27.1$ mag and $J_{AB} \gtrsim 27.0$ mag across the two filters, and requires half the orbits of the NICMOS camera.

Figure 1.9 shows a comparison between each of the instruments aboard *HST* in terms of the wavelengths covered and the discovery efficiency (defined as the system throughput multiplied by the field of view area).

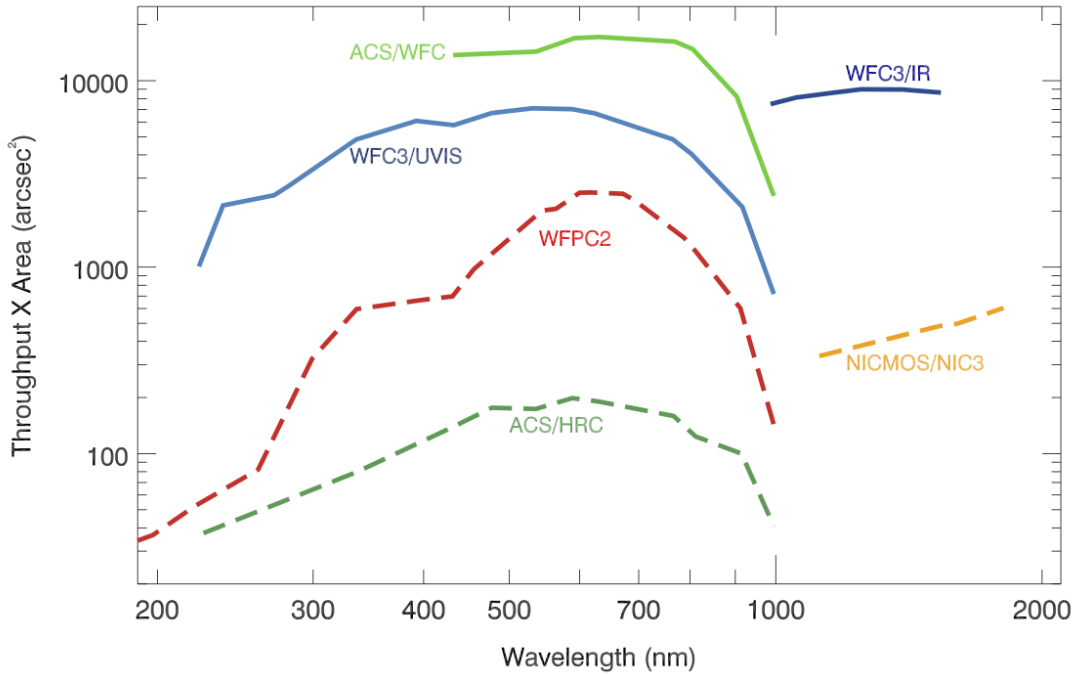

Figure 1.9: *Hubble Space Telescope* detector discovery efficiencies (system throughput multiplied by the field of view area). Image credit: STScI/Space Telescope Science Institute.

Making use of the greater efficiency of WFC3, along with the ACS, the Cosmic Assembly Near-infrared Deep Extragalactic Legacy Survey (CANDELS; Grogin et al., 2011; Koekemoer et al., 2011), a Multi-Cycle Treasury program awarded 902 orbits

of *Hubble* time, was designed to document the first third of galactic evolution over the redshift range $1.5 < z < 8$. The Cosmic Assembly Near-infrared Deep Extragalactic Legacy Survey covers a total of ~800 armin^2 across five separate fields; GOODS-North, GOODS-South, the COSMOS field (Scoville et al., 2007), the Extended Groth Strip (EGS; Davis et al., 2007), and the UKIDSS Ultra-deep Survey field (UDS; Lawrence et al., 2007). These fields are then split into two different observing tiers. The first of these tiers is the CANDELS/Deep tier. This tier covers a region of ~125 arcmin^2 over the two GOODS fields, to a 5σ depth of $H = 27.7$ mag. The second tier is the CANDELS/Wide tier which covers an area of ~668 arcmin^2 over all five fields, to a 5σ depth of $H \geq 27.0$ mag.

The CANDELS survey was designed with four key scientific goals in mind:

1. Cosmic Dawn - formation and evolution of galaxies and AGNs ($6 < z < 10$)
2. Cosmic High Noon - the peak of star formation and AGN activity ($z \approx 2$)
3. Ultraviolet Observations - hot stars at $1 < z < 3.5$
4. Supernovae - standardizable candles beyond $z \approx 1$

Each of these four overarching goals is separated further into smaller aims. For example, the 'Cosmic Dawn' goal is focused on constraining parameters such as star formation rates, ages, metallicities, stellar masses, and dust content at the end of the Epoch of Reionisation. Further to this, another objective is to improve constraints on the bright end of the UV luminosity function at $z \sim 6 - 8$. Duncan et al. (2014) determine the stellar mass function, luminosity function, and dust-corrected star formation rates for galaxies at $z \sim 4$, 5, 6 and 7 in the GOODS-South field of the CANDELS survey.

The 'Cosmic Noon' goal aims to improve the census of a mass-limited sample of galaxies down to $M_* = 2 \times 10^9 M_\odot$ at $z \sim 2$ and use spectral energy distributions

to determine their redshifts, stellar masses, and star formation rates. It also aims to measure quantitative structural parameters and obtain rest-frame optical morphologies. Kartaltepe et al. (2015) visually classify galaxies in all CANDELS fields, down to $H < 24.5$, within a redshift range of $0 < z < 4$. The classifications include their Hubble type and also consider whether they are mergers or involved in an interaction, or whether they exhibit a range of other features such as spiral arms. Tohill et al. (2021) use convolutional neural networks to estimate the non-parametric galaxy structural parameters concentration and asymmetry for 150,000 galaxies at $0 < z < 7$ in the CANDELS fields and are able to accurately predict these parameters within a shorter time frame than previous methods.

This thesis focuses on goals one and two by examining the evolution of a variety of galaxy parameters from the CANDELS survey since $z \sim 7$, such as the size, surface brightness, star formation, and structural parameters.

1.6 Thesis Outline

The aim of this thesis is to utilise the vast amount of data available as a result of the CANDELS survey in order to examine the evolution of galaxies and the processes that lead to the observed changes. The thesis aims to answer the following questions: How do the sizes of galaxies evolve at $1 < z < 7$? How does galaxy surface brightness evolve since $z < 6$? How does the structure of galaxies change at $0.5 < z < 3$?

Chapter 2 presents the results of an analysis of the size evolution of multiple samples of galaxies at $1 < z < 7$ in the GOODS-North and GOODS-South fields. Here I describe the image processing technique developed to remove foreground objects from images of galaxies, allowing for a more accurate determination of the Petrosian radii of the galaxies in the samples.

Chapter 3 investigates the evolution of observed and intrinsic surface brightness of a mass-selected sample of galaxies and a number density-selected sample of galaxies at $1 < z < 6$ in both the GOODS-North and GOODS-South fields.

Chapter 4 presents the results of a quantitative measure of galaxy morphology in the rest-frame optical across all five CANDELS fields at redshifts of $0.5 < z < 3$.

In the final chapter, I present the conclusions of the work presented in this thesis and discuss possible future work.

Throughout this thesis, I use AB magnitudes and assume a Λ-CDM cosmology with $H_0 = 70\ \mathrm{kms^{-1}Mpc^{-1}}$, $\Omega_m = 0.3$, and $\Omega_\Lambda = 0.7$.

Chapter 2

Unbiased Differential Size Evolution and the Inside-Out Growth of Galaxies in the Deep CANDELS GOODS Fields at $1 \leq z \leq 7$

2.1 Introduction

Despite extensive research, the details of the processes that form and influence a galaxy's evolution are still largely unknown. This will change over the next decade with the advent of new facilities such as the *James Webb Space Telescope*. However, there is still a great deal of information to be gathered from existing data from the *Hubble Space Telescope*.

The size evolution of galaxies through redshift can tell us critical information about the potential formation scenarios undergone by the first galaxies in order to produce the galaxies seen at later times. The size of a galaxy is one of the easiest and most

direct properties that can be measured. The effective radius has typically been used to determine this aspect of galaxy evolution over a range of redshifts (e.g., Buitrago et al., 2008; van der Wel et al., 2008; Bouwens et al., 2004; Allen et al., 2017).

It has been shown using the *Hubble Space Telescope* Advanced Camera for Surveys (ACS) and GOODS Near Infrared Camera and Multi-Object Spectrometer (NICMOS) (Conselice et al., 2011a) data that there is a strong evolution in the effective radii of galaxies since $z = 3$ (Trujillo et al., 2007; Buitrago et al., 2008; Cassata et al., 2013). This is further confirmed by the use of data from the Cosmic Assembly Near-infrared Deep Extragalactic Survey (CANDELS) (Grogin et al., 2011; Koekemoer et al., 2011) and NICMOS data (van Dokkum et al., 2008; Buitrago et al., 2008; Weinzirl et al., 2011; Bruce et al., 2012; Buitrago et al., 2013; Lani et al., 2013; Patel et al., 2013; van der Wel et al., 2014). Ground based observations also yield similar results (van Dokkum et al., 2010; Carrasco et al., 2010). These studies show a size evolution with an increase in effective radius since $z \sim 2$ from a factor of ∼2 (van der Wel et al., 2008) up to a factor of ∼7 (Buitrago et al., 2008; Carrasco et al., 2010). This strong evolution in size is consistent with simulations of massive galaxies forming through minor mergers (Naab et al., 2009; Furlong et al., 2017).

At redshifts higher than $z = 3$, a less steep evolution in size is found compared to $z < 3$ with the effective radius changing as $(1 + z)^{-\beta}$ where $\beta \simeq 1$ up to $z = 7$ (Bouwens et al., 2004; Oesch et al., 2010; Straatman et al., 2015; Curtis-Lake et al., 2016; Allen et al., 2017). Probing higher up to a redshift of $z \simeq 12$, the measured sizes also fit with extrapolated data (Ono et al., 2013; Holwerda et al., 2015). Such studies, both at low and high redshifts, show that massive galaxies at $z > 1$ are significantly more compact than galaxies of a comparable mass at low redshift (Ferguson et al., 2004; Cimatti et al., 2008; Damjanov et al., 2009). Observations of galaxies at high redshifts are subject to cosmological dimming and K-correction effects and this can lead to finding no obvious

evolution in size with redshift if these are not accounted for (e.g., Law et al., 2007; Ichikawa et al., 2012; Ribeiro et al., 2016).

The cause of the observed evolution in size is thought to be a result of accretion of gas and stars from the intergalactic medium and mergers with other galaxies (e.g., Ferreras et al., 2009; López-Sanjuan et al., 2012). Conselice et al. (2013) and Ownsworth et al. (2016) find that accretion is the dominant formation mode amongst the most massive galaxies by calculating the evolution of stellar mass from observed star formation rates and the amount of stellar material added via mergers. Bluck et al. (2012) suggests mergers are the primary cause of the observed size evolution in massive galaxies by determining the merger history of a sample of galaxies from the GOODS NICMOS Survey. Additionally, Bluck et al. (2012) suggest mergers can explain the majority of size evolution since $z \sim 1$ assuming mergers occur over a short timescale. Naab et al. (2009) also show this by simulating the formation of a massive spheroidal galaxy. The cosmological hydrodynamical simulation Illustris has also been used to show that the growth in size experienced by galaxies is largely caused by mergers (e.g., Wellons et al., 2016). It has also been suggested that this evolution is due to quasar feedback that removes gas from central regions, which in turn induces the expansion of the stellar distribution (Fan et al., 2008). However, the details of the processes that lead to the growth of galaxies over time are still largely unknown.

Through the study of the evolution of sizes in a sample of galaxies, we can hope to expand the understanding of the formation of galaxies. However a more refined method is now needed to make further progress on the study of galaxy sizes, and those measured using parametric fitting are often subject to biases produced by redshift. Thus, in this chapter we make use of the Petrosian radius, a redshift-independent measure of the size determined by the ratio of surface brightness at a particular radius and the surface brightness within that radius (e.g., Bershady et al., 2000; Conselice, 2003). It makes

it possible to determine not only whether galaxies are growing but also where the size is growing within the galaxies, i.e. whether the inner or outer regions of a galaxy are getting larger. By using this redshift-independent measure of size in combination with a new method to remove field galaxies from images, we present in this chapter an unbiased view of how galaxies are changing in size over time.

The structure of the chapter is as follows: In §2.2, we describe the data and the sample used. In §2.3 we describe the methods used to remove field objects from the postage stamp images of the galaxies in our sample and to calculate the sizes of the galaxies. In §2.4 we present our results. Finally, in §2.5 we discuss our results, and their implications and present our conclusions in §2.6. Throughout this chapter we use AB magnitudes and assume a Λ-CDM cosmology with $H_0 = 70$ kms^{-1}Mpc^{-1}, $\Omega_m = 0.3$, and $\Omega_\Lambda = 0.7$.

2.2 Data and Sample Selection

The data we use in this chapter are taken from the Advanced Camera for Surveys (ACS) and the Wide Field Camera 3 (WFC3) of the *Hubble Space Telescope* (*HST*). The fields used are the GOODS-North and GOODS-South fields of the Cosmic Assembly Near-infrared Deep Extragalactic Survey (CANDELS) (Grogin et al., 2011; Koekemoer et al., 2011). CANDELS covers a total area of 800 arcmin^2 over 5 different fields. GOODS-North and GOODS-South each cover an area of 160 arcmin^2 and are centered on the Hubble Deep Field North and the Chandra Deep Field South respectively (Giavalisco et al., 2004). Both GOODS fields were part of the Deep and Wide tiers of CANDELS which were observed using the WFC3 on *HST* (Grogin et al., 2011; Koekemoer et al., 2011) and these regions were observed in the F105W (Y_{105}), F125W (J_{125}), and F160W (H_{160}) filters. The ACS was used to observe the two fields in the F435W (B_{435}), F606W

(V_{606}), F775W (i_{775}), F814W (I_{814}), and F850LP (z_{850}) filters. We use only the Deep tier and this covers the central regions of the GOODS fields.

Our sample consists of 48,575 galaxies from both GOODS-North and GOODS-South fields, covering a redshift range of $1 \leq z \leq 7$ and a mass range of $10^6 M_\odot \leq M_* \leq 10^{12} M_\odot$. Details of our sample are described in Duncan et al. (2014, 2019) who make new estimates for the galaxy stellar mass function and star formation rates for this sample of galaxies in the CANDELS fields. Figure 2.1 shows the distribution of the stellar mass and the redshift of the galaxies in our sample with the yellow bins representing the highest density of points and the dark purple representing the lowest density. We see that the the highest concentration of mass and redshift lies at approximately $10^8 M_\odot \leq M_* \leq 10^9 M_\odot$ and $1 \leq z \leq 3$ however the sample spans all redshifts and masses. When selecting galaxies at high redshift ($z > 6$) for our sample, we visually inspect the images to remove any contaminating galaxies that are potential false positive detections. To determine which objects were false positives, any that had no object visible in the H_{160} band image or were saturated in H_{160} band image were removed from the sample. Figure 2.1 also shows the mass limits of each of the samples described in §2.4. The mass limits of the mass-selected sample are shown as horizontal dashed lines at $\log_{10}(M_*/M_\odot) = 9$ and $\log_{10}(M_*/M_\odot) = 10.5$. The upper mass limits of each redshift bin of the number density-selected sample (constant number density of $1{\times}10^{-4}$ Mpc^{-3}) are shown as triangles and the lower limits are shown as circles.

2.2.1 Photometric Redshifts and Stellar Masses

The photometric redshifts of the galaxies within our sample are calculated using the method described in Duncan et al. (2019). The photometric redshift software EAZY (Brammer et al., 2008) is used to determine the template-fitting estimates and three

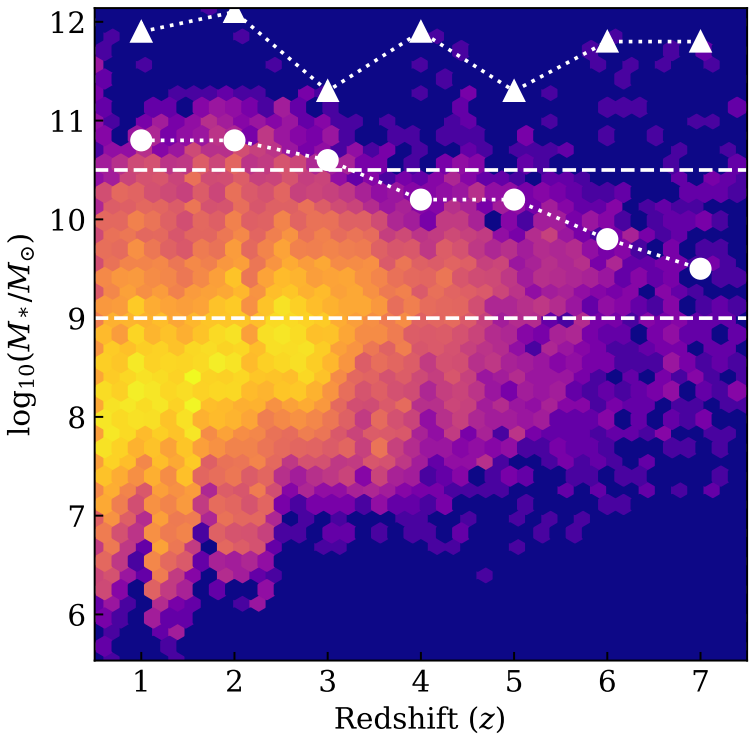

Figure 2.1: The galaxy stellar mass-redshift distribution for all 48,575 galaxies in our sample from the entire CANDELS area of the GOODS-North and GOODS-South fields (see Duncan et al. (2014, 2019) for details). The colours show the density of points with yellow representing the highest density and dark purple representing the lowest. The completeness limits are $\log_{10}(M_*/M_\odot)$ = 8.55, 8.685, 8.85, 9.15 for $z \sim 4$, 5, 6, and 7 respectively (Duncan et al., 2014). The limits for $z < 3$ are considerably lower than our chosen lower mass limit of $10^9 M_\odot$. The mass limits for each of the samples described in 2.4 are shown in white; the limits of the mass-selected sample are shown as horizontal dashed lines. The upper mass limits for each of the number density-selected sample are shown as triangles and the lower mass limits are shown as circles.

separate template sets are used and fit to all available photometric bands. The templates used include zero-point offsets to the input fluxes and additional wavelength-dependent errors. A Gaussian process code (GPz; Almosallam et al. (2016)) is then used to calculate further empirical estimates using a subset of the available photometric bands. Individual redshift posteriors are calibrated and the four estimates are combined in a statistical framework via a hierachical Bayesian combination to produce a final redshift estimate. Of the ~48,000 galaxies, 4.5% have a spectroscopic redshift. These spectroscopic

resdshifts are taken from= a range of sources. For a more in-depth description of the process, see §2.4 of Duncan et al. (2019).

The galaxy stellar masses we use are measured by using a modified version of the spectral energy distribution (SED) code described in Duncan et al. (2014). Instead of finding the best-fit mass for a fixed input redshift, the stellar mass is estimated at all redshifts in the photo-z fitting range. Also included in these estimates is a so-called 'template error function' (the method for this is described in Brammer et al. (2008)) to account for uncertainties introduced by the limited template set and any wavelength effects.

This mass-fitting technique uses Bruzual & Charlot (2003) templates and includes a wide range of stellar population parameters and assumes a Chabrier (2003) initial mass function. The assumed star formation histories follow exponential τ-models for both positive and negative values of τ. Characteristic timescales of $|\tau|$ = 0.25, 0.5, 1, 2.5, 5, and 10 are used, along with a short burst (τ = 0.05) and continuous star formation models ($\tau \gg 1/H_0$).

We compare the mass measurements we make to the average of those determined by the several teams within the CANDELS collaboration (Santini et al., 2015). This is done in order to ensure that the stellar mass estimates do not suffer from systematic biases. There is some scatter between the two mass estimates, however our mass estimates are not affected by any significant biases compared to others. IRAC imaging is also used to increase the reliability of the stellar masses at higher redshifts due to the filters covering UV light on the blue side of the 4000Å break at these redshifts. Systematic and random errors could introduce an error of approximately a factor of 2 however this would not affect the results. For further details on the method and models used, see §2.5 of Duncan et al. (2019) for an extensive discussion of the masses we use here.

2.3 Methodology

2.3.1 2D Lyman-Break Imaging

Here we describe the new method we use to produce images to measure the properties of galaxies in our sample. The method uses the well-known Lyman-break drop technique where a galaxy at a certain redshift 'disappears' at wavelengths redder than the Lyman limit at 912 Å which creates a sharp break in the continuum. This break gives galaxies distinctive ultraviolet (UV) rest-frame colours which can be used to select galaxies at specific redshifts using photometry within multiple filters. The hydrogen gas absorbs the bluest wavelengths of light and thus the target object essentially disappears or becomes significantly fainter compared to the flux in redder bands. The break is observed at redder wavelengths as the redshift increases. For galaxies at $z = 6$ and $z = 7$, the break falls within the V_{606} band, and for galaxies at $z = 5$ and $z = 4$, the break falls within the B_{435} band. The band corresponding to the break for galaxies at $z < 3$ is at a shorter wavelength than the available filters therefore this image processing technique is applied only to galaxies at $z \geq 4$. Note that effectively the galaxy nearly disappears in filters which probe light below the Lyman limit, thus making it possible to isolate the light which belongs to these galaxies from those at lower and significantly higher redshifts. However, the majority of field objects will be at a lower redshift than the target objects so there will be minimal contamination from those that are at higher redshifts.

The basic technique was first used by Steidel et al. (1996) to find distant galaxies as unresolved objects in ground based imaging but can also be used in a 2-dimensional way to remove foreground and background galaxies for systems where the Lyman break is visible within resolved imaging as with the *Hubble Space Telescope*. We call this '2D Lyman-Break Imaging', an earlier version of which is described in Conselice & Arnold (2009).

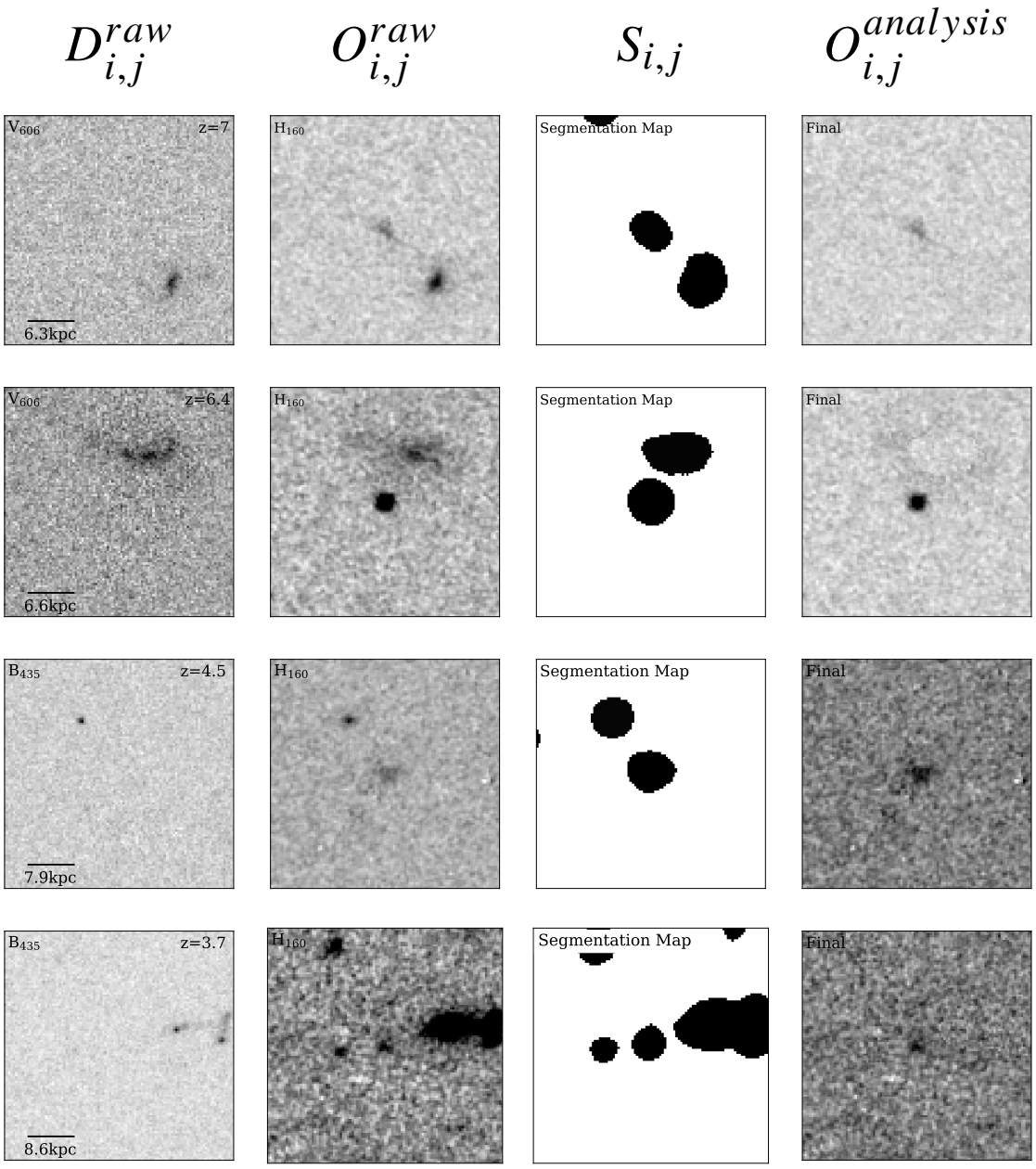

Figure 2.2: Examples of our image processing technique for four galaxies at redshifts of 7.0, 6.4, 4.5, and 3.7. Each column ($D^{raw}_{i,j}$, $O^{raw}_{i,j}$, $S_{i,j}$, and $O^{analysis}_{i,j}$) corresponds to the parameters of Equation 2.1. The first column (left) shows the original V_{606} or B_{435} image showing the light below the Lyman-break rest-frame wavelength for the central galaxy's redshift, the second column shows the original H_{160} band image, the third column shows the segmentation map corresponding to the optical rest-frame, while the fourth column (right) shows the result of the image processing whereby all galaxies that appear below the Lyman break are removed (see Equation 2.1 for details). The field of view is 6" on a side.

Initially, postage stamps measuring 6"×6" (100 pixels × 100 pixels) in size are created from a mosaic image of the field. The postage stamps contain the target object at the centre and contain other galaxies projected near the galaxy at different redshifts. In order to minimise contamination from the field objects, the target objects are isolated by removing these potentially contaminating objects. The following steps of our procedure are probably best demonstrated with images as shown in Figure 2.2. To remove the foreground objects, the band corresponding to the Lyman break and below is subtracted from the optical rest-frame image. The resulting image is then normalised by the optical rest-frame image. Maps of the pixels associated with the galaxy of interest are created such that the pixels corresponding to the central object are given a value of one and the pixels corresponding to the sky are given a value of 0. These are created by selecting pixels that have a value that is equal to or greater than three times the standard deviation of the background statistics.

This map is used in combination with a segmentation map of the optical rest-frame image, where only pixels with values greater than 3 times the standard deviation of the background are selected, to remove areas of the sky that are identified as field objects. These removed areas and objects are then replaced with noise that has the same mean and standard deviation as the sky. Figure 2.2 shows this process for four galaxies at redshifts of 7.0, 6.4, 4.5 and 3.7. On the left we show the original V_{606} or B_{435} band images. Only the foreground objects are visible in these bands. In the second column, we show the optical rest-frame image for each of our sample galaxies where both the central object and potentially contaminating foreground objects are visible. In the third column, we show the corresponding segmentation map which highlights those pixels that are associated with the target galaxy and other objects. There are small differences between the objects appearing in the blue and red images however we always use the segmentation map that corresponds to the optical rest-frame such that these foreground

objects are removed completely.

On the right of Figure 2.2, we show the result of the image processing where we have removed the foreground objects from the image. It is this final image in which we carry out our size analysis.

Our image processing technique can be described by the equation

$$O_{i,j}^{analysis} = \left(\frac{O_{i,j}^{raw} - D_{i,j}^{raw}}{O_{i,j}^{raw}} \cdot S'_{i,j} \right) + f(O_{i,j}^{raw,sky}) \tag{2.1}$$

where $O_{i,j}^{raw}$ is the original optical rest-frame image or its substitute, $D_{i,j}^{raw}$ is the original drop-out image, $S'_{i,j}$ is the segmentation map where where only pixels with values greater than 3 times the standard deviation of the background are selected, and $f(O_{i,j}^{raw,sky})$ is some function of the raw optical rest-frame image. The function $f(O_{i,j}^{raw,sky})$ creates an image in which the pixels corresponding to the central object are 0, the pixels corresponding to the sky are those of the raw optical rest-frame image, and the pixels corresponding to the field objects are noise that has the same mean and standard deviation of the sky. The pixel values of both $O_{i,j}^{raw}$ and $D_{i,j}^{raw}$ must be in the same units e.g. $e^{-}s^{-1}cm^{-2}Å^{-1}$.

We measure the sizes of our galaxies using the images produced using our 2D Lyman-break method of removing foreground objects from the optical rest-frame images of our galaxy sample. This allows us to probe the rest-frame at $\lambda \sim 4000$ Å wherever possible. The bands used for the image processing are shown in Table 2.1, along with the rest-frame wavelength we probe at each redshift. Due to the availability of bands, we must use bands that correspond to the UV at higher redshifts. The possible effects of this are explored later on in this chapter, in §2.4.1.

Table 2.1: The bands used to complete the image processing for each redshift in Column 1. Column 2 gives the band corresponding to the optical rest-frame ($O_{i,j}^{raw}$), and Column 3 gives the band corresponding to the Lyman-break where applicable ($D_{i,j}^{raw}$). Column 4 gives the rest-frame wavelength probed.

z	$O_{i,j}^{raw}$	$D_{i,j}^{raw}$	λ_{rest}
1	I_{814}	-	4070 Å
2	J_{125}	-	4170 Å
3	H_{160}	-	4000 Å
4	H_{160}	B_{435}	3200 Å
5	H_{160}	B_{435}	2670 Å
6	H_{160}	V_{606}	2290 Å
7	H_{160}	V_{606}	2000 Å

2.3.2 Galaxy Sizes

This work uses the Petrosian radius ($R_{\rm Petr}(\eta)$) which is defined as the radius at which the surface brightness at a given radius is a particular fraction of the surface brightness within that radius (e.g., Bershady et al., 2000; Conselice, 2003). The concept of defining a size of a galaxy by the rate of change of light as a function of radius was first proposed by Petrosian (1976) for cosmological uses. The radius measured depends on a defined ratio ($\eta(r)$) of surface brightness. $\eta(r)$ is defined as

$$\eta(r) = \frac{I(r)}{\langle I(r) \rangle} \tag{2.2}$$

where $I(r)$ is the surface brightness at radius r and $\langle I(r) \rangle$ is the mean surface brightness within that radius. By this definition, $\eta(r)$ is 1 at the centre and 0 at large r (Kron, 1995). The Petrosian radius at $\eta = 0.2$ contains at least 99% of the light within a given galaxy (Bershady et al., 2000). This is valid for all galaxy profiles.

The Petrosian radius we use is determined using the CAS (concentration, asymmetry, and clumpiness) code (Conselice, 2003) which provides two measurements of size

(Petrosian radius and half-light radius) along with the CAS parameters. The Petrosian radius differs from the half-light radius in that the former is a redshift independent measure of galaxy size. As such, the Petrosian radius of a particular galaxy would be, in principle, measured as the same no matter what redshift it was placed, whereas the half-light radius would potentially decrease as the redshift increases and outer light is lost.

We however examine this assumption and correct for the effects of the PSF in the measurement of the Petrosian radii through simulating images and measuring radii in the same way as we do for our sample galaxies. In Figure 2.3, we show how η varies with radius r for 98 random galaxies within our sample across a range of redshifts. We show that on average, those galaxies at the higher redshifts (yellow lines) are smaller in size than those at a given lower redshift (purple lines). The lines plotted are exponential fits of the η profiles of the form

$$\eta(r) = ae^{-cr} + d. \tag{2.3}$$

The horizontal lines indicate the positions of the three η values used throughout.

2.3.3 Simulations

To determine how well we can measure galaxy sizes through Petrosian radii we follow the same method as Bhatawdekar et al. (2019) and simulate a sample of galaxies using the IRAF task, MKOBJECTS in order to determine how much of a correction to the measured radii is required. The sample of 1912 simulated galaxies is uniformly distributed across the simulated field and a luminosity distribution of the form of a power law is applied to create a range of magnitudes. The simulated galaxies lie within

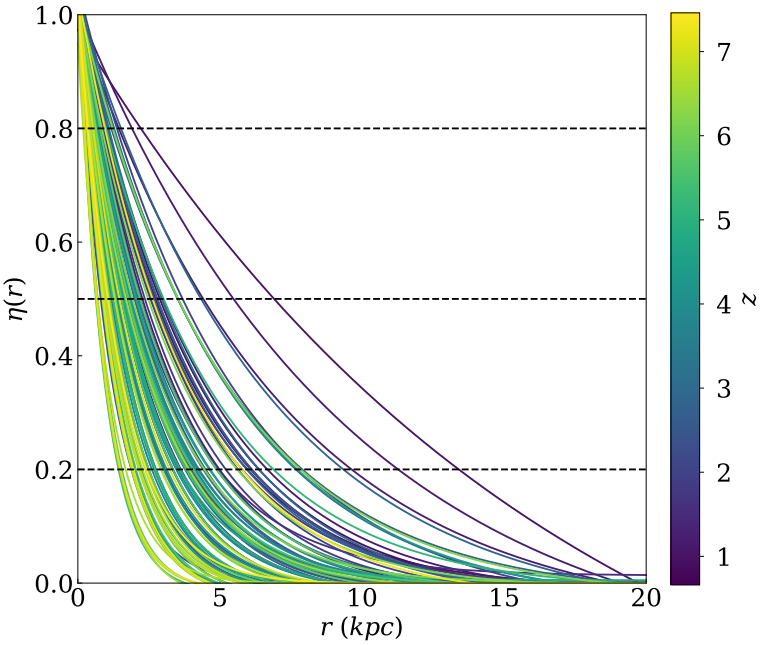

Figure 2.3: Exponential fits of the form $\eta(r) = ae^{-cr} + d$ of the η profiles for 98 random galaxies from our sample showing that on average, the higher redshift galaxies are smaller than those at lower redshift. The line colour corresponds to the redshift of each of the galaxies, as indicated by the colourbar on the right. The three horizontal lines indicate the locations of $\eta = 0.2$, 0.5, and 0.8.

a magnitude range of 21 to 30 and a size range of 2 to 42 pixels. We apply a range of surface brightness profiles to the sample of simulated galaxies with Sersic indices in the range $0.5 < n < 4$. The simulated galaxies are convolved using the WFC3 point spread function (PSF). We use the same PSF for each of the simulated galaxies due to the fact that any potential PSF variations do not make a significant impact at this level as we use it solely on the simulated images and not in any fits produced. After this image is created, SExtractor (Bertin & Arnouts, 1996) is run on on the new image to detect the sources. A postage stamp measuring 100 pixels × 100 pixels of each object (pre- and post-convolution) is created and examples of the simulated galaxies can be seen in Figure 2.4. We show here the images before the WFC3 PSF has been applied on the left and the images after the PSF has been applied on the right. The CAS code we use for the real sample is then applied to this simulated sample to calculate the Petrosian

radius of each of the objects in the same way we did for our original sample. We then compare the radii measured before applying the PSF to the radii measured after the PSF is applied for each value of η (0.2, 0.5, and 0.8) and the relationship between the two is obtained through a linear fit. In the real images, noise would have some effect on the measured size such that the galaxies may appear slightly larger than in reality however this effect is negligible so would not alter the results.

The relationship between the observed and intrinsic radii for each η value for the simulated galaxies is shown in Figure 2.5. We show $R_{\rm Petr}(\eta = 0.2)$ on the left, $R_{\rm Petr}(\eta = 0.5)$ in the centre, and $R_{\rm Petr}(\eta = 0.8)$ on the right. The linear fits are shown as a red line on each of the panels. This fit is then applied to our observed sample to correct the measured radii. On average, all three radii change by a factor of ~ 0.8 with the radii measured using $\eta = 0.8$ changing on average by 0.036" (0.6 pixels), radii measured using $\eta = 0.5$ changing on average by 0.081" (1.35 pixels), and radii measured using an $\eta = 0.2$ changing by 0.094" (1.56 pixels) on average. The change in measured size for these simulated galaxies is very small. We find the best fit between the size before and after PSF convolution using the analytical form

$$R_{intrinsic} = mR_{observed} + c. \tag{2.4}$$

We henceforth correct our radii using these average values. These corrections are valid down to a radius of 2 pixels.

2.4 Results

In this section we present the results achieved by measuring the sizes of our galaxies in two different sub-samples taken from the full sample as described in §2.2; a mass-

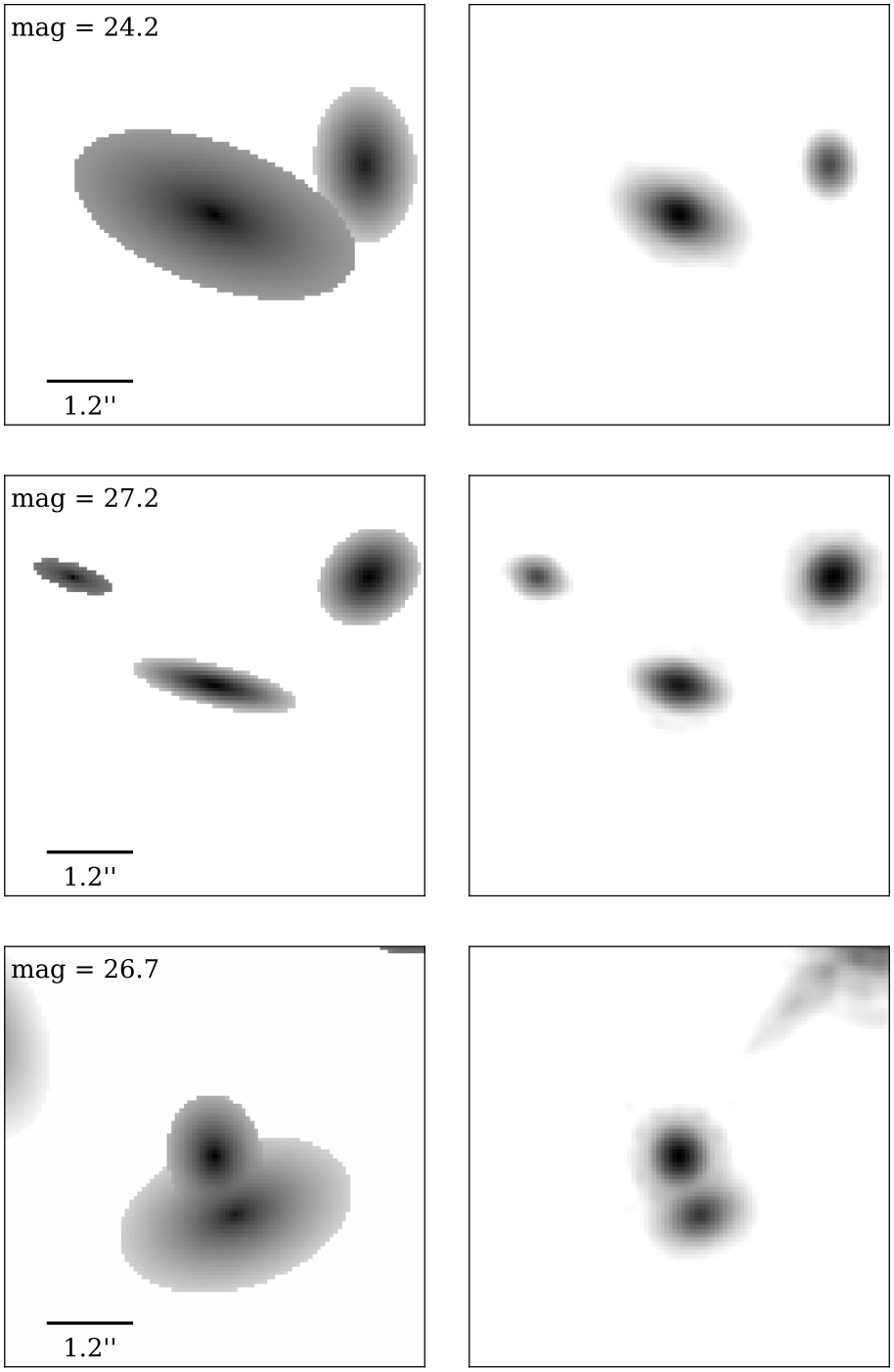

Figure 2.4: Examples of the simulated galaxies before the WFC3 PSF is applied (left) and after (right). These are idealized images which we use to correct the effects of PSF on our size measurements.

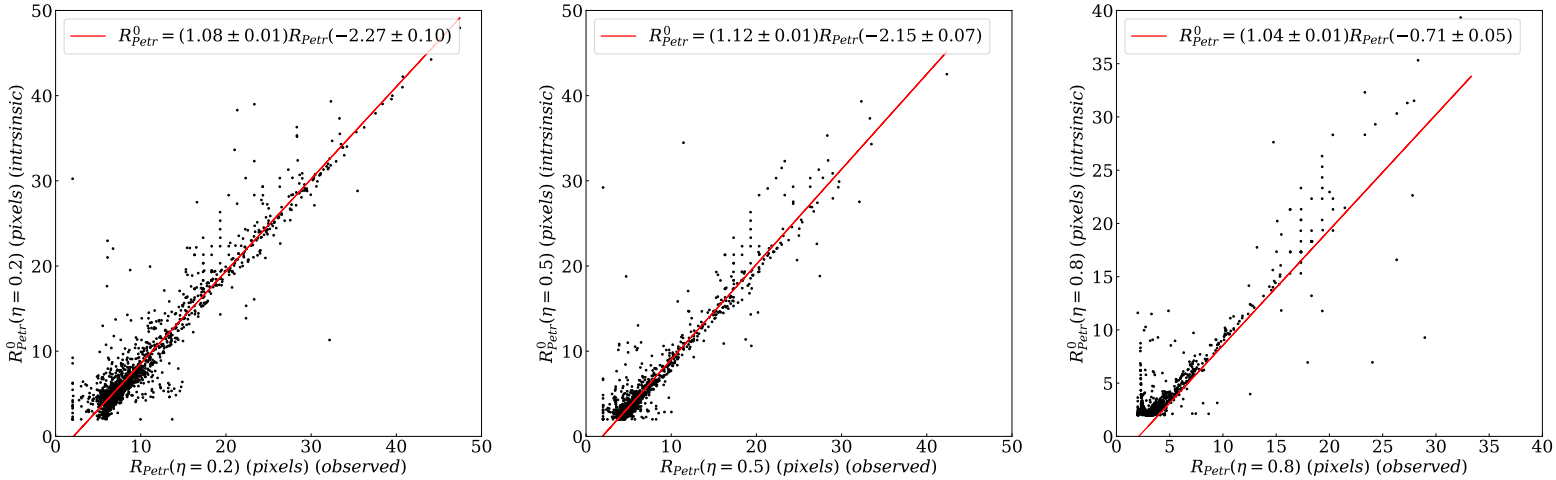

Figure 2.5: Relationship between the post-convolution sizes and the pre-convolution sizes measured on the simulated galaxies described in §2.3.3 for $\eta = 0.2$ (left), $\eta = 0.5$ (middle), and $\eta = 0.8$ (right). Fits of the form $R_{intrinsic} = mR_{observed} + c$ for each Petrosian radius have been plotted as a red line. For $R_{\rm Petr}(\eta = 0.2)$ we find $m = 1.08 \pm 0.01$ and $c = -2.27 \pm 0.10$. For $R_{\rm Petr}(\eta = 0.5)$ we find $m = 1.12 \pm 0.01$ and $c = -2.14 \pm 0.10$. For $R_{\rm Petr}(\eta = 0.8)$ we find $m = 1.04 \pm 0.01$ and $c = -0.71 \pm 0.05$. The post-convolution sizes are on average changed by 0.094" for $\eta = 0.2$, 0.081" for $\eta = 0.5$, and 0.036" for $\eta = 0.8$.

selected sample where galaxies lie within a mass range of $10^9 M_\odot \leq M_* \leq 10^{10.5} M_\odot$, and a number density-selected sample where galaxies are selected using a constant number density of $1{\times}10^{-4}$ Mpc^{-3}. Where reference is made to a galaxy's size, this is taken to be the measured Petrosian radius.

2.4.1 Rest-frame Wavelength and Biases

The appearance of a galaxy depends greatly on its rest-frame wavelength, and a galaxy can have a different morphological and quantitative classification at different wavelengths (Windhorst et al., 2002; Taylor-Mager et al., 2007; Mager et al., 2018). This is due to the fact that different wavelengths probe different aspects of a galaxy, with bluer light probing star formation and redder light probing the older existing populations of stars. The young stars can often have a distribution which is quite different from the older stars, and this needs to be accounted for if we want to measure galaxy sizes at intrinsically different rest-frame wavelengths.

This is also true of the measured surface brightness, and therefore the measured Petrosian radii. This effect is more prominent at lower redshifts when the star formation has dropped significantly. At low redshift, there is little star formation therefore galaxies at this epoch appear less luminous in the UV and therefore are often smaller in the UV than those at higher redshifts where more star formation occurs (e.g., Hopkins & Beacom, 2006). Furthermore, it has been shown that whilst the rest-frame UV and optical structures of galaxies are often significantly different in the local universe, this is not true at high redshifts where galaxies are in many ways extremely similar in terms of structure in the rest-frame UV and optical (e.g., Papovich et al., 2003, 2005; Conselice et al., 2005, 2011b). This is due to the fact that high redshift galaxies are dominated by star formation whereas low redshift galaxies are significantly less star-forming. There

is no explicit cut-off however it is expected that by $z = 1$, we can assume the UV and optical structures of galaxies do not differ significantly. It has also been shown that the measured size of a galaxy does not depend on the observed wavelength to the first order, even after correcting for surface brightness dimming and PSF broadening (Ribeiro et al., 2016). Therefore we are able to use images that correspond to the UV rest-frame at high redshifts, particularly in the case of the most massive galaxies as the variation is not so significant for this population (Cassata et al., 2010).

We thus measure the sizes of galaxies in the optical rest-frame at $\lambda \cong 4000$ Å where possible. However, this is not possible for galaxies at $z > 3$ where we are forced to probe galaxy sizes in progressively bluer wavelengths down to the UV. To determine the bias resulting from this we compare the sizes measured in the observed rest-frame ($\lambda = 4000$ Å) to the intrinsic rest-frame UV at $\lambda \sim 2200$ Å. We do this test at the lower redshifts at $1 < z < 5$ where we have both a rest-frame optical and rest-frame UV morphology. What we find when we do this is that the sizes at both wavelengths are approximately equal. To show this we fit a straight line of the form

$$R_{\lambda_1} = mR_{\lambda_2} + c \tag{2.5}$$

to the results where R_{λ_1} is the Petrosian radius at $\eta = 0.2$ measured in the intrinsic bluer rest-frame and R_{λ_2} is the Petrosian radius at $\eta = 0.2$ measured in the redder rest-frame. The fits for each redshift can be found in Table 2.2. We only include results up to $z = 5$ due to the availability of bands corresponding to the appropriate rest-frame. Table 2.2 also gives the bands used to compare the observed and intrinsic sizes. The mean difference between these two wavelengths ($\overline{\delta R}$) is shown in Column 6 of Table 2.2. This difference has been normalised by R_{λ_1}. These values show that the size measurements made at the bluer rest-frame are similar in magnitude to those made at

the redder rest-frame wavelength.

Table 2.2: Slopes (Column 2) and y-intercept (Column 3) of the observed rest-frame size (R_{λ_1}) and intrinsic rest-frame size (R_{λ_2}) measurement fits (given by Equation 2.5), including errors for each redshift (Column 1). Columns 4 and 5 give the bands corresponding to the observed and intrinsic rest-frame wavelengths respectively. Column 6 gives the mean difference between the size measured in the observed and intrinsic rest-frame wavelengths. This difference has been normalised by R_{λ_1}. R_{λ_1} and R_{λ_2} are the Petrosian radii measured at $\eta = 0.2$.

z	m	c	λ_2	λ_1	$\lvert\frac{\overline{\delta R}}{R_{\lambda_1}}\rvert$
1	0.5359 ± 0.0001	5.0641 ± 0.0053	I_{814}	B_{435}	0.06
2	0.6488 ± 0.0001	5.4437 ± 0.0044	J_{125}	V_{606}	0.63
3	0.6904 ± 0.0002	4.7803 ± 0.0156	H_{160}	z_{850}	0.41
4	0.4584 ± 0.0013	2.9556 ± 0.0635	H_{160}	Y_{105}	0.11
5	0.5941 ± 0.0015	2.3206 ± 0.0685	H_{160}	J_{125}	0.07

The slope of relationship between the observed and intrinsic rest-frame is shown in Figure 2.6. Although the slope is less than one at all redshifts, the difference seen would not significantly change the results when examining the radius evolution of the galaxies in our sample.

2.4.2 Redshift-Size Relation

By studying our full sample, we are able to see the effect redshift has on the size of galaxies for the full mass range. The distribution of the corrected Petrosian radii with redshift of the total sample size at three different η values can be seen in Figure 2.7 with $\eta = 0.2$ on the left, $\eta = 0.5$ in the middle, and $\eta = 0.8$ on the right. We represent the pixel size as a white dashed line. From the definition of the Petrosian radius, $\eta = 0.2$ corresponds to a measurement made near the outer edge of a galaxy, and $\eta = 0.8$ corresponds to a measurement made in the inner regions of a galaxy. The evolution of each radius with redshift changes in a similar way in that there are more galaxies at larger radii at lower redshifts than seen at higher redshifts. However, the values of the

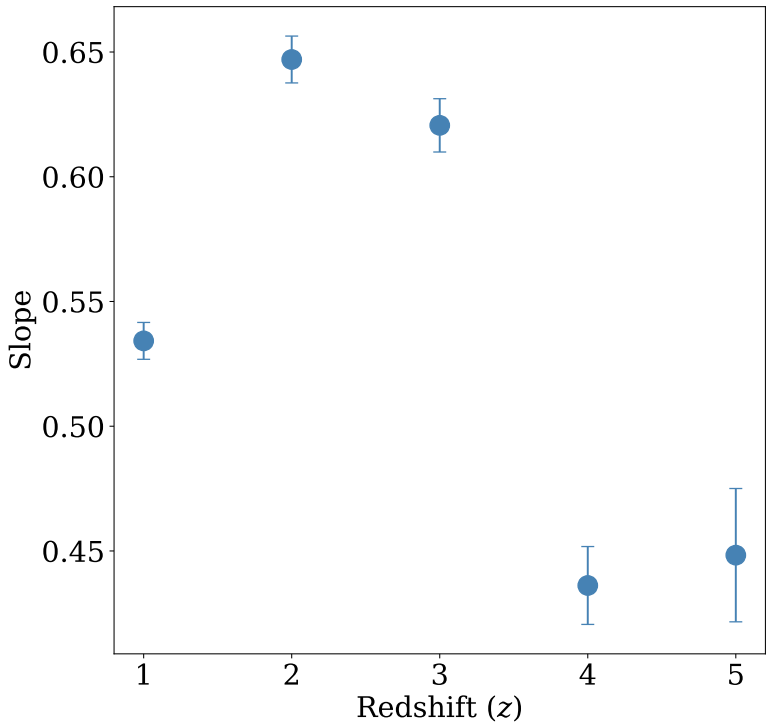

Figure 2.6: The slope of the relationship between the observed and intrinsic rest-frame for the redshift range of $1 < z < 5$. The 50% difference would not significantly change the results.

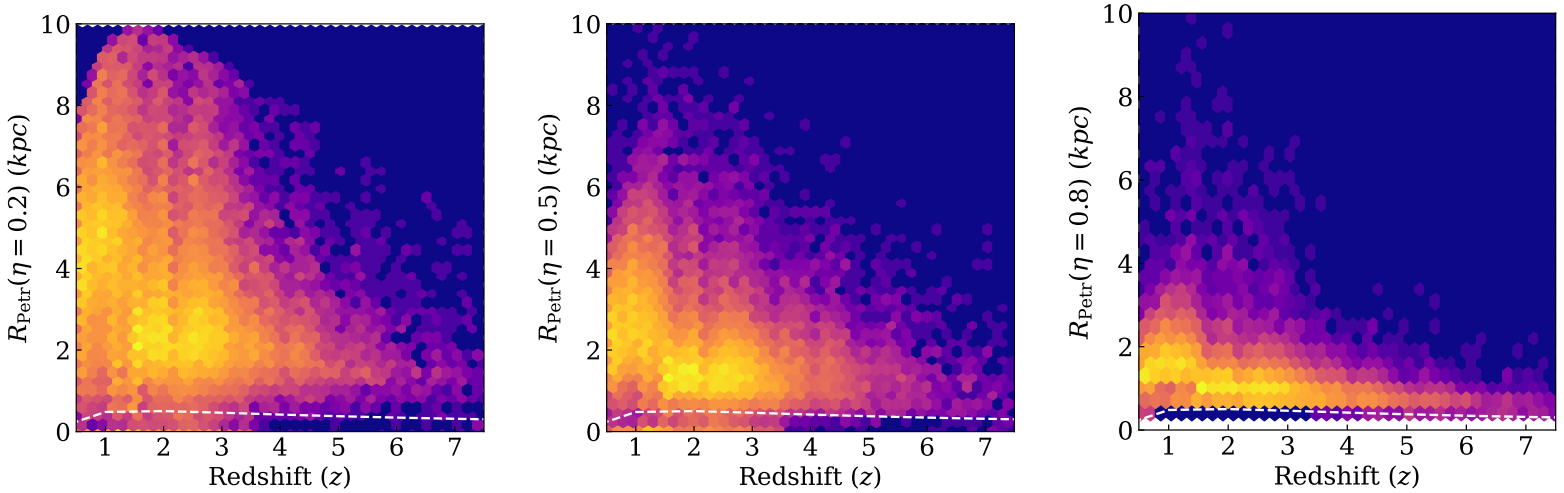

Figure 2.7: Galaxy size-redshift distribution for the full sample of galaxies for three different η values. Left: $\eta = 0.2$. Middle: $\eta = 0.5$. Right: $\eta = 0.8$. The yellow regions show the highest density of points and purple the lowest. The pixel size is shown by the the white dashed line.

radii differ such that the $\eta = 0.2$ values are typically much larger than those of $\eta = 0.8$ as expected.

2.4.3 Mass-Size Relation

From the full sample of galaxies we are able to determine the mass-size relation as a function of redshift. In Figure 2.8, we show the mass-size distribution for each redshift bin. We use $R_{\rm Petr}(\eta = 0.2)$ as a measure of size in this case. Each panel corresponds to a different redshift, showing the density of the mass-size distribution and a line of best fit. At low redshift, there appears to be a cut-off at the higher radii however this is due to the way in which the data is binned and the limitation of radii on the size of the postage stamps used to measure the radii. The redshift given in the upper left corner of each panel indicates the midpoint of the redshift bin where the upper and lower limits are 0.5 either side of this point. In the final panel, we show the lines of best fit for all seven redshift bins, each in the same colour as their individual panels. The lines of best fit are of the form

$$\log_{10}(R_{\rm Petr}(\eta = 0.2)) = m\log_{10}(M_*/M_\odot) + c \tag{2.6}$$

and the parameters for each redshift bin are shown in Table 2.3. We see that the slope of the fit (m) decreases as redshift increases, showing that the sizes of the galaxies at lower redshifts have a greater dependence on their masses compared to those galaxies at higher redshifts. We also find that the intercept (c), on average, decreases as z increases showing an evolution in size. These fits don't take the errors in the masses into account so the errors on the slope at high redshift are likely larger due to the uncertainty in measuring stellar mass in the UV.

Table 2.3: The parameters determined for the mass-size relation (shown in Figure 2.8) for each redshift bin. The fits are given in the form $\log_{10}(R_{\rm Petr}(\eta = 0.2)) = m\log_{10}(M_*/M_\odot) + c$. These fits don't take the errors in the masses into account so the errors on the slope at high redshift are likely larger due to the uncertainty in measuring stellar mass in the UV.

z	m	c
1	0.139±0.002	-0.567±0.018
2	0.137±0.003	-0.742±0.025
3	0.126±0.004	-0.693±0.037
4	0.073±0.005	-0.293±0.048
5	0.064±0.009	-0.289±0.078
6	0.090±0.013	-0.581±0.117
7	0.048±0.027	-0.289±0.249

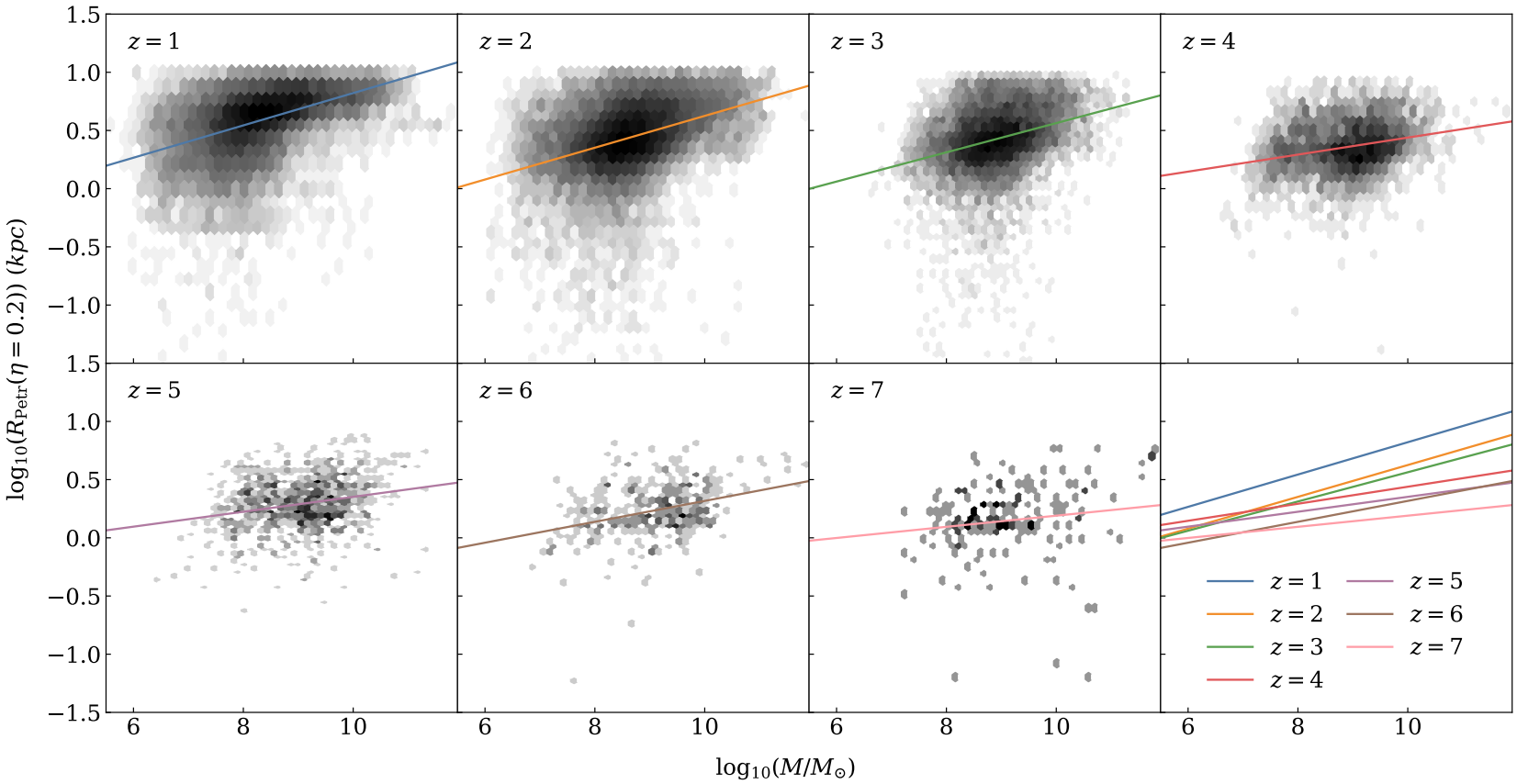

Figure 2.8: Galaxy stellar mass-size distributions for the full sample of galaxies. The size measurement is given by $R_{\rm Petr}(\eta = 0.2)$. Each panel shows the distribution of a different redshift along with a line of best fit given in Equation 2.6. In the final panel, we show the fitted mass-size relation for each redshift using the same coloured lines as in the individual panels. The gradient of each best fit is positive however it decreases as redshift increases. The best fit parameters are given in Table 2.3.

2.4.4 Mass-selected Sample

Here we present the results of the analysis of a mass-selected sample ($10^9 M_\odot \leq M_* \leq 10^{10.5} M_\odot$) of 14,015 galaxies taken from the full sample. This mass range is chosen for completeness (Duncan et al., 2014). A mass-selected sample allows us to remove biases present in the full sample due to the detection limits of the surveys.

Comparing the median sizes of the galaxies in our sample at different epochs shows how the sizes evolve with redshift. Figure 2.9 shows the evolution of the median corrected radii of our mass-selected sample. The blue circles show the evolution of the $R_{\rm Petr}(\eta = 0.2)$ values, the orange diamonds show the evolution of $R_{\rm Petr}(\eta = 0.5)$, and the green squares show the evolution of $R_{\rm Petr}(\eta = 0.8)$. The error bars on each point are the standard error on the median. There is a clear change in each of the radii measurements from $z = 7$ to $z = 1$, particularly in the case of $\eta = 0.2$. We find that $R_{\rm Petr}(\eta = 0.2)$ increases by a factor of 3.78 ± 0.39 from $z = 7$ to $z = 1$ whereas $R_{\rm Petr}(\eta = 0.8)$ increases by a factor of 3.20 ± 0.19. We fit a simple power-law relation to the median measured sizes for each η value of the form

$$R_{\rm Petr}(\eta) = \alpha(1 + z)^{\beta}{\rm kpc}. \tag{2.7}$$

The values we find for α and β for each of the methods and η values can be seen in Table 2.4. The values for α and β for the mass-selected sample can be seen in Columns 2 and 3. In Figure 2.9, the power-law fits for the full samples are shown as a blue dotted line for $R_{\rm Petr}(\eta = 0.2)$, an orange dashed line for $R_{\rm Petr}(\eta = 0.5)$, and a green solid line for $R_{\rm Petr}(\eta = 0.8)$.

Table 2.4: The fits determined for both the mass-selected and number density-selected samples as given by Equation 2.7.

	Mass		Number Density	
η	α	β	α	β
0.2	11.68±0.16	-0.97±0.03	12.62±1.10	-0.82±0.14
0.5	6.27±0.10	-0.92±0.03	4.57±0.48	-0.53±0.16
0.8	3.10±0.04	-0.80±0.03	2.66±0.18	-0.67±0.11

2.4.5 Number Density-selected Sample

Instead of selecting a sample of galaxies by their mass, in this selection we create a sample of galaxies based on a constant number density. This method has been used in a number of previous studies to examine galaxy formation and evolution over a large redshift range (van Dokkum et al., 2010; Papovich et al., 2011; Conselice et al., 2013; Ownsworth et al., 2016). This has been proven to have several advantages. Although the stellar mass grows through star formation and minor mergers, the number density of galaxies above a given density threshold is invariant with time in the absence of major mergers or extreme changes of star formation (Ownsworth et al., 2016). Selecting galaxies through this method directly tracks the progenitors and descendants of massive galaxies at all redshifts (e.g., Mundy et al., 2015; Ownsworth et al., 2016).

We select a sample of galaxies using a constant number density of 1×10^{-4} Mpc^{-3}, yielding a sample size of 521 galaxies. This is done by ranking the galaxies in each redshift bin by stellar mass until the required number density is reached. Figure 2.10 shows the evolution of the median corrected radii for this selected sample. As for Figure 2.9, the blue circles represent $R_{\rm Petr}(\eta = 0.2)$, orange diamonds represent $R_{\rm Petr}(\eta = 0.5)$ and green squares represent $R_{\rm Petr}(\eta = 0.8)$. We fit a power-law to the median sizes. We show these fits in Table 2.4 and in Figure 2.10 as a blue dotted line for $R_{\rm Petr}(\eta = 0.2)$, an orange dashed line for $R_{\rm Petr}(\eta = 0.5)$, and a green solid line for $R_{\rm Petr}(\eta = 0.8)$. We find

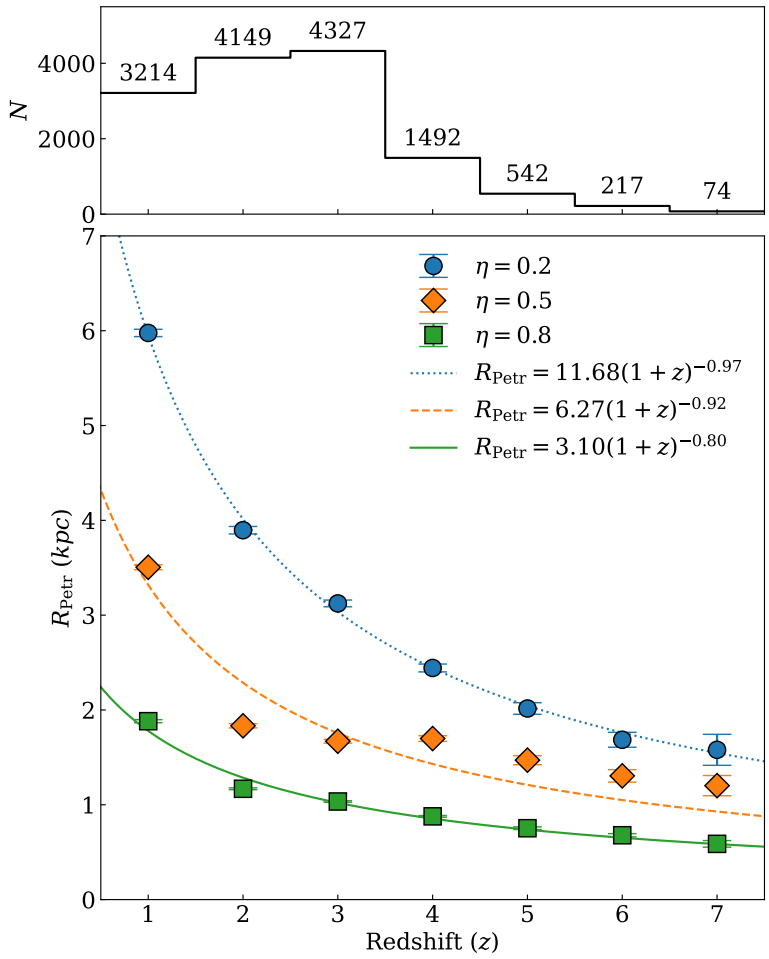

Figure 2.9: Top: histogram showing the distribution and number of galaxies in each redshift bin. Bottom: evolution of the average Petrosian radius through redshift for the mass limited sample where a mass-cut of $10^9 M_\odot \leq M_* \leq 10^{10.5} M_\odot$ is applied. Each point is the median value for each redshift bin with the error bars showing the standard error. Blue circles show how $R_{\rm Petr}(\eta = 0.2)$ changes, orange diamonds show $R_{\rm Petr}(\eta = 0.5)$, and green squares show $R_{\rm Petr}(\eta = 0.8)$. By fitting a power-law relation to the median sizes, we find $R_{\rm Petr}(\eta = 0.2) = 11.68(1+z)^{-0.97\pm0.03}$ (blue dotted line), $R_{\rm Petr}(\eta = 0.5) = 6.27(1+z)^{-0.92\pm0.03}$ (orange dashed line), and $R_{\rm Petr}(\eta = 0.8) = 3.10(1+z)^{-0.80\pm0.03}$ (green solid line).

that $R_{\rm Petr}(\eta = 0.2)$ changes by a factor of 3.39 ± 0.54 over the redshift range $1 < z < 7$, a much more significant change compared to a factor of 2.59 ± 0.24 for $R_{\rm Petr}(\eta = 0.8)$ over the same redshift range.

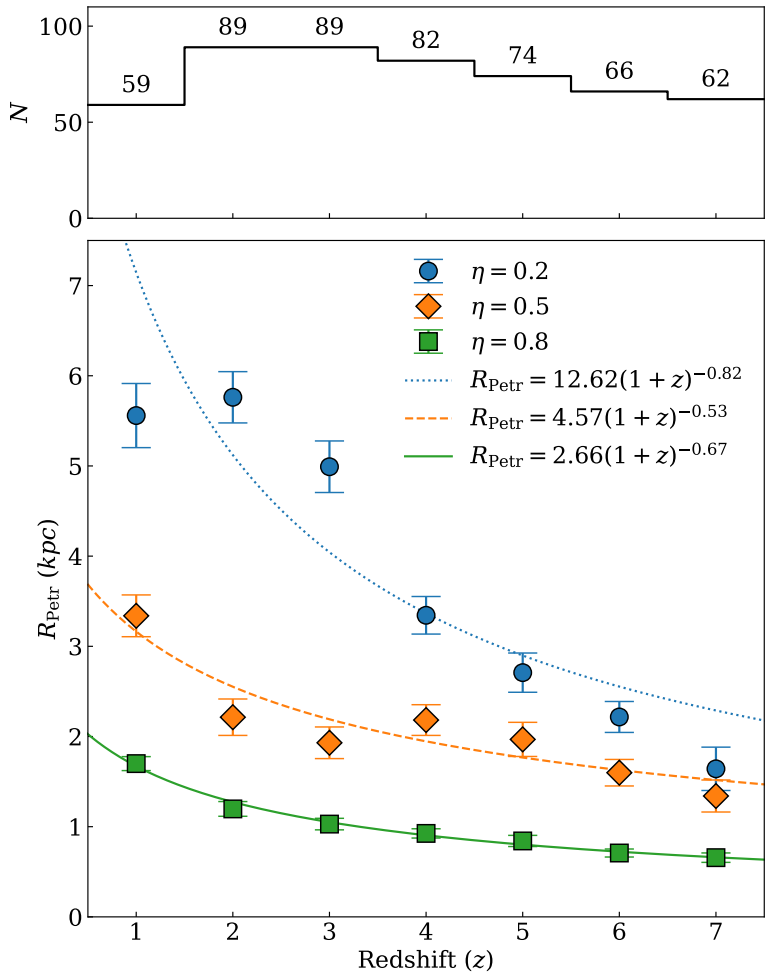

Figure 2.10: Top: histogram showing the distribution and number of galaxies in each redshift bin. Bottom: evolution of the average Petrosian radius through redshift for the number density-selected sample where galaxies within a constant number density of $1{\times}10^{-4}$ Mpc^{-3} are selected. Each point is the median value for each redshift bin with the error bars showing the standard error. Blue circles show how $R_{\rm Petr}(\eta = 0.2)$ changes, orange diamonds show $R_{\rm Petr}(\eta = 0.5)$, and green squares show $R_{\rm Petr}(\eta = 0.8)$. A power-law relation is fit to each radius and we find $R_{\rm Petr}(\eta = 0.2) = 12.62(1+z)^{-0.82\pm0.14}$ (blue dotted line), $R_{\rm Petr}(\eta = 0.5) = 4.57(1+z)^{-0.53\pm0.16}$ (orange dashed line), and $R_{\rm Petr}(\eta = 0.8) = 2.66(1+z)^{-0.67\pm0.11}$ (green solid line).

2.4.6 Inner Versus Outer Regions

In order to determine where the radius changes the most, we plot the normalised difference between the median $R_{\rm Petr}(\eta = 0.2)$ and $R_{\rm Petr}(\eta = 0.8)$ against redshift in Figure 2.11 where $R_{\rm Petr}(\eta = 0.2)$ corresponds to the outer edges of a galaxy and $R_{\rm Petr}(\eta = 0.8)$

corresponds to the inner regions of a galaxy. The normalised difference in the radii is given by

$$\Delta R_{\rm Petr} = \frac{R_{\rm Petr}(\eta = 0.2) - R_{\rm Petr}(\eta = 0.8)}{R_{\rm Petr}(\eta = 0.8)}. \tag{2.8}$$

The difference between the radii measured at the outer edge and the inner regions for both the mass-selected and number density-selected samples is shown in Figure 2.11. The mass-selected sample is represented by the red diamonds and the number density-selected sample by black squares. $\Delta R_{\rm Petr}$ increases as redshift decreases for both samples, but more significantly for the number density-selected sample.

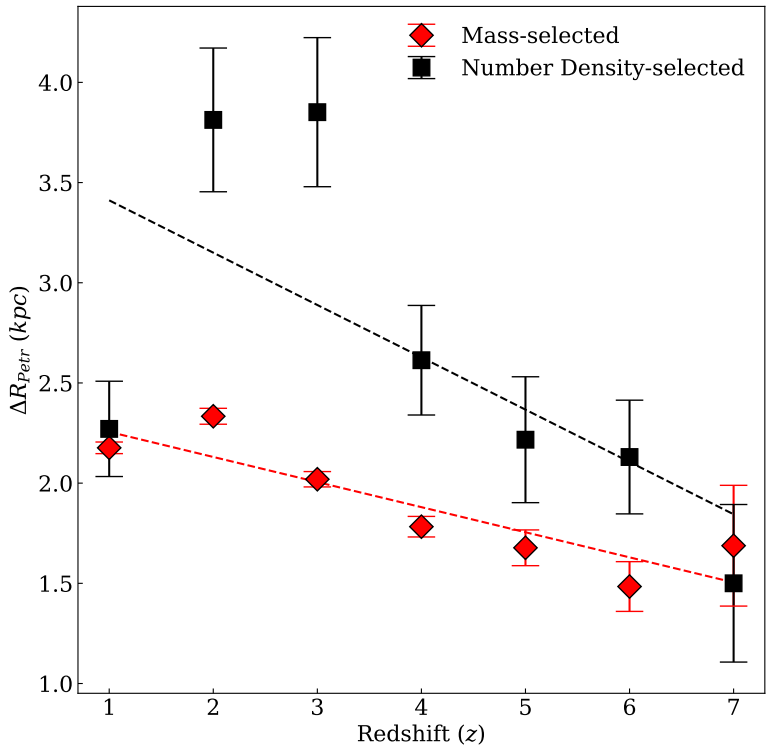

Figure 2.11: Evolution in the normalised median difference between $R_{\rm Petr}(\eta = 0.2)$ and $R_{\rm Petr}(\eta = 0.8)$ for each redshift bin. This parameter, $\Delta R_{\rm Petr}$, is shown in Equation 2.8. The mass-selected sample is shown as the red diamonds and the number density-selected sample is shown as the black squares. For both samples, there is an increase in $\Delta R_{\rm Petr}$. The number of galaxies in each redshift bin are the same as in Figure 2.9 for the mass-selected sample and Figure 2.10 for the number density-selected sample.

2.4.7 Galaxy Merger Sizes

It has long been shown that galaxies increase in size as redshift decreases (e.g., Daddi et al., 2005; Trujillo et al., 2007; Buitrago et al., 2008; Cimatti et al., 2008; van der Wel et al., 2008; van Dokkum et al., 2008; Cassata et al., 2010) but the method through which this occurs is largely unknown. We examine a sample of galaxies classified as mergers and non-mergers in order to determine whether this is a potential factor in causing the increase in size.

We identify a sample of mergers and non-mergers from the mass-selected sample by utilising the CAS approach (Conselice, 2003) whereby merging galaxies are those with a high asymmetry that is larger than the clumpiness. We use the condition

$$(A > 0.35)\ \&\ (A > S) \tag{2.9}$$

to define our sample. This method predominantly identifies only major mergers where the ratio of the stellar masses of the progenitors is at least 1:4 (Conselice, 2003, 2006; Lotz et al., 2008).

We show the evolution of the Petrosian radii at three different η values in Figure 2.12. Mergers are represented by circles and non-mergers are represented by triangles. The colours are the same as in Figure 2.9 where $R_{\rm Petr}(\eta = 0.2)$ is shown in blue, $R_{\rm Petr}(\eta = 0.5)$ is shown in orange, and $R_{\rm Petr}(\eta = 0.8)$ is shown in green. For both mergers and non-mergers, the radius decreases as redshift increases irrespective of the value of η. However, the non-mergers are on average smaller than the mergers at the same redshift despite having similar masses of $10^{9.5} M_{\odot}$ and $10^{9.4} M_{\odot}$ respectively. The outermost radii change the most significantly for mergers and non-mergers, changing by factors of 3.14 ± 0.49 and 4.38 ± 0.46 respectively. $R_{\rm Petr}(\eta = 0.8)$ changes the least with

mergers and non-mergers evolving by factors of 2.62 ± 1.84 and 3.28 ± 0.18 respectively. This is a sign that there is more evolution in the outer radii sizes for mergers than for normal galaxies. During the merger process we see that galaxies are getting larger not in their centers but in their outer parts. This is further evidence for our observational picture that galaxies are forming from the inside-out.

2.5 Discussion

Using the GOODS-North and GOODS-South fields of the CANDELS dataset, we present an analysis of the sizes of a sample of galaxies in the redshift range $1 \leq z \leq 7$. We also present a new method of removing nearby unrelated field objects from images by making use of a 2-dimensional Lyman-break method at λ_{rest} = 912 Å. Using these processed images, we measure the redshift-independent Petrosian radius of each galaxy at η values of 0.2, 0.5, and 0.8 and determine how these radii change with redshift. The measured radii are then corrected to remove any effects from the PSF.

At high redshifts i.e. $z > 3$, the size distribution of the galaxies within the full sample is dominated by galaxies with a small Petrosian radius with the median size increasing as redshift decreases. This is true for all values of η. Typically the effective radius has been used to measure the size evolution of galaxies. For example, Shibuya et al. (2015) find sizes that decrease significantly toward high z, no matter what statistic is used. In addition, a small sample of galaxies at $z \sim 9 - 10$ studied by Holwerda et al. (2015) were found to have mean size of 0.5 ± 0.1kpc which is consistent with extrapolated low-redshift data.

In order to remove biases introduced by the detection limits of the surveys, we select a mass-complete sample of galaxies from the main sample within the mass range $10^9 M_\odot \leq M_* \leq 10^{10.5} M_\odot$. At $z = 7$, we find the average size of a galaxy is

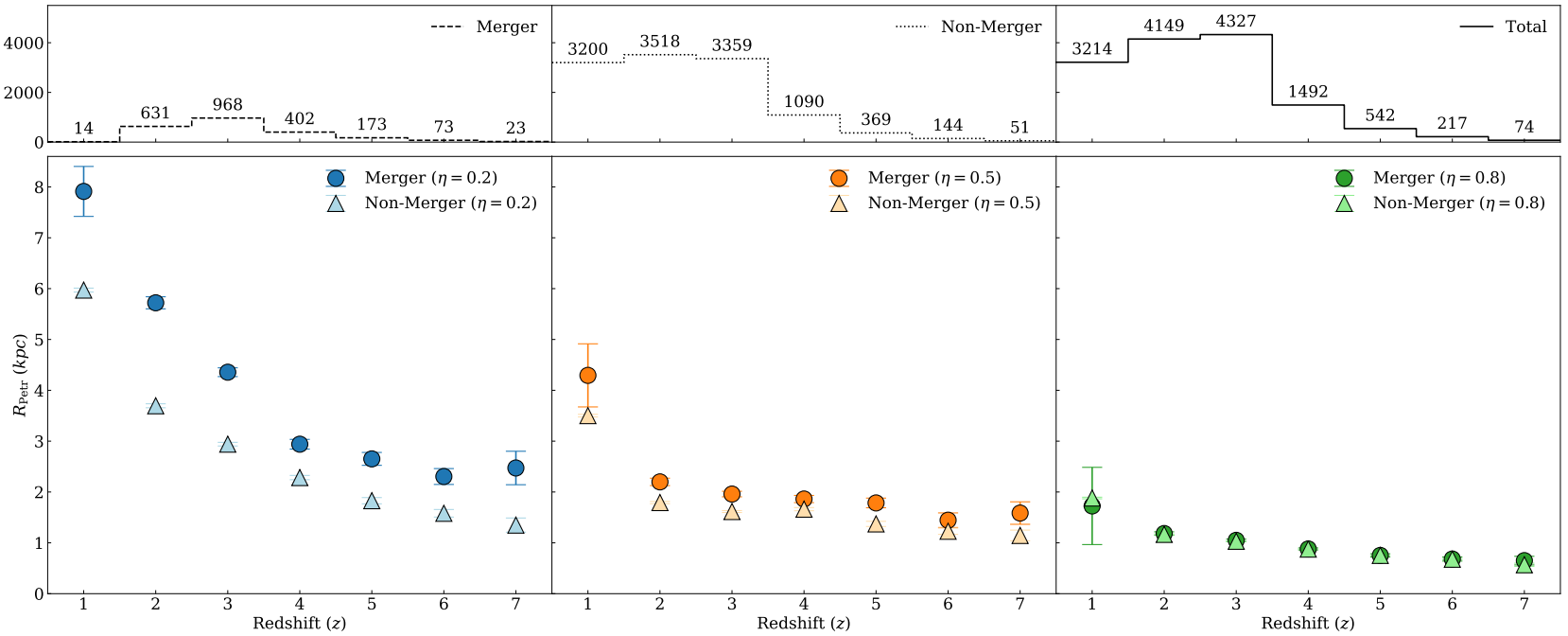

Figure 2.12: Top: numbers of galaxies in each redshift bin for the mergers (left), non-mergers (middle) and the total mass-selected sample (right). Bottom: evolution of the median Petrosian radius for mergers and non-mergers within the mass-selected sample. The error bars represent the standard error, some of which are smaller than the point size. Mergers are shown by circles and non-mergers are shown by triangles. The Petrosian radius is plotted for the three different η values with $\eta = 0.2$ shown in blue (left), $\eta = 0.5$ in orange (centre), and $\eta = 0.8$ in green (right). For all redshifts, the mergers are larger on average than the non-mergers but similar at larger η.

$R_{\rm Petr}(\eta = 0.2) = 1.58 \pm 0.16$ kpc, a factor of 3.78 ± 0.39 smaller than $R_{\rm Petr}(\eta = 0.2)$ at $z = 1$. By applying a simple power-law fit to each of the radii, we see the radii change as $(1 + z)^{\beta}$ where $\beta < 0$ in Figure 2.9. We fit $\beta = -0.97 \pm 0.03$ for $R_{\rm Petr}(\eta = 0.2)$ and $\beta = -0.80 \pm 0.03$ for $R_{\rm Petr}(\eta = 0.8)$ which shows that the size evolution is, on average, faster for the outer regions of the galaxies than for the inner regions. These fits are however shallower than other studies that use a simple fitted half-light radius e.g. Allen et al. (2017) who find $\beta = -0.89$ for a mass-complete ($M_* > 10^{10} M_{\odot}$) sample of galaxies from the FourStar Galaxy Evolution Survey over a redshift range of $z = 1 - 7$. Similarly, van der Wel et al. (2014) determine the size evolution of a sample of galaxies with $M_* \sim 10^{10} M_{\odot}$ to be steep with $\beta = -1.1$.

A similar result is achieved when measuring the sizes of a number density-selected sample at a limit of 1×10^{-4}Mpc^{-3}. The median size for this selection at $z = 7$ is 1.64 $\pm$ 0.24 kpc, a number similar to that found at the same redshift for the mass-selected sample. The value at $z = 1$ for the number density-selected sample is a factor of $3.39 \pm$ 0.54 larger than that at $z = 7$. The size evolution for this sample therefore evolves at a similar rate to the previous mass-selected sample.

We again find that the evolution can be fit as a power-law of the form $(1 + z)^{\beta}$. For $R_{\rm Petr}(\eta = 0.2)$, we find $\beta = -0.82 \pm 0.14$ and for $R_{\rm Petr}(\eta = 0.8)$, we find $\beta = -0.67 \pm 0.11$. The result for the outermost radius is consistent with that of Bouwens et al. (2004) who find $\beta = -1.05$ and Oesch et al. (2010) who find $\beta = -1.12$ for their samples. In comparison Patel et al. (2013) select galaxies using a number density of 1.4×10^{-4}Mpc^{-3} and find a value of $\beta = -1.16$ for quiescent galaxies which is slightly higher. The results found by these previous works are determined using the effective radii of galaxies.

Independent of the selection method used, the outer radii of galaxies evolve with a steeper slope than the inner radii suggesting that the outer regions are growing more rapidly. This therefore suggests that mass is added to the outer regions in an inside-out

formation mode. This difference in evolution between $R_{\rm Petr}(\eta = 0.2)$ and $R_{\rm Petr}(\eta = 0.8)$ is highlighted in Figure 2.11. For each selection method, the value of $\Delta R_{\rm Petr}$ increases with time, showing that the outermost radius increases at a greater rate than the innermost radius.

We furthermore split the mass-selected sample into mergers and non-mergers based on the measured CAS values. We examine this as the merging of galaxies is a dominant method for forming distant galaxies and therefore we can determine how the size distribution changes during this process. Figure 2.12 shows that each of the different radii increase as redshift decreases for both mergers and non-mergers however on average, mergers are larger. As with the previous samples, $R_{\rm Petr}(\eta = 0.2)$ changes the most significantly with mergers changing by a factor of 3.11 ± 0.81 and non-mergers evolving in size by a factor of 3.98 ± 0.41. $R_{\rm Petr}(\eta = 0.8)$ changes the least with mergers and non-mergers changing by factors of 2.07 ± 0.24 and 2.31 ± 0.13 respectively. The outer radii change to a higher degree for mergers compared to the non-mergers, again suggesting a inside-out formation scenario whereby galaxy formation events increase the outer sizes more than the inner radii.

This inside-out growth could be due to a number of factors with these results suggesting accretion of satellite galaxies being an important one (e.g., Ferreras et al., 2014; Huertas-Company et al., 2016a; Buitrago et al., 2017). Miller et al. (2019) suggests the growth of the inner parts of galaxies is related closely to the star formation whereas the growth of the outer regions is linked to accretion and the relationship with galactic halos. By measuring R_{20} and R_{80} as opposed to the half-light radius which is more commonly used, star forming galaxies are found to be larger than quiescent galaxies in the inner regions (R_{20}) but the difference between the sizes of star forming and quiescent galaxies disappears at R_{80}.

The results we find are consistent with previous work. For example, Margalef-

Bentabol et al. (2016) determine the size evolution of a sample of two-component galaxies with stellar masses $M_* > 10^{10} M_\odot$ from CANDELS. The circularised effective radius of each of the components is measured and the outer components are found to increase in size from $z = 3$ to $z = 1$ by a factor of 2 whereas the bulges, or inner components, remain roughly constant over the same redshift range. It is concluded that this suggests inside-out formation with the bulges being in place early on in a galaxy's history. Carrasco et al. (2010) also find a similar result; by using observations of massive ($M_* \sim 4 \times 10^{11} M_\odot$) galaxies from the Palomar Observatory Wide-Field Infrared survey, the outer regions of low-z elliptical galaxies are shown to be denser than the high-z compact massive galaxies by a factor of ~ 2, confirming that mass is added in the outer edges. Therefore, it is now commonly seen in all studies that galaxies are growing in an inside-out fashion.

2.6 Conclusions

The details of the processes that lead to the growth of galaxies through time are still largely unknown, but by measuring sizes using redshift-independent relative surface brightness metrics, it is possible to determine where the size of a galaxy grows most rapidly, and therefore suggest how galaxies grow. In this chapter, we present a new method of removing foreground objects from images of galaxies that makes use of the Lyman break at 912 Å. This allows us to reduce the risk of contamination from other objects when measuring the sizes and other properties of galaxies. The images we use to make our measurements are in the optical rest-frame at $\lambda \cong 4000$ Å wherever possible. However, due to the limited availability of *HST* bands, this is not possible for galaxies at $z > 3$ where we are forced to probe galaxy sizes in progressively bluer wavelengths down to the UV. We calculate the Petrosian radii of three different samples of galaxies

selected from the CANDELS GOODS-North and GOODS-South fields and determine how these radii evolve with redshift from $z = 7$ to $z = 1$. We use the Petroisan radius as a proxy for size throughout. Overall, we find an increase in size from $z = 7$ to $z = 1$ with the outer radii increasing the most rapidly over this redshift range. This rapid growth in the outer edges suggests an inside-out formation process is causing the overall growth in galaxy size.

We also determine how size evolves for a sample of mergers and non-mergers and find that mergers are, on average, larger than non-mergers at the outer radii for a given redshift. The outer radii evolve more rapidly than the inner radii, further supporting the idea that the size evolution of galaxies is caused by an inside-out formation process e.g. the accretion of satellite galaxies, mergers, and accretion of gas from the intergalactic medium.

Chapter 3

Surface Brightness Evolution of Galaxies in the CANDELS GOODS Fields up to $z \sim 6$: High-z Galaxies are Unique or Remain Undetected

3.1 Introduction

When studying and examining galaxy evolution as a function of redshift it is common to observe and characterise how quantities evolve with redshift to infer evolution. These quantities are most famously the ultraviolet (UV) luminosity function (LF) (e.g., Arnouts et al., 2005; McLure et al., 2013; Bouwens et al., 2015), the stellar mass function (e.g., Duncan et al., 2014; Bhatawdekar et al., 2019), the spectral shape of the UV light distribution (e.g., McLure et al., 2018), morphological evolution (e.g., Conselice & Arnold, 2009) as well as the merger and pair fraction evolution (e.g., Duncan et al.,

2019).

Galaxy surface brightness (SB) has previously been studied in the optical and near-infrared at low redshifts (Schade et al., 1995; Roche et al., 1998; Labbé et al., 2003; Barden et al., 2005). Such studies find mixed results with some suggesting there is evolution in the surface brightness (e.g., Schade et al., 1996) and others suggesting it does not exist or is due to selection effects (e.g., Simard et al., 1999). Higher redshift galaxies have been examined in the context of gas, star formation, and star surface density but rarely explicitly in the form of surface brightness for the last decade or so. However these density relations are similar to the SB problem. Since the low redshift studies, larger and deeper surveys have taken place allowing us to now look further and deeper into the evolution of surface brightness of galaxies, and to do so at a consistent rest-frame wavelength. With modern deep imaging data from the *Hubble Space Telescope*, it is possible to investigate the evolution of surface brightness as measured in the UV and determine how it evolves in terms of intrinsic surface brightness, and what this evolution implies for galaxy formation, star formation, dust, as well as galaxy detection. Surface brightness in the UV rest-frame is a good indicator of star formation density and gas density (Schmidt, 1959; Kennicutt, 1998; Leroy et al., 2008; Freundlich et al., 2013), and thus enables an understanding of how these quantities change with time to first order. Star formation density has been shown to increase to a peak between $z \sim 1$ and $z \sim 2$, before becoming nearly constant to high redshift for Lyman break galaxies (e.g., Steidel et al., 1999; Giavalisco et al., 2004). Observations from the *Hubble Space Telescope* show a small amount of evolution at $z > 3$ (Bouwens et al., 2003) and those measurements that are made using photometric redshifts show constant star formation up to $z \sim 6$ (Thompson et al., 2001; Kashikawa et al., 2003). Surface brightness also determines how well galaxies can be detected and in this chapter we investigate both of these problems.

When measuring the surface brightness of a given galaxy it is now well known that this value is constant for the same galaxies seen at different distances in the nearby universe. However, when a galaxy is at cosmological distances, the surface brightness becomes lower by a significant amount that scales with redshift (z) as $(1 + z)^{\alpha}$, where α can range from 3 to 5 depending on the particular circumstances (Tolman, 1930, 1934). One result of this is that the observability of galaxies which would normally be detectable would have such a low surface brightness that even with deep *Hubble Space Telescope* exposures, it would not be possible to detect them at higher redshifts.

The literature on the evolution of SB is however not entirely consistent on how this evolution occurs. Previous studies of the rest-frame surface brightness evolution of disk galaxies find mixed results ranging from little or no evolution to a difference of ∼1-2 mag between the local Universe and $z \sim 1$. For example, Labbé et al. (2003) use ground-based near-infrared imaging and find an increase of 1 mag out to $z \sim 2 - 3$ for six Milky Way-type galaxies. Schade et al. (1996) also use ground-based imaging but find a stronger evolution of 1.6 mag from $z \sim 1$ for a larger sample of 143 galaxies (33 early-type and 110 late-type). These results are also found in *Hubble Space Telescope* observations; Schade et al. (1995), Lilly et al. (1998), Roche et al. (1998) and Barden et al. (2005) who find an average increase in surface brightness of ~ 1 mag by $z \sim 1$ for a mixture of both spiral and elliptical galaxies.

In terms of surface brightness and selection, Simard et al. (1999) identify the need for selection effects to be taken into account when probing higher redshifts, and this is another reason why studying the evolution of SB is important. Before taking selection effects into account, Simard et al. (1999) find a change of 1.3 mag from $z \sim 1$ to $z \sim 0$ but once these effects are considered, no evolution in the surface brightness is seen. Similarly, Ravindranath et al. (2004) find a change in surface brightness of < 0.4 mag over the range $0.2 < z < 1.25$ in the z-band for disk like galaxies when

considering selection effects. These studies show that there are relatively bright galaxies in the highest redshift bins. Trujillo & Aguerri (2004) also take selection effects into account in their analysis, a change of ~ 0.8 mag from $z = 0.7$ to $z = 0$ is found when measuring the surface brightness in the V-band. Models supporting an increase in surface brightness include Bouwens & Silk (2002) who model disk evolution based on two different approaches. Both models find a strong evolution in the B-band surface brightness of 1.5 mag by $z = 1$, and it is argued that these results are not an artefact of selection effects.

These works are limited to relatively low redshift objects, where the cosmological SB dimming is not as dramatic as it is at higher redshifts and to the optical rest-frame. As higher redshift data from surveys such as the Cosmic Assembly Near-infrared Deep Extragalactic Survey (CANDELS) is now available, it is now possible to probe how the surface brightness of galaxies changes with time, and infer the processes that cause this evolution over ~ 12 Gyr of cosmic time for the UV rest-frame.

We examine the evolution of the UV rest-frame ($\lambda \sim 2000$ Å) surface brightness through the redshift range of $0.5 < z < 6.5$. We also examine the relationship between the surface brightness with star formation rate (SFR). In order to reduce any biases in the results, we use a mass-selected sample that is >95% complete (Duncan et al., 2019). We also examine a separate number density-selected sample. Stellar mass incompleteness is an important factor to consider when examining galaxies at high redshift as due to detection limits, some galaxies will be missed in observations. We explore this incompleteness in our sample in order to see how this affects our surface brightness measurements.

This chapter is structured as follows. In §3.2 we describe the data and the sample. In §3.3 we describe the method used. In §3.4 we present our main results, and in §3.5 we discuss our findings. Finally, we conclude in §3.6. Throughout this chapter we use

AB magnitudes and assume a Λ-CDM cosmology with $H_0 = 70$ kms^{-1}Mpc^{-1}, $\Omega_m = 0.3$, and $\Omega_\Lambda = 0.7$.

3.2 Data and Sample Selection

For this work two samples of galaxies over the redshift range $0.5 < z < 6.5$ are selected from the Great Observatories Origins Deep Survey North and South (GOODS-N and GOODS-S respectively) fields (Giavalisco et al., 2004) from the Cosmic Assembly Near-infrared Deep Extragalactic Survey (CANDELS) (Grogin et al., 2011; Koekemoer et al., 2011). CANDELS is a Multi Cycle Treasury Programme which images objects using the Advanced Camera for Surveys (ACS) and the Wide Field Camera 3 (WFC3). In total, CANDELS covers an area of 800 arcmin^2 over five different fields. The GOODS-N and GOODS-S fields cover a combined area of 160 arcmin^2 and are centred on the Hubble Deep Field North and the Chandra Deep Field South (Giavalisco et al., 2004). CANDELS is divided into CANDELS/Deep which images both GOODS-N and GOODS-S to a 5σ depth of 27.7 mag in the H-band and CANDELS/Wide which images the fields to a 5σ depth of 26.3 mag in the H-band. For this work, we use the F435W, F606W, F814W, and F850LP images observed using the ACS and the F105W, F125W, and F160W images observed using the WFC3. These filters will be referred to as B_{435}, V_{606}, I_{814}, z_{850}, Y_{105}, J_{125}, and H_{160} from this point onwards.

In this work, we analyse two separate samples; a mass-selected sample and a number-density selected sample. The mass-selected sample is comprised of 1,522 galaxies that lie within the mass range $10^{10}M_\odot < M_* < 10^{11}M_\odot$ to ensure completeness (Duncan et al., 2019). The completeness limits at $z = 6$ are $\log_{10}(M_\odot) = 10$. The mass limits for $z < 6$ are considerably lower than our chosen mass limit of $10^{10}M_\odot$. The redshift and mass distributions of the galaxies within this sample are shown in the left panel of

Figure 3.1. The yellow regions indicate a high density of galaxies and purple indicates a lower density of galaxies.

The number density-selected sample is generated by using a constant number density of $1{\times}10^{-4}$ Mpc^{-3} (Ownsworth et al., 2016). This sample consists of 400 galaxies that have masses in the range $10^{9.5}M_{\odot} < M_{*} < 10^{11.8}M_{\odot}$. The redshift and mass distributions within the number density-selected sample are shown in the right panel of Figure 3.1. As with the left panel, the yellow regions indicate a high density of galaxies and purple indicates a lower density of galaxies. This sample is chosen as it potentially allows us to directly track the progenitors and descendants of massive galaxies at all redshifts (e.g., Mundy et al., 2015; Ownsworth et al., 2016). In the following subsections we discuss how we measured photometric redshifts and stellar masses for our sample of galaxies. There are a small number of high-z galaxies with high masses in this sample that are unlikely to be real, however these galaxies do not affect our results.

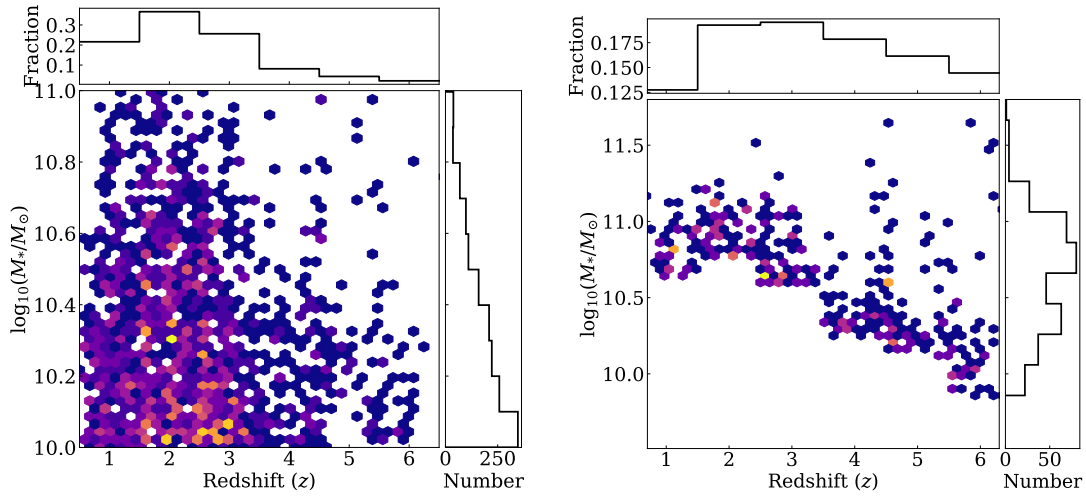

Figure 3.1: Left: redshift and mass distributions of the mass-selected sample. Right: redshift and mass distributions of the number density-selected sample. In both, yellow indicates an increased density of points and purple indicates a low density.

3.2.1 Photometric Redshifts and Stellar Mass Fitting

We use the same methods as in 2.2.1 in order to determine the photometric redshifts and stellar masses of the galaxies within our sample.

3.2.2 Star Formation Rates

The star formation rates we use in this chapter are determined through spectral energy distribution (SED) fitting. The measured rest-frame absolute magnitudes (M_{1500}) are corrected for dust extinction using the relation determined by Meurer et al. (1999). Where the relation implies a negative extinction, the extinction is set to 0. The UV star formation rates are calculated using the following:

$$SFR\ (M_{\odot}\ \mathrm{yr}^{-1}) = \frac{L_{UV}\ (\mathrm{erg\ s^{-1}\ Hz^{-1}})}{1.39 \times 10^{27}} \tag{3.1}$$

where the conversion factor of Madau et al. (1998) and Kennicutt (1998) is used. For further details, see Duncan et al. (2014) and Duncan et al. (2019).

3.3 Methodology

3.3.1 2D Lyman-break Imaging

We utilise the same image processing technique described in 2.3.1 however in this case, we use the UV rest-frame as opposed to optical. The bands used are given in Table 3.1, along with the rest-frame wavelength we probe at each redshift. This 2D Lyman break imaging method removes all nearby galaxies and only retains the original system. We do this to avoid contamination from foreground objects, utilising the fact that the Lyman

Table 3.1: The bands used to complete the image processing for each redshift in Column 1. Column 2 gives the band corresponding to the UV rest-frame ($O_{i,j}^{raw}$), and Column 3 gives the band corresponding to the Lyman-break where applicable ($D_{i,j}^{raw}$). Column 4 gives the rest-frame wavelength probed.

z	$O_{i,j}^{raw}$	$D_{i,j}^{raw}$	λ_{rest}
1	B_{435}	-	2175 Å
2	V_{606}	-	2020 Å
3	I_{814}	-	2035 Å
4	z_{850}	B_{435}	1700 Å
5	Y_{105}	B_{435}	1750 Å
6	J_{125}	V_{606}	1785 Å

break allows us to find which systems are at a different redshifts of the principal galaxy we are looking at.

3.3.2 Size Measurement & Magnitude Determination

In this work we use the Petrosian radius ($R_{\rm Petr}(\eta)$) to measure the sizes of our galaxies (e.g., Whitney et al., 2019). The radius we use for sizes, defined by the Petrosian index, is also the radius we use to measure the magnitude of the galaxy. The Petrosian radius is defined as the radius at which the surface brightness at a given radius is a particular fraction of the surface brightness within that radius (e.g., Bershady et al., 2000; Conselice, 2003). The Petrosian radius and the way in which it measured are described in further detail in 2.3.2. We correct the sizes for point spread function (PSF) effects by simulating a sample of galaxies and applying the WFC3 PSF to images of these galaxies, as described in Whitney et al. (2019).

In order to calculate the surface brightness, we first calculate the magnitude, m, within an aperture of radius $R_{\rm Petr}$ by measuring the flux within this aperture. From this magnitude, we are able to determine the observed surface brightness and the intrinsic surface brightness, as explained below.

3.3.3 Surface Brightness Dimming

Below we give a detailed description of our derivation for how the surface brightness of a galaxy changes due to cosmological effects. There are many papers on this in the past (Tolman, 1930, 1934; Giavalisco et al., 1996; Conselice, 2003) however, we rederive the net correction for the dimming in our own specific situation whereby we are observing the same rest-frame wavelength, but in different observed filters, at different redshifts. Note that all situations in surface brightness dimming are unique and the derivation below is focused on our own situation.

It is well known that the measured surface brightness of a given galaxy is not constant with redshift, and that objects are subject to surface brightness dimming whereby an object at redshift z_1 is a factor f dimmer in surface brightness than the same object at redshift z_2 where $z_1 > z_2$ Tolman (1930, 1934). There are 5 factors of $(1 + z)$ that need to be taken into account when considering surface brightness dimming; two factors of $(1 + z)$ arise from the fact that the source was closer to the observer when the light was emitted. This causes the object to look larger by a factor $(1 + z)$ in two dimensions. One factor of $(1 + z)$ arises from a change in the rate of photons being received from the source. Another factor is the result of photons shifting to a lower energy as they propagate from the source to the observer. The final factor comes from the change in the unit wavelength bandpass. When considering the integrated flux, the final factor does not apply. This is consistent with the argument made by Tolman (1930) whereby galaxies dim with redshift by a factor of $(1 + z)^4$. Here we consider the flux density measured in units of f_ν. Therefore, the redshift dependence is reduced to $(1 + z)^3$.

We carry out a detailed derivation on a step by step basis so that other situations can be adopted using our methodology. First, when considering the spectral flux density in units of f_λ (erg s^{-1} cm^{-2} Å^{-1}), as used in Space Telescope (ST) magnitudes, there are

five factors of $(1 + z)$ to consider when calculating how much the surface brightness reduces by in terms of a bolometric flux. One term of $(1 + z)$ originates from the energy reduction of a photon. When a photon is emitted, it has a wavelength λ_{emit} and has energy E_{emit} given by

$$E_{emit} = \frac{hc}{\lambda_{emit}}. \tag{3.2}$$

We know that observed wavelength, λ_{obs}, is a factor of $(1 + z)$ larger than the emitted wavelength due to redshift, therefore, the observed energy, E_{obs}, is given by

$$E_{obs} = \frac{hc}{\lambda_{emit}(1 + z)}. \tag{3.3}$$

From this, we can say that the energy is a factor of $(1 + z)$ smaller at the time of observation than at the time of emission, giving the first factor of $(1 + z)$.

Another factor is due to time dilation; two photons emitted in the same direction δt_{emit} are separated by a proper distance $c \times \delta t_{emit}$. At observation, the proper distance is $c \times \delta t_{emit} \times (1 + z)$. The two photons are then detected at a rate of

$$\delta t_{obs} = \delta t_{emit}(1 + z). \tag{3.4}$$

This yields a second factor of $(1 + z)$. The two factors that are due to energy reduction and time dilation are the two factors associated with the luminosity distance d_L. The luminosity distance d_L is used when determining the flux emitted from an object with luminosity L:

$$f = \frac{L}{4\pi d_L^2}. \tag{3.5}$$

the luminosity distance is related the the transverse comoving distance r by the relation

$$d_L = r(1+z). \tag{3.6}$$

We can therefore express the flux in terms of the luminosity distance as:

$$f = \frac{L}{4\pi r^2 (1+z)^2}. \tag{3.7}$$

The two factors in the denominator are due to the energy and time dilation effects as described above. The third and fourth factors arise from the change in angular size of the object; for an object of diameter d and angular size $\delta\theta$, the angular diameter distance is given as:

$$d_A = \frac{d}{\delta\theta}. \tag{3.8}$$

For a flat Universe, the angular diameter distance is given by

$$d_A = \frac{r}{(1+z)}. \tag{3.9}$$

Substituting this into Equation 3.7, we see that the flux is reduced by a factor of $(1+z)^4$ due to redshift:

$$f = \frac{L}{4\pi d_A^2 (1+z)^4}. \tag{3.10}$$

The fifth and final factor arises due to the change in unit bandpass wavelength from emission to detection. A filter has central wavelength λ and width $\Delta\lambda$. Both the observed central wavelength and the observed band width increase by a factor of $(1+z)$. For a

fixed filter width this results in a reduction of observed flux from a galaxy. The observed bandpass wavelength can therefore be given as

$$\lambda_{obs} = \lambda_{emit}(1+z) + \Delta\lambda_{emit}(1+z). \tag{3.11}$$

From these arguments, we can see that

$$f_\lambda \propto (1+z)^{-5} \tag{3.12}$$

in units of erg s^{-1} cm^{-2} $Å^{-1}$, or ST magnitudes, where μ_{int} is the intrinsic surface brightness.

In the case of the spectral flux density is units of f_ν (erg s^{-1} cm^{-2} Hz^{-1}), as used in AB magnitudes, we must consider the first four factors described above (energy, time dilation, angular size). However we must consider the change in unit frequency as opposed to the change in unit wavelength. As frequency is inversely proportional to wavelength, the frequency interval decreases by a factor of $(1+z)$ from emission to detection. From this, we find that

$$f_\nu \propto (1+z)^{-3} \tag{3.13}$$

in units of erg s^{-1} cm^{-2} Hz^{-1}, or AB magnitudes. We use this factor of $(1+z)$ throughout the remainder of this work when comparing the measured surface brightness at different redshifts as derived in Equation 3.13.

We use the factor of $(1+z)^4$ when artificially redshifting galaxies, as described below in §3.3.5. Overall, the surface brightness dimming factor used when considering the integrated flux (erg s^{-1} cm^{-2}) includes the factors that are a result of energy reduction,

time dilation, and change in size. Therefore, objects are subject to a cosmological dimming factor of $(1+z)^{-4}$. This is also the case when considering pixel values of an image, where the pixel values are in units of photons $s^{-1}cm^{-2}Å^{-1}$.

3.3.4 Surface Brightness: Observed and Intrinsic

One of the main goals of this chapter is to examine the intrinsic evolution of the surface brightness for galaxies up to $z = 6.5$. However, this is a derived quantity that must be calculated based on the observed surface brightness, and assuming that cosmological dimming is taking place. As such, we examine in this chapter both the observed and the derived intrinsic SB evolution.

First, we describe the method in which we use to derive the intrinsic surface brightness from the observations. The observed surface brightness is given by

$$\mu_{obs} = m + 2.5\log_{10}(\pi R^2_{\rm Petr}) \tag{3.14}$$

where m is the apparent magnitude discussed in §3.3.2 and $R_{\rm Petr}$ is the Petrosian radius of the galaxy in which that magnitude is measured. The apparent magnitude is calculated from the measured flux within the measured Petrosian radius $R_{\rm Petr}$. As we are measuring fluxes in the AB magnitude system, this surface brightness should be corrected by surface brightness dimming of the form:

$$\mu_{int} = m + 2.5\log_{10}(\pi R^2_{\rm Petr}) - 2.5\log_{10}((1+z)^3). \tag{3.15}$$

We use Equation 3.15 to calculate the intrinsic SB for the systems we detect, within the observed SB given by Equation 3.14. Throughout the rest of this chapter we use

these SB values to understand the physical evolution and selection effects present within deep surveys such as CANDELS. As explained in §3.3.3, we use a factor of $(1+z)^4$ to determine the amount of cosmological dimming experienced by a galaxy when being artificially redshifted from a redshift z_1 to a higher redshift z_2.

3.3.5 Artificially Redshifted Galaxies

One of the tools we use to determine whether galaxies observed at low redshift (z_1) would be detectable at higher redshift (z_2), is by artificially redshifting galaxies in our sample from low redshift to high redshift. We start by examining a representative simulation by taking galaxies from $z_1 = 2$ and simulating how they would appear within the CANDELS data at $z_2 = 6$. This procedure is done by multiplying the V_{606} image by the factor $\left(\frac{1+z_1}{1+z_2}\right)^4$ and inserting this into the background of the J_{125} mosaic image whose noise is reduced by a factor defined as,

$$f = \frac{1}{1 - \left(\frac{1+z_1}{1+z_2}\right)^4}, \tag{3.16}$$

to ensure we are not overestimating the background. We also include luminosity evolution in the form of the difference between the characteristic magnitudes (ΔM^*) of the UV luminosity functions for each redshift. The values for $1 \leq z \leq 3$ are taken from Arnouts et al. (2005) and the values for $4 \leq z \leq 7$ are taken from Bouwens et al. (2015). The redshifting process is therefore described by the equation

$$R_{i,j} = O_{i,j} \cdot \left(\frac{1+z_1}{1+z_2}\right)^4 \cdot \Delta M^* + \frac{N_{i,j}}{f} \tag{3.17}$$

where $R_{i,j}$ is the redshifted image, $O_{i,j}$ is the rest-frame UV image at $z = 2$, and $N_{i,j}$

is the background noise. Figure 3.2 shows an example of this redshifting technique, beginning at $z = 2$ and ending at $z = 6$. We then measure these galaxies using the CAS code (Conselice, 2003) in the same way would do on actual galaxies. We use this to measure the size (in this case, the Petrosian radius at $\eta = 0.2$, $R_{\rm Petr}$ and flux of each galaxy from which we can determine the measured surface brightness.

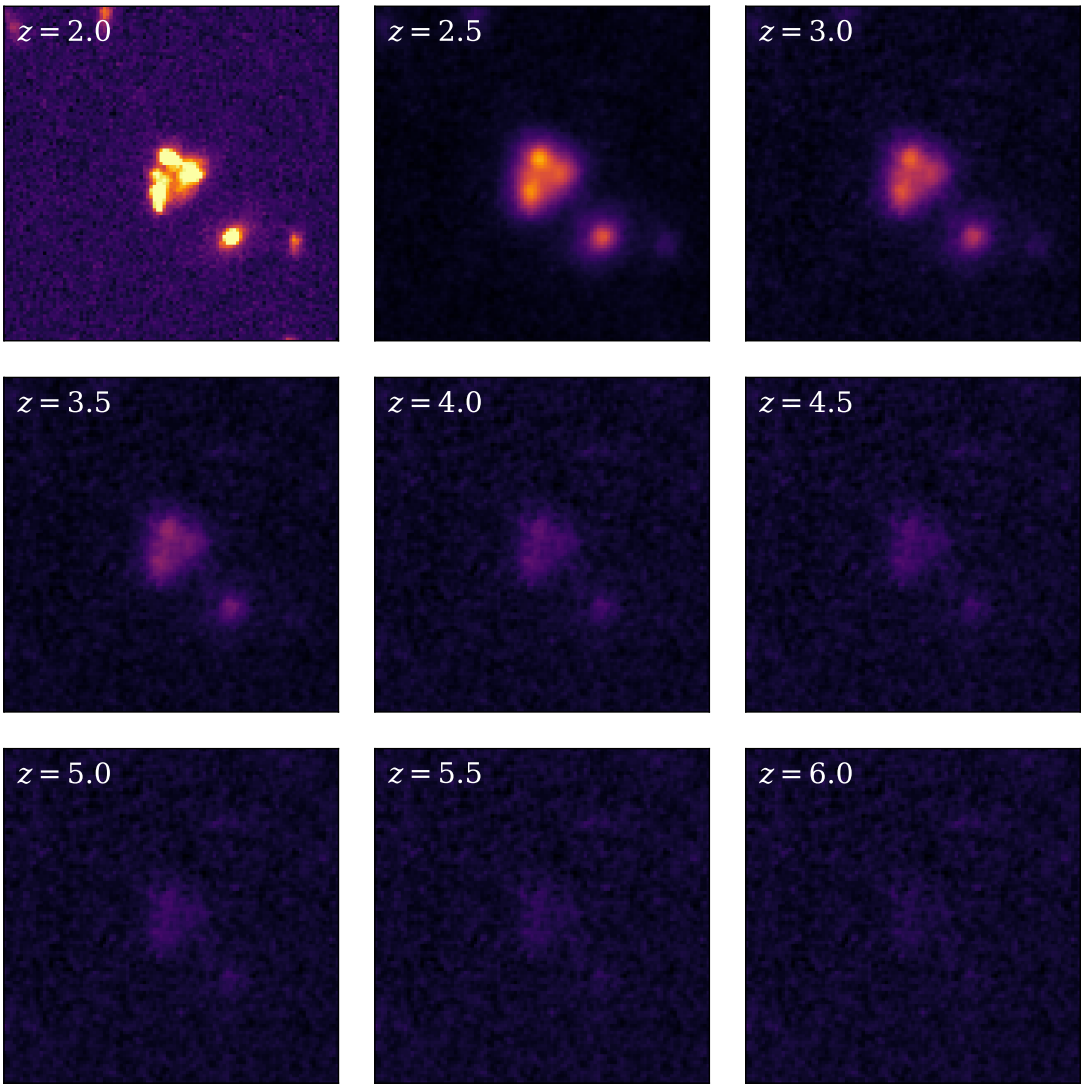

Figure 3.2: Example of the redshifting process beginning with a $z = 2$ galaxy (top left) and ending with the same galaxy redshifted to $z = 6$ (bottom right). The images in between correspond to the original galaxy redshifted in $\delta z = 0.5$ intervals. The image at each redshift interval has been evolved with the characteristic magnitude of that redshift (Arnouts et al., 2005; Bouwens et al., 2015).

We calculate a surface brightness completeness limit by examining the whole sample from which the two sub-samples are selected and determining at which magnitude the surface brightness function declines. This magnitude is then used to calculate the equivalent intrinsic surface brightness at each redshift.

3.4 Results

In this section we present the results we find when measuring the surface brightness of the galaxies using the two separate samples described in §3.2; a mass-selected sample where the galaxies lie within a mass range of $10^{10} M_{\odot} < M_{*} < 10^{11} M_{\odot}$ and a number density-selected sample where each redshift bin contains galaxies such that a number density selection is used at the constant value of 1×10^{-4} Mpc^{-3} with a mass range of $10^{9.5} M_{\odot} < M_{*} < 10^{11.8} M_{\odot}$. This particular method of selecting galaxies allows us to trace how the most massive galaxies have evolved in SB over time.

3.4.1 Observed Surface Brightness as a Function of Redshift

Throughout this work we measure all sizes and fluxes in the UV rest-frame between 1785 Å, and 2175 Å. Surface brightness is variant with wavelength, hence the need for a consistent rest-frame wavelength across redshifts. The UV rest-frame is also useful for tracing the star formation within galaxies. One downside of using the UV is that we are not able to trace the underlying older stellar mass formed within these galaxies. We are only tracing the young stars and the effects of dust on this light.

Before applying mass and number density cuts to the data, we examine the observed surface brightness distribution of the full sample of ~34,000 galaxies obtained from the CANDELS GOODS-North and GOODS-South fields. These galaxies lie in the redshift

range $0.5 < z < 6.5$ and have stellar masses in the range $10^6 M_\odot < M_* < 10^{12} M_\odot$. The observed surface brightness for each of these galaxies can be seen in Figure 3.3 before any cuts are performed. The average observed surface brightness of each redshift bin is given as a blue triangle, with an error of 1σ. There is a jump in μ_{obs} between redshifts $z = 3$ and $z = 4$ due to a difference in limiting magnitude of the filters, whereby F814W probing $z \sim 3$ is more sensitive than any redder filter with WFC3.

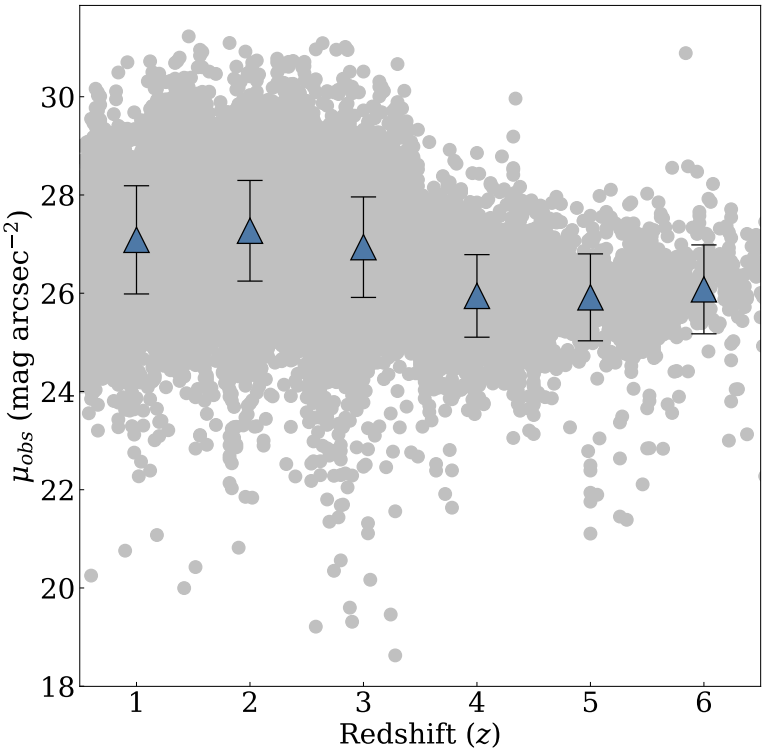

Figure 3.3: Observed surface brightness for the full sample from which the mass-selected and number density-selected samples are taken from. The average observed surface brightness for each redshift bin are shown as blue triangles with errors equal to 1σ. This is purely an observational result showing the range of surface brightness which we probe with our filters and exposures.

The evolution of the observed surface brightness (μ_{obs}) of the mass-selected sample can be seen in the left panel of Figure 3.4 with the mean surface brightness indicated for each redshift as orange circles. The same plot for the number density-selected sample can be seen in the right panel of Figure 3.4 with the mean surface brightness shown by

green circles. Both forms of the evolution are fit with a power law of the form:

$$\mu = \alpha(1+z)^{-\beta}. \tag{3.18}$$

The parameters determined for the fits are shown in Table 3.2. Both samples show a relatively flat evolution, increasing by 0.9 ± 1.5 mag arcsec^{-2} and 1.2 ± 1.4 mag arcsec^{-2} respectively. We correct the observed surface brightness for size evolution by setting the size of each galaxy to be the mean size of the $z = 6$ galaxies such that Equation 3.14 becomes

$$\mu_{obs} = m + 2.5\log_{10}(\pi R^2_{z=6}). \tag{3.19}$$

We plot these size corrected values as empty circles and fit these points with the power law given in Equation 3.18 and this is shown as a dashed line on both the left and right panels of Figure 3.4. We see that the size corrected values yield a shallower evolution whereby the difference between the surface brightness at $z = 1$ and $z = 6$ is now 0.4 $\pm$ 1.8 mag arcsec^{-2} and 0.1 $\pm$ 1.9 mag arcsec^{-2} for the mass-selected and number density-selected samples respectively.

When using more the more direct physical value of surface brightness in the form of measured flux per unit area in real units rather than logged, we find that the mass-selected sample evolves as $(1+z)^{0.25\pm0.71}$ and the number density-selected sample evolves as $(1+z)^{0.07\pm0.73}$. This method also suggests that the flux per unit area decreases with time.

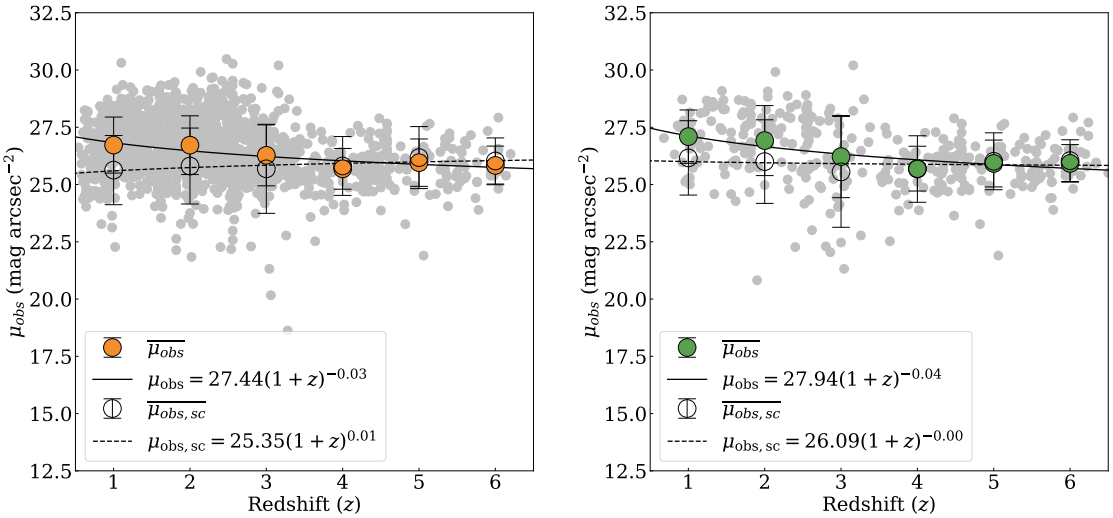

Figure 3.4: Left: evolution of the average observed surface brightness for the mass-selected sample. The mean surface brightness is shown for each redshift as orange circles. A power law is fit to the mean values and we find $\mu_{\rm obs} = 27.44 \pm 0.34(1+z)^{-0.03\pm0.01}$. This fit is shown as a solid line. The surface brightness is corrected for size by setting the sizes of all galaxies to the mean $z = 6$ galaxy size . These points are shown as empty circles. The fit to the points is shown as a dashed line and is found to be $\mu_{\rm obs} = 25.35 \pm 0.20(1+z)^{0.01\pm0.01}$. The error bars shown are 1σ from the mean. Right: evolution of the average observed surface brightness for the number density-selected sample. The mean surface brightness for each redshift is indicated by the green circles. The error bars shown are 1σ from the mean and a fit of the form $(1+z)^{-\beta}$ (solid line) have been fit to the data. The fit is found to be $\mu_{\rm obs} = 27.94 \pm 0.39(1+z)^{-0.04\pm0.01}$. The observed surface brightness is corrected for size, as shown by the empty circles. The power law fit of these values yields $\mu_{\rm obs} = 26.09 \pm 0.37(1+z)^{-0.00\pm0.01}$ and is shown as a dashed line.

3.4.2 Intrinsic Surface Brightness as a Function of Redshift

The intrinsic surface brightness (μ_{int}) varies with redshift such that galaxies at a low redshift are ~5 mag dimmer than those at the highest redshift. The evolution of μ_{int} can be seen in the left panel of Figure 3.5 for the mass-selected sample and in the right panel of Figure 3.5 for the number density-selected sample. The mean intrinsic surface brightness is indicated by the orange and green points respectively. We fit a power law to these mean values and these fits are indicated by a solid line in both cases. The parameters of the power law fits for both figures are shown in Table 3.2. Both samples

show a similar evolution, with the mass-selected sample evolving as $(1+z)^{-0.18\pm0.01}$ and the number density-selected sample evolving as $(1+z)^{-0.19\pm0.01}$. No matter the selection method, the intrinsic surface brightness changes by several mag arcsec^{-2} with the mass-selected sample changing by 4.8 ± 1.5 mag arcsec^{-2} and the number density-selected sample changing by 5.0 ± 1.4 mag arcsec^{-2}.

As for the observed surface brightness, we correct for size evolution for both samples by setting the size of each galaxy to the mean size of the $z = 6$ bin. Equation 3.15 therefore becomes

$$\mu_{int} = m + 2.5\log_{10}(\pi R^2_{z=6}) - 2.5\log_{10}((1+z)^3). \tag{3.20}$$

This is shown in the left (mass-selected) and right (number density-selected) panels of Figure 3.5 by the empty circles and a fit of the form $(1+z)^{-\beta}$ is shown as a dashed line for both samples. This size correction causes the evolution to flatten for both samples with β changing from 0.18 ± 0.01 to 0.13 ± 0.01 and 0.19 ± 0.01 to 0.15 ± 0.01 for the mass-selected and number density-selected samples respectively. This size correction also causes the difference in surface brightness between $z = 1$ and $z = 6$ to change to 3.5 ± 1.8 mag arcsec^{-2} and 3.9 ± 1.9 mag arcsec^{-2} for the two samples. This means that size can only account for about a magnitude of the evolution of galaxy surface brightness, with 3-4 mag arcsec^{-2} unaccountable for the fact that galaxies are growing in size within their Petrosian radius as they evolve from high to low redshift (e.g., Whitney et al., 2019). By examining the evolution of the size corrected surface brightness, a quantity that is linearly proportional to the luminosity, we are effectively examining the evolution of the absolute magnitude at a fixed size.

We also show the distribution of the surface brightness for the full mass-selected sample in Figure 3.6. This demonstrates a systematic evolution at all galaxy masses in

Table 3.2: The fits determined for both the mass-selected (M) and number density-selected (ND) samples as given by Equation 3.18.

	Sample	α	β
μ_{observed}	M	27.44 ± 0.34	-0.03 ± 0.01
	ND	27.94 ± 0.39	-0.04 ± 0.01
$\mu_{\text{intrinsic}}$	M	27.91 ± 0.51	-0.18 ± 0.01
	ND	28.31 ± 0.57	-0.19 ± 0.01

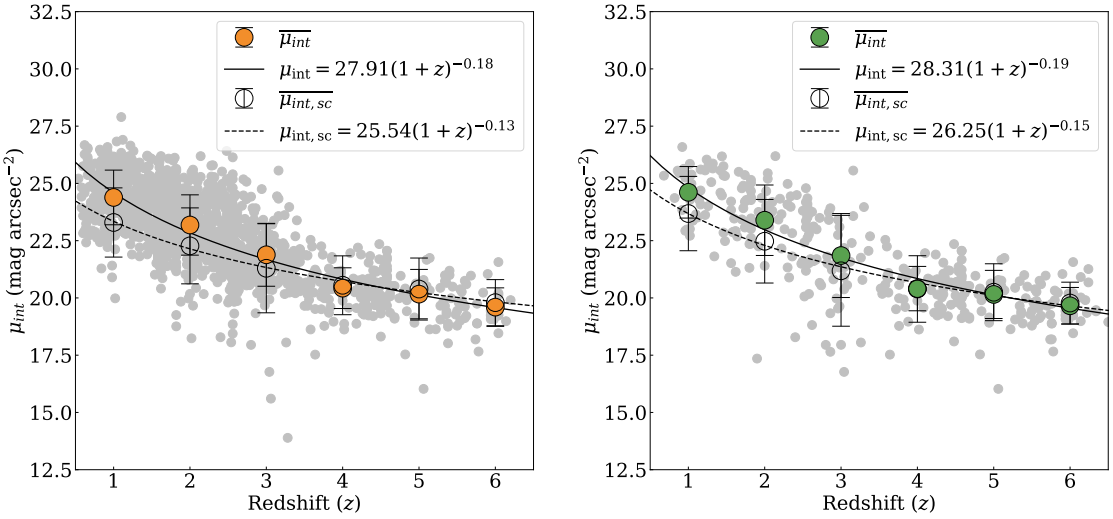

Figure 3.5: Left: evolution of the intrinsic surface brightness for the mass-selected sample with the mean surface brightness for each redshift bin shown by the orange circles. We fit a power law of the form $(1+z)^{-\beta}$ (solid line) and find $\mu_{\text{int}} = 27.91 \pm 0.51(1+z)^{-0.18\pm0.01}$. Also shown are the mean size corrected values (empty circles) and a power law fit to these points. This fit is found to be $\mu_{\text{int}} = 25.54 \pm 0.22(1+z)^{-0.13\pm0.01}$. The error bars shown are 1σ from the mean. Right: evolution of the intrinsic surface brightness for the number density-selected sample with the mean surface brightness for each redshift bin shown by the green circles. We fit a power law (shown by the solid line) and find $\mu_{\text{int}} = 28.31 \pm 0.57(1+z)^{-0.19\pm0.01}$. The mean size corrected surface brightness is also shown as empty circles, along with the fit to these points. The fit is found to be $\mu_{\text{int}} = 26.25 \pm 0.34(1+z)^{-0.15\pm0.01}$. The error bars shown are 1σ from the mean.

surface brightness such that, on average, galaxies at higher redshifts exhibit a higher intrinsic surface brightness, which then declines at lower redshifts. One caveat to this observation is that this is not necessarily a complete sample, as we would naturally be missing galaxies lower than the surface brightness completeness limit. At high redshift

this limit is quite high – 20 mag arcsec^{-2}, which appears to be the limit in which we can still detect intrinsically faint galaxies at $z > 3$. What remains to be known or determined is if there are indeed galaxies at these redshifts which have an intrinsic surface brightness which is lower than this value and therefore unobservable with our current deep imaging. We investigate this question later in the chapter.

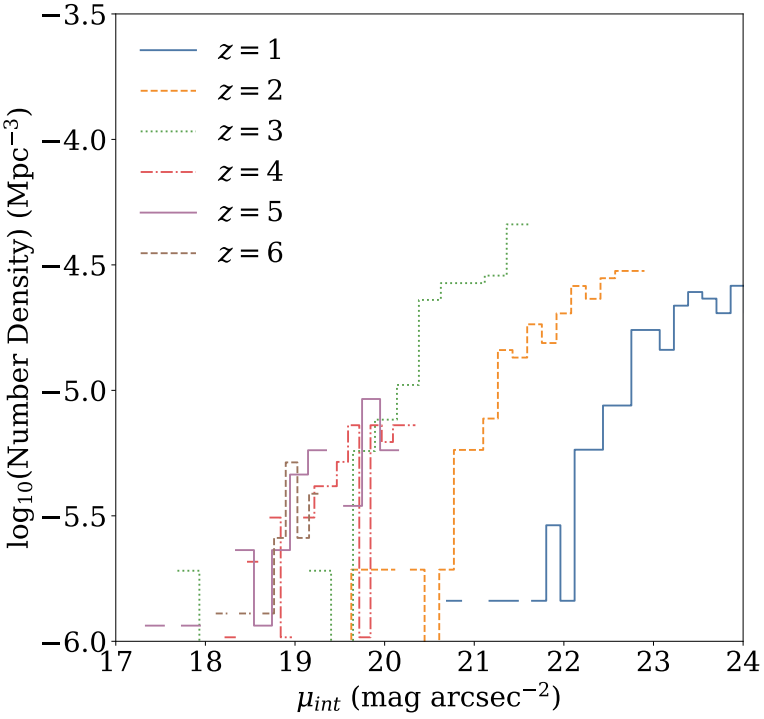

Figure 3.6: Intrinsic surface brightness distribution for each redshift. The different coloured lines show the different redshifts for this distribution of intrinsic surface brightness. These are corrected by a factor of $(1+z)^3$ from the observed distributions to account for the surface brightness dimming with redshift.

3.4.3 Artificially Redshifting Galaxies

We examine the effects of redshift using the simulations described in §3.3.5. We carry out these simulations by artificially redshifting galaxies at $z = 2$ and imaging them to how they would appear in our data at $z = 6$. This is done primarily using the techniques described in §3.3.5 whereby the galaxy is reduced in surface brightness by $(1 + z)^4$, and

then reimaged into our data.

When we carry out this process we find that there are few galaxies obviously visible in the resulting images. This implies that without some type of luminosity evolution we would only be able to detect a few galaxies with properties similar to the ones we can detect at $z = 2$ at higher redshifts. However, in addition to our visual determination of whether a galaxy has been detected, we measure the signal-to-noise ratio (S/N) of each of the objects after they are simulated. We measure the flux within $R_{\rm Petr}(\eta = 0.2)$. The average S/N for the redshifted sample is ~ 3, which is barely detectable at best, and which is a significant decrease when compared to the original sample of galaxies that have an average S/N of ~ 100. We find that 16% of the artificially redshifted galaxies are detectable (defined as having a S/N > 5) compared to 94% of the original sample of $z = 2$ galaxies.

We measure a difference of 3.5 ± 1.6 mag arcsec^{-2} in intrinsic surface brightness between $z = 6$ and $z = 2$ for the mass-selected sample and so we apply this difference to the $z = 6$ simulated galaxies in the form of an increase of brightness by a factor of ~ 24 using the relation:

$$\frac{L_{z=6}}{L_{z=2}} = 10^{0.4 \cdot \Delta M}. \tag{3.21}$$

As a result, the S/N of the artificially redshifted galaxies increases to about ~ 50 after this luminosity evolution is included. We also measure a mean observed surface brightness of 26.3 mag arcsec^{-2} and a mean intrinsic surface brightness of 19.9 mag arcsec^{-2}. Both results are ~ 0.3 magnitudes dimmer than the values we see for the actual $z = 6$ sample of galaxies. This implies that most of these galaxies would be observable at $z = 6$ just using the amount of decrease in the observed surface brightness and correcting for it.

However, we know from various studies of the luminosity function in the UV that

the intrinsic average brightness of galaxies on average changes as we go to higher redshifts, with galaxies becoming brighter (e.g., Arnouts et al., 2005; Bouwens et al., 2006; McLure et al., 2013; Duncan et al., 2014; Bouwens et al., 2015; Bhatawdekar et al., 2019). This observed brightening of the average galaxy population is however much less than the amount we observe in terms of the SB evolution.

To see the effect of this on the detectability of our sample of galaxies after being simulated from $z = 2$ to $z = 6$ we increase the brightness of our images by the observed amount from LF evolution. We take the $z = 2$ characteristic magnitude, M^*_{UV}, to be -20.33 ± 0.50 (Arnouts et al., 2005) and set this value to be the zero-point. We take the $z = 6$ characteristic magnitude to be -20.94 ± 0.20 (Bouwens et al., 2015) and calculate the change in magnitude between the two redshifts to be 0.61 ± 0.54 mag. We are then able to calculate the factor by which the brightness changes ($\frac{L_{z=6}}{L_{z=2}}$) from the lowest redshift to the highest redshift. We determine this value to be 1.75 ± 0.87, which is much less than the factor of 24 observed, as discussed above. We calculate this factor for each redshift interval and multiply the redshifted images by this factor to simulate the evolution of the luminosity function.

We show the evolution of both the observed and intrinsic surface brightness of the artificially redshifted sample of galaxies that have been evolved with the luminosity function in Figure 3.7. Unlike the actual observed surface brightness evolution, the measured SB for the simulated sample increases by 1.0 ± 1.9 mag arcsec^{-2} from $z = 6$ to $z = 2$, and we find that the evolution goes as $(1 + z)^{0.05\pm0.01}$ so therefore these simulated galaxies appear to get brighter with redshift. This is due to the method used when artificially redshifting the galaxies; the overall factor the images are multiplied by decreases as redshift increases leading to a smaller measured flux and therefore a dimmer surface brightness. The real mass-selected sample on the other hand decreases by 0.7 ± 1.6 mag arcsec^{-2} over the same redshift range. The intrinsic surface brightness

however follows the trend seen in the real sample but the evolution is not as steep; the evolution goes as $(1+z)^{-0.09\pm0.02}$ and the surface brightness decreases by 1.9 ± 1.9 mag arcsec^{-2} over the redshift range $z = 6$ to $z = 2$ whereas the real sample decreases by 3.5 ± 1.6 mag arcsec^{-2} over the same redshift range.

Based on this, there is approximately 1.6 magnitudes of intrinsic surface brightness evolution unaccounted for in the simulated images. We find from this that 84% of the $z = 2$ galaxies would not be detected at $z = 6$ if evolved with the luminosity function (where detected galaxies are determined as being those with a S/N > 5), with only the highest surface brightness ones being detectable. This implies that there is a either a significant amount of galaxies being missed in deep *HST* imaging which exist at high redshifts, or that some galaxies have evolved significantly more than others. This would imply an unusually shaped surface brightness function at high redshifts. We will further discuss this in the discussion section of this chapter.

We also alternate how much evolution we add to determine how much brighter the galaxies at $z = 2$ would need to be in order to be considered significant detections. We find that a factor of 6 is required for a mean S/N value of 10. This factor of 6 in brightness equates to a change in magnitude of ~ 2 which is much larger than the change of 0.61 in magnitude seen for the characteristic magnitudes between $z = 2$ and $z = 6$. Thus it cannot be the case that surface brightness evolution is determined simply by an evolving luminosity and size within the Petrosian radius.

The limiting magnitudes for an extended source for the J_{125} filter of GOODS-South and GOODS-North fields are 27.9 mag and 28.0 mag respectively. These values are 5 × the photometric error within a 0.2 arcsec^2 aperture (Grogin et al., 2011). This equates to limiting observed surface brightness to 26.2 mag arcsec^{-2} and 26.3 mag arcsec^{-2} within a 0.2 arcsec^2 area, respectively. However, this is not a proper limit due to various factors. We thus empirically determine the SB completeness limit for our data by examining at

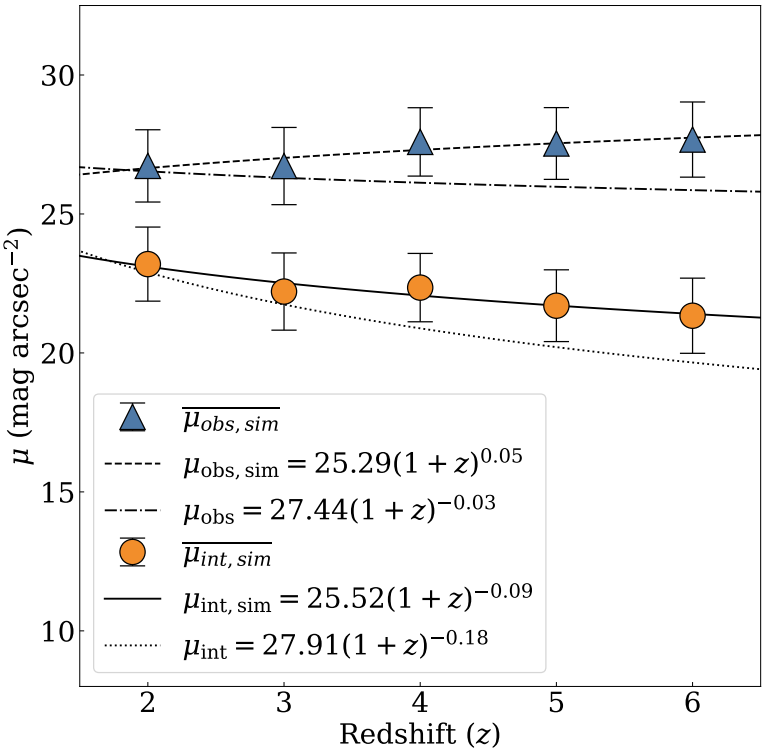

Figure 3.7: Evolution of the observed (blue triangles) and intrinsic (orange circles) surface brightness of our simulated galaxies that have been evolved with the luminosity function increase in brightness from $z = 2$ to $z = 6$. We fit a power law to both surface brightness and find $\mu_{\rm obs} = 25.29 \pm 0.30(1+z)^{0.05\pm0.01}$ (shown as a dashed line) for the observed surface brightness and find $\mu_{\rm int} = 25.52 \pm 0.67(1+z)^{-0.09\pm0.02}$ (shown as a solid line) for the intrinsic surface brightness. Also shown are the fits to the real surface brightness evolution for both the intrinsic (dotted line) and observed (dot-dash line).

which magnitude the SB function declines. We find that 90% of the simulated galaxies that have been evolved with the luminosity function correction have an observed surface brightness that is lower than the limiting surface brightness. Therefore, if these galaxies were real, we would not be able to detect the vast majority of these galaxies using the J_{125} filter of WFC3.

In the next section of this chapter we investigate the relationship of surface brightness to other galaxy properties. One reason we do this is to try to make sense of this evolution in observed surface brightness and what it might imply regarding the galaxy population at high redshift.

3.4.4 Correlation With Other Parameters

The first part of this chapter is about the use of surface brightness measures as a way to detect galaxies. We discuss how it is likely that many galaxies are likely missing and whether the evolution of luminosity is consistent with the intrinsic SB evolution. In this section, we explore the relationship between the intrinsic surface brightness and other galaxy parameters such as star formation rate. This is the second part of this chapter whereby we examine how the surface brightness reveals information about the physical state of the galaxies and how they are evolving.

Firstly, we determine the relationship between intrinsic surface brightness and the stellar mass of our mass-selected sample of galaxies for each redshift bin, as shown in Figure 3.8. Each panel shows the relationship for each redshift bin with the final panel giving the evolution of the slope of the relationship. The fits for each redshift are shown as dashed lines and the surface brightness completeness limit described in §3.3.4

is shown by a solid line. The fits are determined by minimising the errors in the surface brightness. There are galaxies below the surface brightness limits due to the way in which we determine the surface brightness limit; we find the point at which the surface brightness function declines and as this is gradual and not a vertical drop, there are some galaxies that have a low surface brightness. We find a slight dependence of surface brightness on galaxy stellar mass whereby lower surface brightness galaxies have a higher mass, however this is a very small dependence. In general, a galaxy of any given mass could have a range of surface brightness at all redshifts. This suggests that the stellar mass of a galaxy does not heavily influence the evolution of its intrinsic surface brightness. It also implies that by only reaching a certain surface brightness limit we are not solely missing low-mass galaxies, but high-mass galaxies are missing too. This has important consequences for understanding the fact that we are missing galaxies at

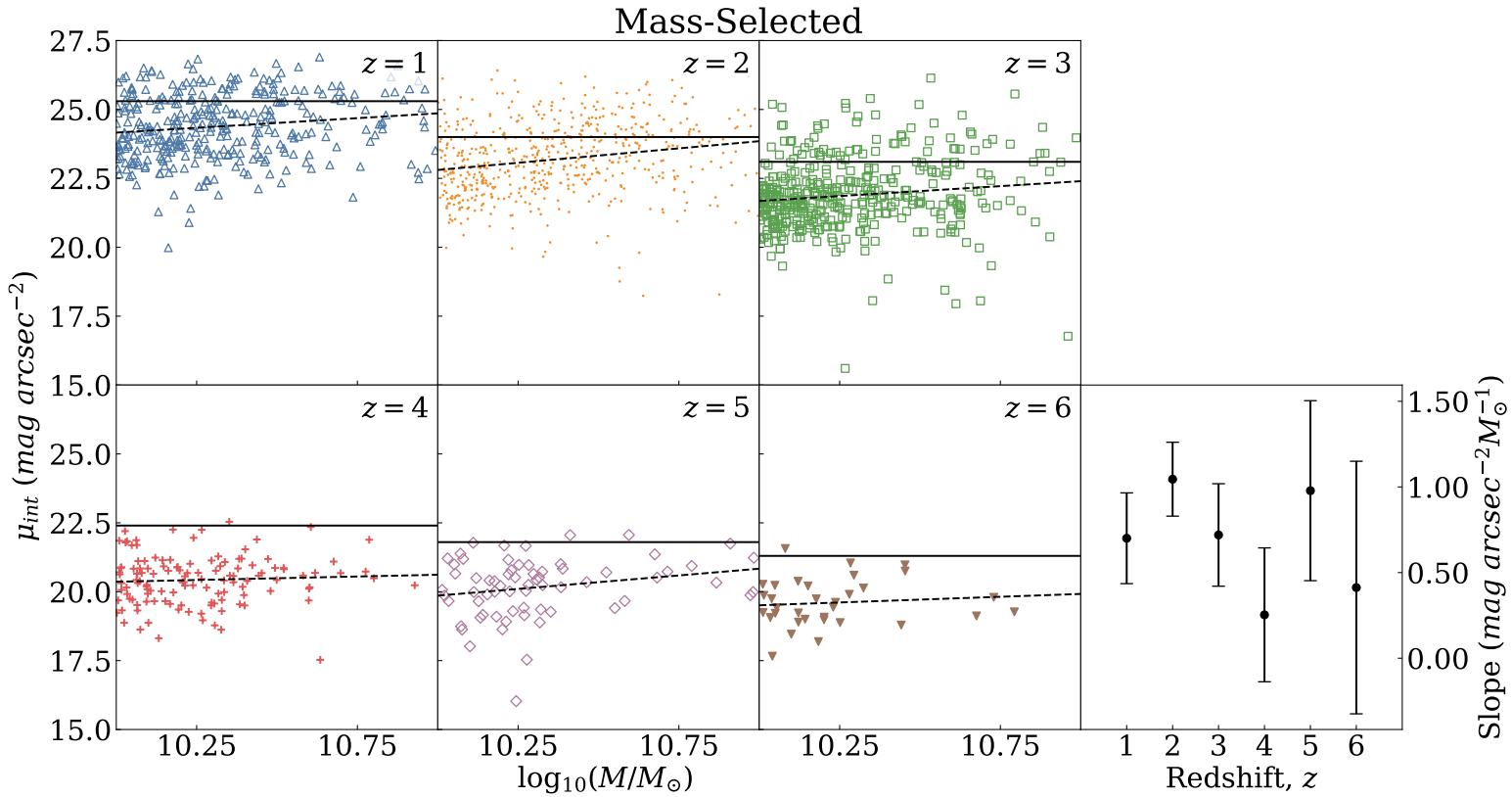

Figure 3.8: Relationship between the intrinsic surface brightness and galaxy stellar mass for each redshift bin. Each bin is shown in a separate panel and the final panel shows the slope of the fit for each bin. The fits are shown as dashed lines in each panel and the surface brightness completeness limit at each redshift is indicated by the solid vertical line. The linear fits are done by minimising the errors in the surface brightness. We find very little dependence of surface brightness on galaxy stellar mass at all redshifts, suggesting that a galaxy of any given mass could have a range of surface brightness values.

high redshift under the surface brightness completeness limits.

As we probe the universe with deeper observations, we are are able to detect galaxies with lower surface brightness. However, as we are only looking at objects in the UV rest-frame at the highest redshifts with *HST*, we can conclude that we are missing galaxies at all stellar masses. To highlight this, we compare the relationship between the stellar mass and intrinsic surface brightness measured in the UV rest-frame (B_{435}) and the H_{160} band, as shown in Figure 3.9. The slope for the H_{160} band is negative as opposed to no relation as seen for the B_{435} band. This is such that within the H_{160} band those galaxies with the highest masses exhibit a higher surface brightness. We do not witnesses this when observing galaxies in the rest-frame UV; in this case there is a large scatter and no obvious trend. From this we can conclude that it is thus likely that observations are missing low surface brightness galaxies in the UV which span all stellar masses.

We also examine the evolution star formation rate density, Σ_{SFR} of the two samples. Σ_{SFR} is defined as the star formation rate per unit area where the area used is the region bound by a circle of radius $R_{\rm Petr}(\eta = 0.2)$. In the left panel of Figure 3.10, we show the mean star formation rate density for the mass-selected sample as orange circles. In the right panel of Figure 3.10, we show the same relation but for the number density-selected sample. For both samples, we see decreases in $\log_{10}(\Sigma_{SFR})$ of $1.4 \pm 0.6 M_{\odot}{\rm yr}^{-1}{\rm kpc}^{-2}$ and $1.5 \pm 1.0 M_{\odot}{\rm yr}^{-1}{\rm kpc}^{-2}$ for the mass-selected and number density-selected samples respectively. Both results show that a higher surface brightness correlates with a larger SFR and a larger SFR per unit mass.

The relationship between the star formation rate (SFR) and the intrinsic surface brightness is shown in Figure 3.11 for the six redshift bins. On top we show the results for the mass-selected sample and the bottom shows the same results for the number density-selected sample. Each panel shows the relationship between the two variables

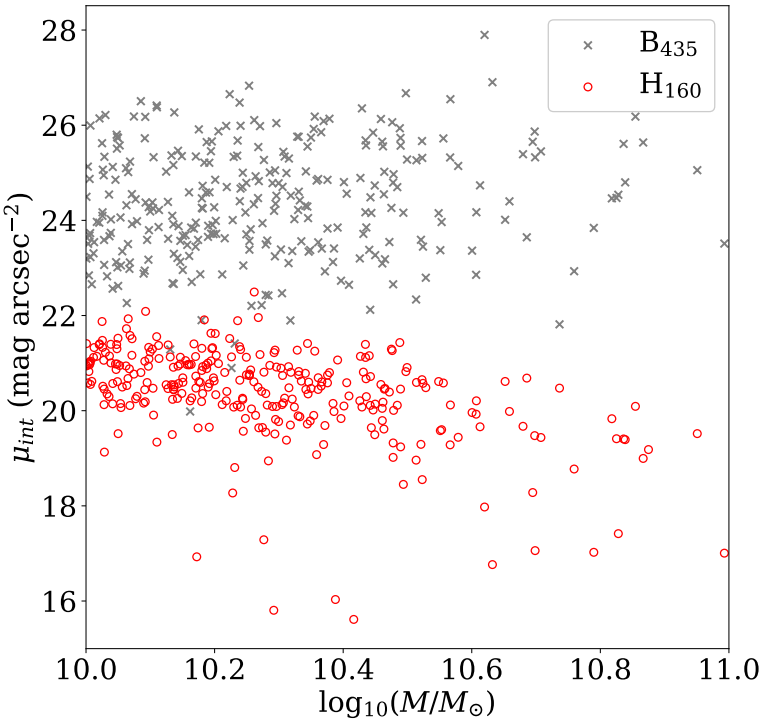

Figure 3.9: Intrinsic surface brightness versus stellar mass for $z = 1$ galaxies as observed with *HST*. The UV rest-frame (B_{435}) is shown as grey crosses and the same measurement for the H_{160} band is shown as red circles.

for each redshift bin, along with a fit to the data. The final panel shows the evolution of the slope of these fits with redshift. On average, the slope gets steeper with time for the mass-selected sample. The slope for the number density-selected sample however remains approximately constant with time.

We also show the relationship between the intrinsic surface brightness and specific star formation rate (sSFR, defined as the star formation rate per unit mass) for both samples in Figure 3.12. As for Figure 3.11, on the top panel we show the relationship for the mass-selected sample and on the bottom we show the relationship for the number density-selected sample. Each panel shows the relationship between SFR and intrinsic SB for each of the seven redshift bins and the bottom right panel shows the evolution of the slope with redshift. The slopes of both samples get steeper with time however the mass-selected sample changes by a greater amount.

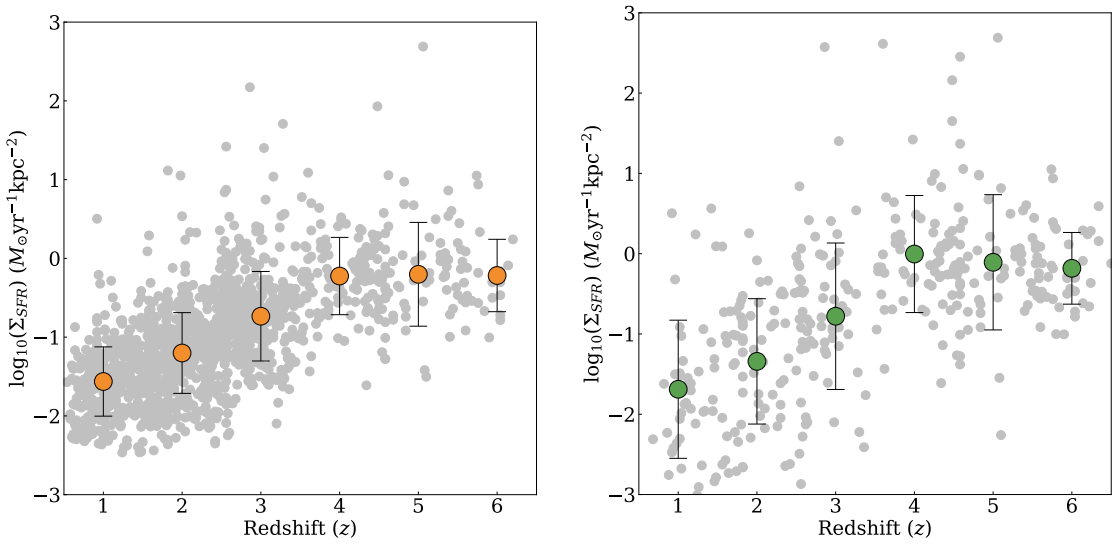

Figure 3.10: Left: evolution of the logarithm of the star formation rate density, Σ_{SFR} for the mass-selected sample. Individual points are shown as grey circles. The orange circles show the mean Σ_{SFR} for each redshift bin. The error bars on these points are given as 1σ from the mean. Right: evolution of the logarithm of the star formation rate density for the number density-selected sample. Green circles show the mean star formation rate density for each redshift. The error bars on these points are given as 1σ from the mean.

3.5 Discussion

In this section we discuss our results, including what the meaning of the surface brightness evolution implies for detection of missing galaxies at high redshift, as well as for what the correlation of SB With other parameters means for the origin of the changes in observed intrinsic surface brightness.

3.5.1 Surface Brightness Evolution

The observed surface brightness evolution for both the mass and number density samples decreases with time by 0.7 ± 1.5 mag arcsec^{-2} with evolution of the form $(1+z)^{-0.03\pm0.01}$ for the mass-selected sample and decreases by 1.2 ± 1.4 mag arcsec^{-2} with evolution

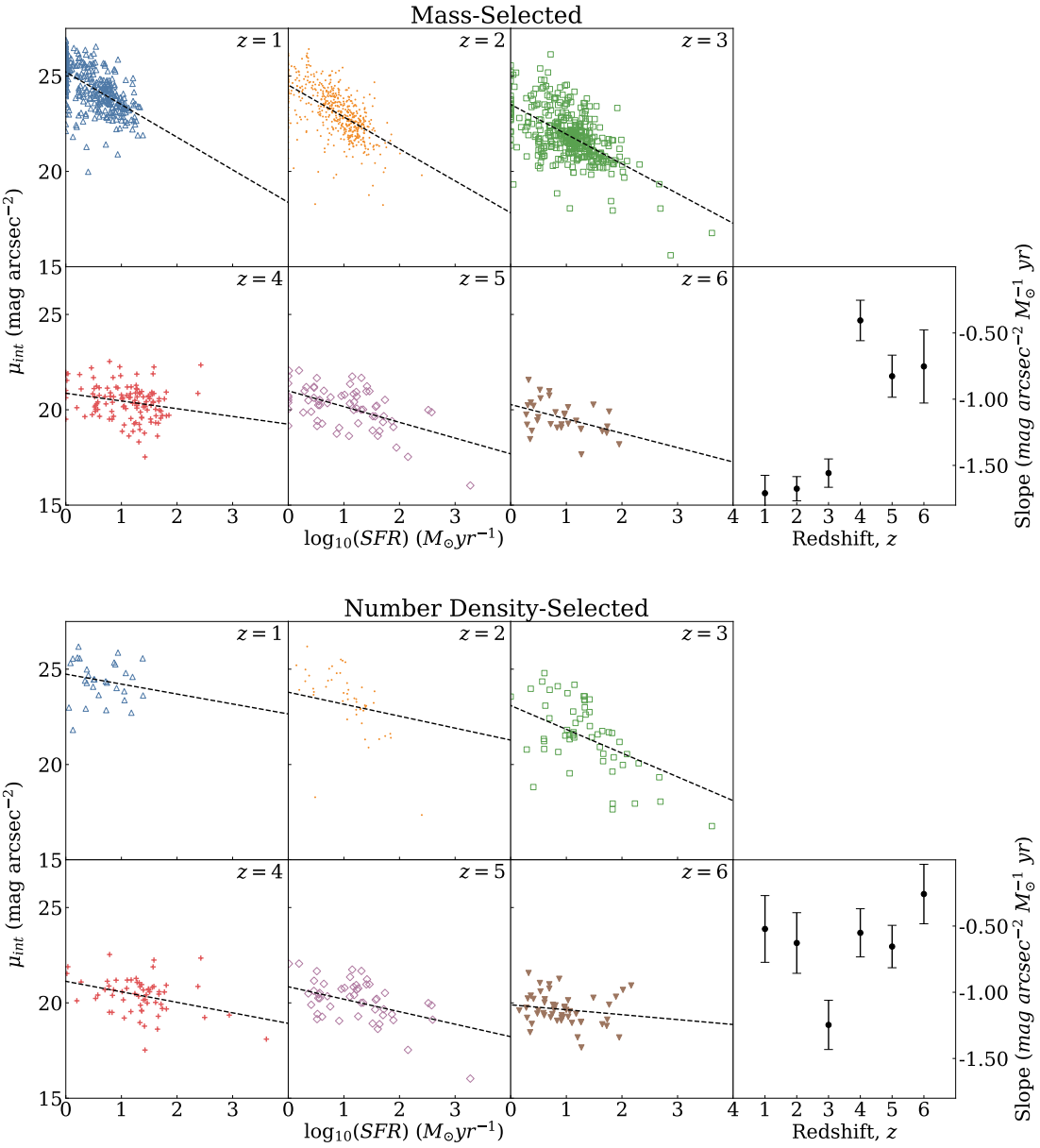

Figure 3.11: Top: star formation rate versus intrinsic surface brightness for the mass-selected sample. Bottom: star formation rate versus intrinsic surface brightness for the number density-selected sample. Each redshift bin is given as a separate panel and a straight line fit (dashed line) to the fits is given for each. The final panels give the evolution of the slope of these fits. The error bars on these points are the square root of the variance of the estimated slope. For the mass-selected sample, the slope of the fits for each redshift bin gets steeper with time, on average, suggesting the dependence of surface brightness on star formation rate gets stronger with time. For the number density-selected sample, the slope remains roughly constant with time suggesting that, for this sample, there is little dependence on the relationship between star formation rate and surface brightness with time.

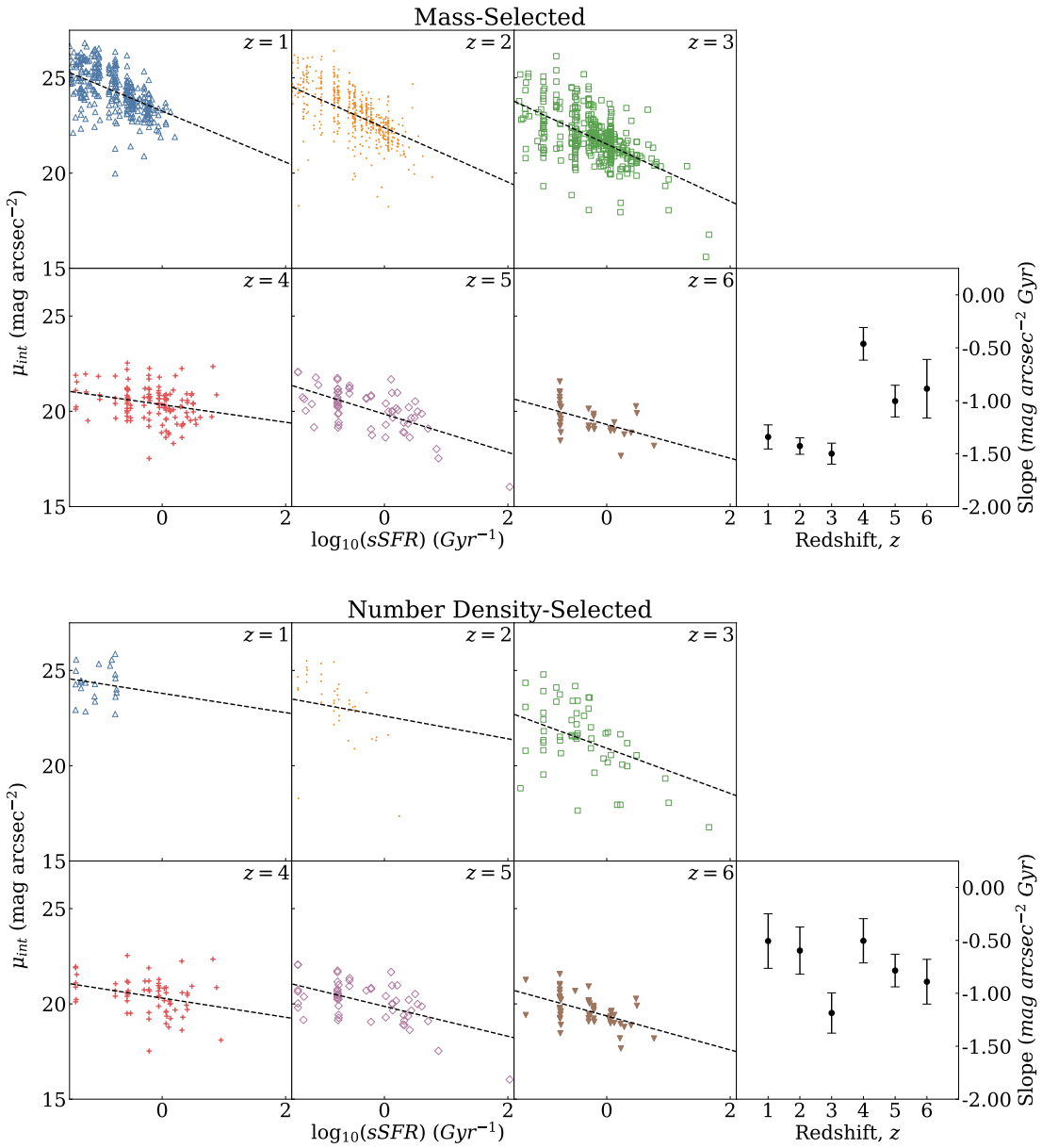

Figure 3.12: Top: specific star formation rate versus intrinsic surface brightness for the mass-selected sample. Bottom: specific star formation rate versus intrinsic surface brightness for the number density-selected sample. Each redshift bin is given as a separate panel and a straight line fit (dashed line) to the fits is given for each. The final panels give the evolution of the slope of these fits. The error bars on these points are the square root of the variance of the estimated slope.

of the form $(1+z)^{-0.04\pm0.01}$ for the number density-selected sample. This suggests that the observed surface brightness remains almost constant with a slight decrease at low redshifts, which is certainly due to the more sensitive optical filters on *HST*. It could also be due to a selection bias.

However, that is the observed surface brightness evolution, and what we really want to study and understand is the intrinsic evolution of surface brightness once it has been corrected for redshift effects, what we call the intrinsic surface brightness, $\mu_{\rm int}$. The change in the mean $\mu_{\rm int}$ from $z = 6$ to $z = 1$ for the mass-selected sample is 4.7 ± 1.5 mag arcsec^{-2}. The intrinsic surface brightness evolution of the number density-selected sample changes by 5.0 ± 1.4 mag arcsec^{-2} over the same range. This is a very large change in surface brightness over this redshift range, where $\mu_{\rm int}$ decreases by 0.5-0.7 mag arcsec^{-2} per redshift interval.

This is consistent with previous studies using both ground based and *HST* observations that find an evolution of 1-2 mag between $z = 0$ and $z = 1$ (e.g., Schade et al., 1996; Lilly et al., 1998; Labbé et al., 2003; Barden et al., 2005), but now extended to much higher redshifts. This change in intrinsic surface brightness is likely due to the fading of sources or an intrinsic luminosity difference. The question is - what is producing this change in intrinsic surface brightness evolution, and what does it imply for our detectability for distant galaxies? To answer this we consider the effects of size, dust, star formation, and detection limits to understand these issues.

3.5.1.1 Effects of UV Luminosity Evolution

As we are examining the evolution of the UV luminosity surface brightness, one area where we must first try to understand the evolution of the SB is within the UV luminosity itself. As explained in §3.4.3, we are able to trace the evolution of this UV luminosity

function, and more importantly, the value of M^*_{UV} and how it evolves with time. Although the total SFR decreases at $z > 2$ overall per unit volume, the UV flux of individual galaxies increases, as characterized by the UV luminosity function. Using this data we know that the $z = 2$ characteristic magnitude, $M^*_{UV} = -20.33 \pm 0.50$ (Arnouts et al., 2005) and at higher redshifts this becomes brighter to -20.94 ± 0.20 (Bouwens et al., 2015), as discussed in §3.3.5. Thus a representative amount of evolution is for galaxies to become fainter, on average, by about 0.61 magnitudes over this epoch. This is certainly much less than the 4 to 5 magnitudes of observed SB evolution. Therefore the intrinsic SB evolution cannot be accounted for solely or even primarily by an evolution in UV flux.

3.5.1.2 Size Corrections

The size evolution of galaxies is well documented (e.g., Trujillo et al., 2007; Buitrago et al., 2008; van Dokkum et al., 2008; Cassata et al., 2010; Whitney et al., 2019). Because galaxies evolve in size to become larger at lower redshifts, this will in principle act to decrease the surface brightness of galaxies. Thus we test to determine whether this observed size evolution is causing an 'artificial' evolution in the surface brightness. To determine this we correct both the observed and intrinsic surface brightness values by setting the size of all galaxies to that of the median size at $z = 6$ as measured in Whitney et al. (2019). In all cases (for both samples and for both measures), we find that the fit to the evolution becomes less steep, and the change in intrinsic SB decreases from $\Delta\mu_{1\rightarrow6} = 4.7 \pm 1.5$ mag arcsec^{-2} to $\Delta\mu_{1\rightarrow6} = 3.5 \pm 1.8$ mag arcsec^{-2} for the mass-selected sample and decreases from $\Delta\mu_{1\rightarrow6} = 5.0 \pm 1.4$ mag arcsec^{-2} to $\Delta\mu_{1\rightarrow6} = 3.9 \pm 1.9$ mag arcsec^{-2} for the number density-selected sample. Therefore, the value of mag arcsec^{-2} changes by $\sim$1 mag arcsec^{-2} for both samples. This suggests that whilst the size evolution is causing some of the evolution we see in the surface brightness, it is

not the primary cause. When we account for the size and luminosity evolution, this still leaves ~ 3.5 magnitudes of SB unaccounted for that must be due to other effects.

By correcting the surface brightness using Equation 3.20, we are effectively examining the absolute magnitude at a fixed size. Ultimately we find that there is a small difference between the size corrected and uncorrected surface brightness evolution, indicating that the effect of size evolution and surface brightness evolution on incompleteness is small.

3.5.2 Effects of Dust

Here we explore the possibility of dust extinction producing an apparent decrease in the surface brightness from $z = 6$ to $z = 1$. In this work we use the UV rest-frame and as such, the light is significantly affected by dust attenuation.

We calculate the estimated dust extinction using the relation between dust extinction and the UV-continuum slope β from Meurer et al. (1999):

$$A_{1600} = 4.43 + 1.99\beta \tag{3.22}$$

where A_{1600} is the dust extinction at the rest-frame wavelength $\lambda = 1600$ Å. In the case where this relation implies a negative extinction, A_{1600} is assumed to be 0. Typically, higher redshift objects are found to have bluer UV-continuum slopes than lower redshift objects, implying the presence of younger stellar populations and lower metallicities in higher redshift objects (Wilkins et al., 2013). A smaller value of β therefore suggests there is less dust extinction at high-z (Meurer et al., 1999; Lehnert & Bremer, 2003; Bouwens et al., 2009). This implies that as dust grows in importance with time it will have more of an effect on the measured UV luminosity, which will therefore also produce

a change in the SB of the galaxies. Very dusty galaxies, such as sub-mm galaxies, are rare and there would be a negligible amount in the CANDELS fields we are taking our observations from, and as such, these galaxies are not something we need to consider here.

To determine the effect of this we consider the measured extinction for $z \geq 3$ galaxies due to the fact the β is a measure of evolved populations and as such, the high values of β measured at low redshift are artificially inflated by the abundance of early-type galaxies. We find that for the mass-selected sample, there is an increase of 0.1 ± 3.4 mag between $z = 6$ and $z = 3$. When fitting the values of A_{1600} to a straight line, we calculate a best-fit slope of -0.15 ± 3.4, so on average, there is an increase in the extinction but it is not significant. The value of A_{1600} for the number density-selected sample increases by 2.6 ± 4.3 mag from $z = 6$ to $z = 3$. The dust extinction therefore plays a small role in the decrease in intrinsic surface brightness, with ∼0.1 mag being accounted for in the mass-selected sample and ∼2.6 mag being accounted for in the number density-selected sample when considering the redshift range $3 \leq z \leq 6$. After considering size and dust corrections, we are left with ∼3.4 mag arcsec^{-2} of SB evolution unaccounted for within the mass-selected sample and ∼1.3 mag arcsec^{-2} unaccounted for within the number-density selected sample. However, the errors on the evolution of dust extinction are large in comparison to the actual value so this may result in all the surface brightness evolution being accounted for.

3.5.3 UV Magnitude Evolution Modelled

We model the change in absolute magnitude for the redshift range $1 \leq z \leq 6$ for a number of different star formation histories using **SMpy**[1] (Duncan et al., 2014). The SED is convolved at each redshift with the filter corresponding to the UV rest-frame

[1]https://github.com/dunkenj/smpy

wavelength at that redshift. The filters are given in Table 3.1. We use the same simple stellar population models and initial mass function used when completing the stellar mass fitting as described in §2.2.1. We model the evolution of the rest-frame magnitude using a star formation history given by

$$SFR \propto e^{\frac{-t}{\tau}} \tag{3.23}$$

and vary the value of τ. The evolution of the magnitude using star formation histories with τ = -10 Gyr, -5 Gyr, 1 Gyr, 5 Gyr, and 10 Gyr are as shown in Figure 3.13 where τ = -10 Gyr is shown as a green dashed line, τ = -5 Gyr is shown as an orange dashed line, τ = 1 Gyr is shown as a red solid line, τ = 5 Gyr is shown as a black dotted line and τ = 10 Gyr is shown as a blue dashed line. We show the change in absolute magnitude since $z = 6$ for each value of τ, where we assume the star formation started at $z = 20$. The scenario where the star formation history occurs very quickly during the early universe (τ = 1 Gyr) shows that the galaxies get much dimmer with time. The the other scenarios where the star formation is more gradual and continues throughout the galaxy evolution ($\tau >$) show a much shallower change in absolute magnitude, but the galaxies still get dimmer as redshift decreases. The scenarios where we model a rising star formation history yield a change in magnitude similar to that of $\tau >$ in that it is a shallow increase but could be argued to be constant throughout time. For star forming galaxies we would expect these τ values to be somewhat larger, and only near $\tau \sim 1$ at $z < 3$ for the most massive systems that undergo most of their star formation early in the universe's history. The model we use assumes a dust extinction of $A_V = 0$ and a metallicity of $Z = Z_\odot$. We also assume these values are constant with redshift therefore this figure only illustrates the age effects on the magnitude evolution but in reality, the dust extinction increases with time, as explained in §3.5.2, and also scales with metallicity so the evolution may

be steeper than seen here.

If we assume a star formation history with τ = 1 Gyr, we see a change of 5.8 mag from z = 6 to z = 1 which would entirely account for the evolution seen in the surface brightness not already accounted for by size and dust. However, our systems are known to be star forming over a long period of time, and therefore the τ value would be larger. If we take the information from empirical measurements of the value of τ (e.g., Ownsworth et al., 2016) we find that $\tau \sim 2 - 5$ Gyr. If we assume that our galaxies have a similar τ which is the case for systems at these mass ranges at $z < 3$, then we would find that the star formation history would cause the SB to be roughly constant with time. This would only exacerbate the problem of understanding the decline of the SB for these galaxies at lower redshifts. We have nonetheless already accounted for the decline in the UV brightness from using the luminosity function changes from $z \sim 6$ to lower redshifts. Thus we can conclude from this section that the decline in surface brightness we observe in our selections is not due to an evolution in the star formation rate. If anything these estimates are the maximum change in the brightness as the star formation history is known to increase from z = 6 to z = 3 which would have the effect of only increasing further the brightness of our sample.

3.5.3.1 Image Simulations - How many galaxies are we missing?

By artificially redshifting a sample of galaxies, we are able to determine whether the same galaxies we see at low redshift are detectable at high redshift. As a fiducial experiment we simulate the galaxies in our z = 2 sample to z = 6 and determine how many of these we would detect, at what S/N, and at what measured surface brightness, as described in §3.4.3.

When we do this experiment we find that only ∼16% of these simulated z = 2

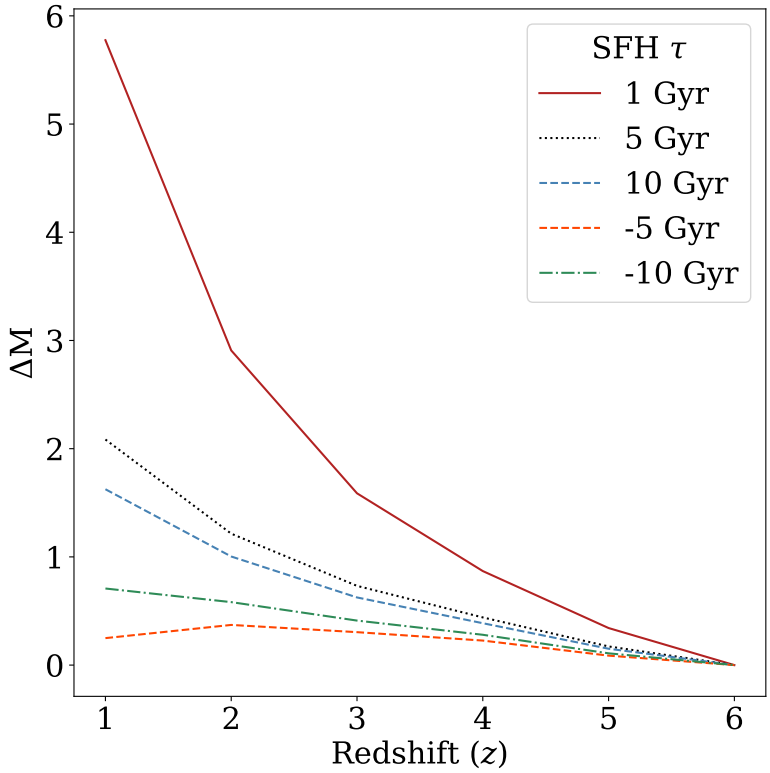

Figure 3.13: Evolution of the change in absolute magnitude since $z = 6$ for five different star formation histories. The SED is convolved at each redshift with the filter that corresponds to the UV rest-frame wavelength at that redshift. We use three decreasing star formation histories; τ = 1 Gyr is shown as a solid red line, τ = 5 Gyr is shown as a dotted black line and τ = 10 Gyr is shown as a dashed blue line. We also show two examples of increasing star formation histories; τ = -5 is shown as a dashed orange line and τ = -10 is shown as a green dashed line. There is a significant difference between $|\tau|$ = 1 Gyr and $|\tau| > 1$ Gyr whereby the UV rest-frame absolute magnitude decreases in brightness from $z = 6$ to $z = 1$ for τ = 1 Gyr but remains roughly constant for the other scenarios. The change in absolute magnitude is the change since $z = 6$ so is therefore 0 at this point.

galaxies are still detectable when simulated to be at $z = 6$ (at a S/N > 5), compared to 94% of the original galaxies at $z = 2$ with a S/N > 5, with the remaining 6% of detected galaxies at a S/N < 5 down to our magnitude limit. This suggests we are not detecting a significant number of galaxies at these high redshifts due to their observed low surface brightness produced by the effects of redshift.

The characteristic luminosity (L^*), as determined from the characteristic magnitudes

given by Arnouts et al. (2005) and Bouwens et al. (2015), decreases by a factor of 1.75 from $z = 6$ to $z = 2$. By calculating the equivalent change in luminosity of the redshifted sources using

$$\frac{L_{z=6}}{L_{z=2}} = 10^{0.4 \cdot \Delta M}, \tag{3.24}$$

we measure that the intrinsic luminosity of all galaxies artificially redshifted to $z = 6$ is 5.75 times brighter in SB than that of the original galaxies at $z = 2$. Therefore, the evolution we see in the artificially redshifted galaxies is greater than that of the characteristic luminosity. This strongly implies that the galaxies at $z = 2$ are not the descendants of the galaxies at $z = 6$ just by examining how much evolution they would have undergone.

When artificially redshifting the sample of $z = 2$ galaxies, we find that the change in surface brightness, both observed and intrinsic, does not correlate with the change we see in the real galaxies. For the observed surface brightness, we see a decrease in surface brightness of 1.0 ± 1.9 mag arcsec^{-2} when comparing the redshifted $z = 6$ galaxies (evolved with the luminosity function correction) to the original $z = 2$ galaxies, as shown in Figure 3.7. For the real sample, we see an increase in surface brightness of 0.7 ± 1.1 mag arcsec^{-2} over the same redshift range. For the intrinsic surface brightness, we see a change of 1.9 ± 1.5 mag arcsec^{-2} in the simulated sample whereas for the real sample, there is a change of 3.5 ± 1.6 mag arcsec^{-2} over the same redshift range.

We conclude from this analysis that there are a significant number of missing galaxies at high redshifts that are driving the intrinsic average surface brightness evolution. Because it is only the brightest galaxies we are detecting at $z \sim 6$ due to our SB limits, this drives up the intrinsic measurement of the average surface brightness. This is true even when examining a mass- or number density-selected sample. It is thus not simply

due to missing lower mass galaxies. In fact, as our simulations show we are missing 84% of the $z = 2$ galaxies when they are simulated to $z = 6$ even when we take into account the average increase in magnitude from the UV luminosity function. From this we conclude that there is a significant population of galaxies that remain undetected at these higher redshifts (e.g., Conselice et al., 2016). Most of these galaxies are likely to be span our entire mass range, and not just be low-mass systems. Therefore, our previously stated mass completeness limit underestimates selection effects.

The density of our detected galaxies (those with S/N > 5) at $z = 2$ is measured as 3.2×10^{-3}Mpc^{-3}. The density of our detected galaxies at $z = 6$ is almost a factor of 10 smaller at 2.5×10^{-4}Mpc^{-3}. The measured density of the simulated $z = 6$ galaxies (evolved with the luminosity function) is 4.1×10^{-3}Mpc^{-3}. This is 16 times greater than the real $z = 6$ galaxies. This suggests we are missing a significant number of high redshift galaxies in the real observations. The fact that there are undetected galaxies at high redshift is consistent with the actual number of galaxies being higher than the number we can actually see (Conselice et al., 2016). Many of these missing galaxies will be lower mass, but a significant fraction will be high mass systems.

3.5.4 The Origin of High SB Galaxies

In this section we discuss how to measure how the SB evolves intrinsically and what this implies for the evolution of galaxies in terms of their star formation rate and gas densities that produce this star formation. One issue is that it is clear that at the highest redshifts we are only observing galaxies with the very highest intrinsic SB levels. These are much higher in SB than galaxies in the nearby universe and the question is what is the origin of these systems and how do they relate to lower redshift galaxies?

3.5.4.1 Star Formation Rate Density

For both mass- and number density-selected samples, we find that on average, there is a decrease in the star formation rate density (Σ_{SFR}) over time. The gas density and fraction are observed to be greater at higher redshifts (Tacconi et al., 2013; González Delgado et al., 2017) which leads to a higher Σ_{SFR} by extrapolating from the Kennicutt-Schmidt law (Barden et al., 2005; Mosleh et al., 2012). Increased size at low redshift also contributes to the lower Σ_{SFR} we see at low redshift. However, from the change we see in the star formation rate over redshift (Figure 3.10), this size evolution is unlikely to be a significant cause of the decrease in Σ_{SFR} at lower redshifts.

We find a difference in Σ_{SFR} of $1.4 \pm 0.6\ \mathrm{M_\odot yr^{-1} kpc^{-2}}$ for the mass-selected sample and a difference of $1.5 \pm 1.0\ \mathrm{M_\odot yr^{-1} kpc^{-2}}$ for the number density-selected sample over the redshift range $1 < z < 6$. This suggests that the evolution in luminosity cannot be solely driven by the star formation rate density. This reinforces our conclusions from the previous argument that there are multiple factors contributing to the origin of the 4 to 5 mags of evolution in intrinsic SB observed.

3.5.4.2 Star Formation Rate and Specific Star Formation Rate

As we have shown, the surface brightness of a galaxy depends strongly on the star formation rate, particularly in the UV, as to be expected. In the case of the mass-selected sample, this relationship appears to grow stronger as time progresses with galaxies that have a high star formation rate generally exhibiting a brighter SB. In the case of the number density-selected sample the slope of the relation between these quantities remains approximately constant with time suggesting that there is little dependence on the relationship between star formation rate and intrinsic surface brightness with time.

The two samples differ in that one contains galaxies that are at the same mass and one

that contains galaxies of differing mass, depending on the number density requirement with the lower redshift bins containing galaxies of a higher mass than the higher redshift bins. From this, we can infer that the surface brightness of galaxies at high redshift of a given mass depends less on the star formation rate than galaxies of the same mass at lower redshifts. On the other hand, if we directly track galaxies through time, we infer that the relationship between star formation rate and surface brightness does not change as the galaxies evolve and grow in mass.

The evolution of the relationship between the specific star formation rate and intrinsic surface brightness is similar to that between the SFR and μ_{int} whereby the mass-selected sample shows a stronger dependence between the two at lower redshifts and for the number density-selected sample remains roughly constant with time.

3.6 Conclusions

We present an analysis of the surface brightness evolution of two separate samples (a mass-selected sample and a number density-selected sample) of galaxies taken from the GOODS-North and GOODS-South fields of the Cosmic Assembly Near-infrared Deep Extragalactic Legacy Survey. We examine UV rest-frame ($\lambda \sim 2000$ Å) images and find that strong evidence for surface brightness evolution whereby on average, galaxies get intrinsically brighter per unit area with redshift. This is the case for both the mass-selected and number-density samples. The evolution is consistent with the form given by $\propto (1+z)^{-0.18\pm0.01}$ and $\propto (1+z)^{-0.19\pm0.01}$ for each sample respectively. We explore possible causes of this evolution.

Size evolution is well known, and is now well quantified, so we test to determine whether this is producing the surface brightness evolution by setting the size of all galaxies to that of the average size of the galaxies at $z = 6$ (Whitney et al., 2019). We

find that SB the evolution is not significantly changed when accounting for this, thus the increase in the size of galaxies is not producing an 'artificial' surface brightness evolution. We also find that dust extinction is a possible cause of the evolution we see in μ_{int} but we find that it plays a small role, contributing 0.1 mag of evolution between $z = 6$ and $z = 3$ for the mass-selected sample and 2.6 mag for the number density-selected sample over the same redshift range.

We find that the star formation rate density (Σ_{SFR}) decreases with time, however the change does not completely explain the significant evolution we see in the intrinsic surface brightness. Thus a large portion of the intrinsic evolution for SB within galaxies is left unexplained. Thus, we are seeing an unnatural evolution in the amount of SB changes which thus must be due to an observational bias – we are missing high redshift galaxies in our observations, some of which are likely quite massive systems.

The stellar mass is known to be the cause of differences in galaxy evolution and is a measure of the formation and merging history of a galaxy (Bhatawdekar et al., 2019). We find that the intrinsic surface brightness of galaxies in the mass-selected sample does not rely heavily on the stellar mass; for each redshift bin, the slope of the relationship between the two quantities is very close to zero. This suggests that the stellar mass of a galaxy does not correlate with a galaxy's surface brightness. It also implies that the selection in the UV at these redshifts does not give mass completeness at any mass, even for the most massive, star forming galaxies.

To further demonstrate this we artificially redshift a sample of $z = 2$ galaxies to $z = 6$ to determine the level of surface brightness and what fraction of these we would still be detected at the higher redshift. We find that the surface brightness of these redshifted galaxies is much lower than that of the real $z = 6$ galaxies suggesting that we are not detecting the low SB galaxies we see at low redshift. This remains true when we consider the amount of evolution in the UV luminosity function when carrying out

these simulations.

In the case of the mass-selected sample, the star formation rate and specific star formation rate of galaxies depend strongly on the surface brightness at low redshift however this relationship gets weaker as redshift increases. We find that the relationship between these parameters is approximately constant for the number density-selected sample so whilst there is a dependence on SFR and μ_{int}, this dependence does not change with time.

Overall, we conclude that the high surface brightness galaxies we find at high redshift are not perfectly analogous to starburst galaxies seen at lower redshifts. It is also likely that there are many missing galaxies at these redshifts which will be discovered with telescopes that can probe deeper than *HST*, such as the forthcoming *James Webb Space Telescope* (*JWST*). Uncovering these galaxies will require that we obtain fundamentally much deeper imaging which will be carried out with first generation imaging with *JWST*. This may reveal a new population of distant high redshift galaxies that are not just lower mass, but including lower SB massive systems. These results may in fact alter our understanding of galaxy formation and the history of star formation and mass assembly in our universe's history.

Chapter 4

Galaxy Evolution in all Five CANDELS Fields and IllustrisTNG: Morphological, Structural, and the Major Merger Evolution to $z \sim 3$

4.1 Introduction

Throughout the history of galaxy studies, the most common way to derive galaxy evolution is through examining some property as a function of time. This includes the evolution of star formation, stellar mass, metallicity, and other properties. One of the most fundamental properties that is still being explored is the morphological or structural evolution of galaxies, which is an integrated result of the many different galaxy properties and formation processes (e.g., Conselice et al., 2008; Mortlock et al., 2013; Conselice, 2014; Huertas-Company et al., 2016b).

There are many ways in which to trace the structural evolution of galaxies. The most simplistic and direct way is investigating the size evolution (e.g., Trujillo et al., 2007; Buitrago et al., 2008; Allen et al., 2017; Whitney et al., 2019), and the surface brightness evolution (e.g., Whitney et al., 2020), as well as simply the evolution of apparent morphology classified into Hubble types/peculiars (e.g., Conselice et al., 2005). Another way to examine the evolution of galaxy structure is to examine the bulge and disk components of galaxies and how these evolve together (Bruce et al., 2014; Margalef-Bentabol et al., 2018). What has not been carried out in any detail is the quantitative evolution of galaxies as measured with non-parametric parameters. These parameters, including concentration and asymmetry (Kent, 1985; Conselice, 2003), reveal the processes of galaxy assembly through the systematic change of galaxy light over time.

Throughout a galaxy's lifetime, it will undergo several processes that will alter its structure and its morphology. Within a cosmological context of Λ-CDM, this includes the formation of bulges and then disks. In the simplest paradigm galaxies collapse into small systems that grow through star formation and mergers with other galaxies. At some point gas accretion will also occur and this is a primary method by which spiral arms and disks are formed. This process includes the accumulation of gas forming into stars that will expand galaxies in their outer parts (Whitney et al., 2019). This also includes mergers that will lead to structural peculiarities, and eventually, for some, into more concentrated systems. Furthermore, within clusters of galaxies processes such as ram pressure stripping (Gunn & Gott, 1972), starvation (Larson et al., 1980), and harassment (Moore et al., 1996) are all tied to galaxy star formation history and can strongly influence the physical and morphological properties of a galaxy.

A galaxy's morphology is traditionally defined as the point at which it lies on the 'tuning fork' diagram, first described by Edwin Hubble (Hubble, 1926), whereby

galaxies are defined as either spirals or ellipticals/S0s. Historically, these morphological classifications were done visually (e.g., de Vaucouleurs, 1959; Sandage, 1975; van den Bergh, 1976; Lintott et al., 2008, 2011), whereby an individual examines galaxy images and assigns labels to those images based in their visual appearance. However, this method gives rise to errors and biases and the sheer sample size of current and upcoming surveys mean this is quickly becoming inefficient even for large citizen-science projects such as Galaxy Zoo (Cheng et al., 2020). In order to remove some of these problems it is important to use a less subjective and more quantitative way of classifying galaxies. One such method is a non-parametric system that seeks to measure the concentration, asymmetry, clumpiness, Gini and M_{20} (CAS parameters) of galaxies by using measured light distribution. This system is described in papers such as Conselice et al. (2000b, 2002); Lotz et al. (2004). Using this method, galaxies can be placed in parameter space and from this, it can be seen that all major classes of galaxies in various phases of evolution are easily differentiated (Conselice, 2003). Furthermore, classical classifications of galaxies are unable to be used at higher redshifts, whereby most galaxies are not elliptical or spirals (e.g., Conselice et al., 2005; Mortlock et al., 2013).

An important stage of galaxy evolution that can be measured with these parameters is when a galaxy undergoes a merger. Mergers can be identified using methods such as pair fractions (Man et al., 2016; Mundy et al., 2017; Duncan et al., 2019; Ventou et al., 2019), Deep Learning models (Ferreira et al., 2020), and by using the CAS parameter space (Conselice, 2003; Lotz et al., 2004; Conselice et al., 2008; López-Sanjuan et al., 2009). Major mergers lie in a specific areas of these parameter spaces and as such, they are a useful tool in determining whether a galaxy is a merger or not. The merger rate can then be calculated from this to determine the role of mergers in forming galaxies.

In this chapter we investigate the general evolution of galaxy structure through

cosmic time. We start with visual estimates of morphology and structure and then we examine the quantitative structural evolution of these systems. We use IllustrisTNG simulations to help us interpret these structures from which we derive the rates of galaxy formation processes such as those driven by mergers and how light concentration in a galaxy changes with time.

Throughout this chapter we use AB magnitudes and assume a Λ-CDM cosmology with $H_0 = 70\ \mathrm{kms^{-1}Mpc^{-1}}$, $\Omega_m = 0.3$, and $\Omega_\Lambda = 0.7$.

4.2 Data & Methods

4.2.1 Data

We use a sample of 16,778 galaxies at redshifts in the range $0.5 < z < 3$ with stellar masses from $10^{9.5} M_\odot < M_* < 10^{12.2} M_\odot$ and only select galaxies with a signal-to-noise ratio > 10. This S/N ratio is determined from the flux of the image. This signal-to-noise cut removes only 340 galaxies from the initial sample. The mass and redshift distribution can be seen in Figure 4.1 where the yellow regions indicate a higher density of galaxies and purple indicates a lower density of galaxies. We select two samples from the 16,778 galaxies; a low mass sample with $10^{9.5} M_\odot < M_* < 10^{10.5} M_\odot$ and a high mass sample with $M_* > 10^{10.5} M_\odot$. We later also consider how our results change if we used a constant co-moving number density selected sample. The mass limits for our mass-selected sample are shown as horizontal dashed lines on Figure 4.1. Masses and redshifts are determined using the method described in Duncan et al. (2019). A brief description of the process used to obtain the measurements is given in §2.2.1.

This study makes use of data from the Cosmic Assembly Near-infrared Deep Extragalactic Survey (CANDELS; Grogin et al., 2011; Koekemoer et al., 2011). This survey

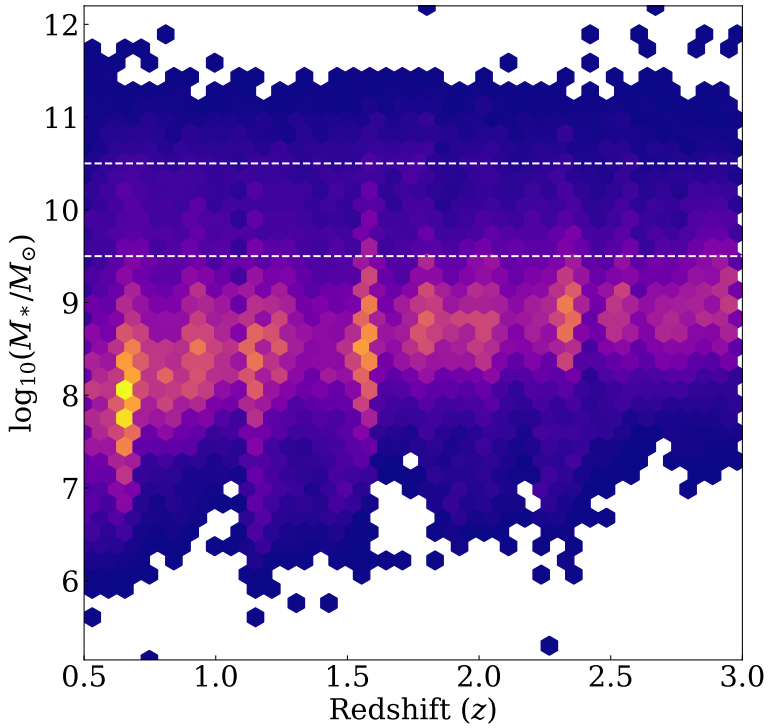

Figure 4.1: Mass and redshift distribution of the sample of galaxies. Yellow indicates a higher density of galaxies and purple indicates the lowest density. White areas indicate there are no galaxies present in this region of parameter space. The dashed horizontal lines at $\log_{10}(M_*/M_\odot) = 9.5$ and $\log_{10}(M_*/M_\odot) = 10.5$ indicate the boundaries between the two mass bins used in this study.

covers 800 arcmin^2 over five fields; GOODS-North, GOODS-South, COSMOS, UDS, and EGS. Our sample consists of galaxies from each of the five fields. CANDELS makes use of the Advanced Camera for Surveys (ACS) and the Wide Field Camera 3 (WFC3) on the *Hubble Space Telescope* (*HST*). For this work we use imaging data from the F814W, F125W, and F160W filters. These filters will be referred to as I_{814}, J_{125}, and H_{160} from this point onward.

We measure all parameters in the optical rest-frame at approximately $\lambda_{rest} \sim 4000$ Å. We do this by locating the observed filter where $\lambda_{rest} \sim 4000$ Å falls as determined by its redshift. We then use that filter in our further analysis to have a consistent rest-frame optical view of our galaxies. The idea here is to measure everything at a constant optical

rest-frame wavelength, to avoid structural biases produced by changes in rest-frame wavelength. The rest-frame wavelength and associated filter are given for each redshift bin in Table 4.1.

Table 4.1: The bands corresponding to the rest-frame optical at each redshift. Column 1 gives the midpoint of the redshift bin. Each redshift bin spans a redshift range of $\Delta z = 0.5$. Column 2 gives the band corresponding to the optical rest-frame and column 3 gives the rest-frame wavelength probed.

z	$O_{i,j}^{raw}$	λ_{rest}
0.75	I_{814}	4650 Å
1.25	I_{814}	3620 Å
1.75	J_{125}	4550 Å
2.25	J_{125}	3850 Å
2.75	H_{160}	4270 Å

We use visual morphological classifications from Kartaltepe et al. (2015) who base the majority of their classifications on H-band images, however J- and V-band images are also used for some features such as clumpy light. For a summary of how these classifications are done and in which morphological classes they are placed, see Kartaltepe et al. (2015).

4.2.2 MORFOMETRYKA

We measure the non-parametric concentration, asymmetry, and clumpiness parameters using the MORFOMETRYKA code (Ferrari et al., 2015). These measurements are made within the Petrosian region (e.g., Conselice et al., 2000b). This is defined as the area with the same axis ratio and position angle as the galaxy and with major axis equal to $N_{R_{\rm Petr}} R_{\rm Petr}$, where $N_{R_{\rm Petr}} = 1.5$ and $R_{\rm Petr}$ is the Petrosian radius. Below we give a description of each index we use, although for more details see Conselice (2003).

4.2.2.1 Asymmetry

The asymmetry, A, is calculated in the same way as in Conselice (2003) whereby a galaxy image rotated by 180° is subtracted from the original source image, and the absolute value of the total light in this self-subtracted image is divided by the total light in the original image. Asymmetry through various tests has been shown to be one of the most robust non-parametric structural parameters to measure and use in analyses. The formula for calculating the asymmetry index (A) we use is outlined in detail in Conselice (2003) and is given by:

$$A = \min\left(\frac{\Sigma|I_0 - I_{180}|}{\Sigma|I_0|}\right) - A_{bkg} \tag{4.1}$$

where I_0 represents the original galaxy image, and I_{180} is this image after rotating it by 180° from its centre. The asymmetry value is calculated through an iterative approach to find the centre of the rotation which is altered to find the one that gives the minimum asymmetry value. This minimum asymmetry is used as the final asymmetry value (e.g., Conselice et al., 2000b) with a search radius typically a pixel or half pixel. A_{bkg} is the background asymmetry of the image. This background term differs from the original application of the CAS parameter measurements whereby the background asymmetry is determined from a single region. MORFOMETRYKA initially did not include such a background correction. In this case we use the same method for determining A_{bkg} as in Tohill et al. (2021) whereby a 10×10 grid is overlayed on the image in an area outside of the galaxy segmentation map, the asymmetry of the individual cells are measured and then the median of these values is taken for A_{bkg}. This removes the bias present in the original method of measuring the asymmetry of a single background region and ensures the measurement is more robust.

4.2.2.2 Concentration

The concentration of a galaxy is used to distinguish between the different types of galaxies; for example, early type galaxies and their immediate progenitors tend to have a higher concentration than late type galaxies (e.g., Bershady et al., 2000; Conselice, 2003). Concentration, C, is defined as the ratio between two circular radii containing certain fractions of the total flux of the galaxy (Kent, 1985). We use R_{20}, the radius containing 20% of the total light, and R_{80}, the radius containing 80% of the total light. Therefore, the concentration is given as

$$C = 5 \times \log_{10}\left(\frac{R_{80}}{R_{20}}\right). \tag{4.2}$$

This calculation of the concentration is sensitive to seeing effects that are more prominent in the central regions and is therefore sensitive to the value of the inner radii R_{20} (Ferrari et al., 2015). We however, investigate other forms of concentration indices, and fully explore the idea of light concentration and what it actually implies for our galaxies. We also consider the R_{50} and R_{90} radii to avoid problems with the inner parts of galaxies, as well as examine the Petrosian radii measures of light concentration.

4.2.2.3 Clumpiness

The clumpiness, S, is a measure of the small scale structure within a galaxy. A higher clumpiness indicates that there are clumps of material within a galaxy, for example spiral galaxies contain many star forming regions and therefore contain many clumps of material. Elliptical galaxies on the other hand are generally smooth and therefore have a clumpiness that is close to zero. S is calculated in the same way as in Conselice (2003) whereby the image is first smoothed by a filter and then subtracted from the original

image. The flux contained within this residual is then divided by the flux contained with the original image. In this case, the filter used to smooth the original image is a Hamming window of size $R_{\rm Petr}/4$. Formally, the clumpiness can be described by the following

$$S = \sum_{i,j} \frac{|I(i,j) - I_S(i,j)|}{|I(i,j)|} - S_{bkg} \tag{4.3}$$

where $I(i,j)$ is the original image, $I_S(i,j)$ is the smoothed image, and S_{bkg} is the average smoothness of the background.

4.2.3 Correcting Values for Redshift Effects

Galaxy structure will change for a given galaxy when that same galaxy is viewed at higher redshifts. To decouple evolution from this effect, we need to account for this. In order to correct for redshift effects, we artificially redshift a sample of galaxies at $0.5 < z < 1$ in redshift intervals of $\Delta z = 0.5$ to a maximum redshift of $z = 2.75$. We take the galaxies in this initial bin from both GOODS fields and consider this our fiducial sample. We simulate these galaxies to higher redshifts and in the other CANDELS fields. We do this using the method described in Tohill et al. (2021). This method considers a number of effects. Firstly, it considers the rebinning factor b, which is the decrease in the apparent size of the galaxy when viewed at a higher redshift. This is done by following the method outlined in Conselice (2003) and de Albernaz Ferreira & Ferrari (2018). Luminosity evolution is also considered and this is implemented in the form found in Whitney et al. (2020) whereby the intrinsic surface brightness goes as

$$\mu_{\rm int} \propto (1+z)^{-0.18} \tag{4.4}$$

for a mass-selected sample of galaxies. After applying the rebinning factor, cosmological dimming of the form $(1+z)^{-4}$, as found by Tolman (1930), is applied. Finally, the image is convolved with the PSF corresponding to the rest-frame filter and inserted into an actual CANDELS background. For the first redshifting interval (z = 0.75 to z = 1.25) we do not convolve with the PSF as the filter corresponding to the optical rest-frame is the same for both redshifts. We then use MORFOMETRYKA to measure the CAS parameters at each redshift and compare these new values to the parameters measured at the original redshift. The differences are then applied to the real galaxies at the corresponding redshift. This change is dependent on the field due to the depth reached by each of the fields. The GOODS fields reach a greater depth than the COSMOS, EGS, and UDS fields and as such, we apply a different correction to each field. We also ensure that we are comparing the same galaxies at each redshift interval. To do this we only consider at all redshifts those galaxies that can be measured in the highest redshift as this ensures that we are comparing exactly the same galaxies at all redshifts to create a fair comparison and relevant correction factors.

The top left panel of Figure 4.2 shows the average asymmetry corrections applied to all CANDELS fields. The top right panel of Figure 4.2 shows the average concentration corrections applied to the five CANDELS fields. The bottom left panel shows the average clumpiness corrections applied to the CANDELS fields. For all parameters, the correction increases in magnitude for higher redshifts and the concentration corrections are relatively large with increased redshift. Table 4.2 gives the values of these corrections for each redshift bin within each field.

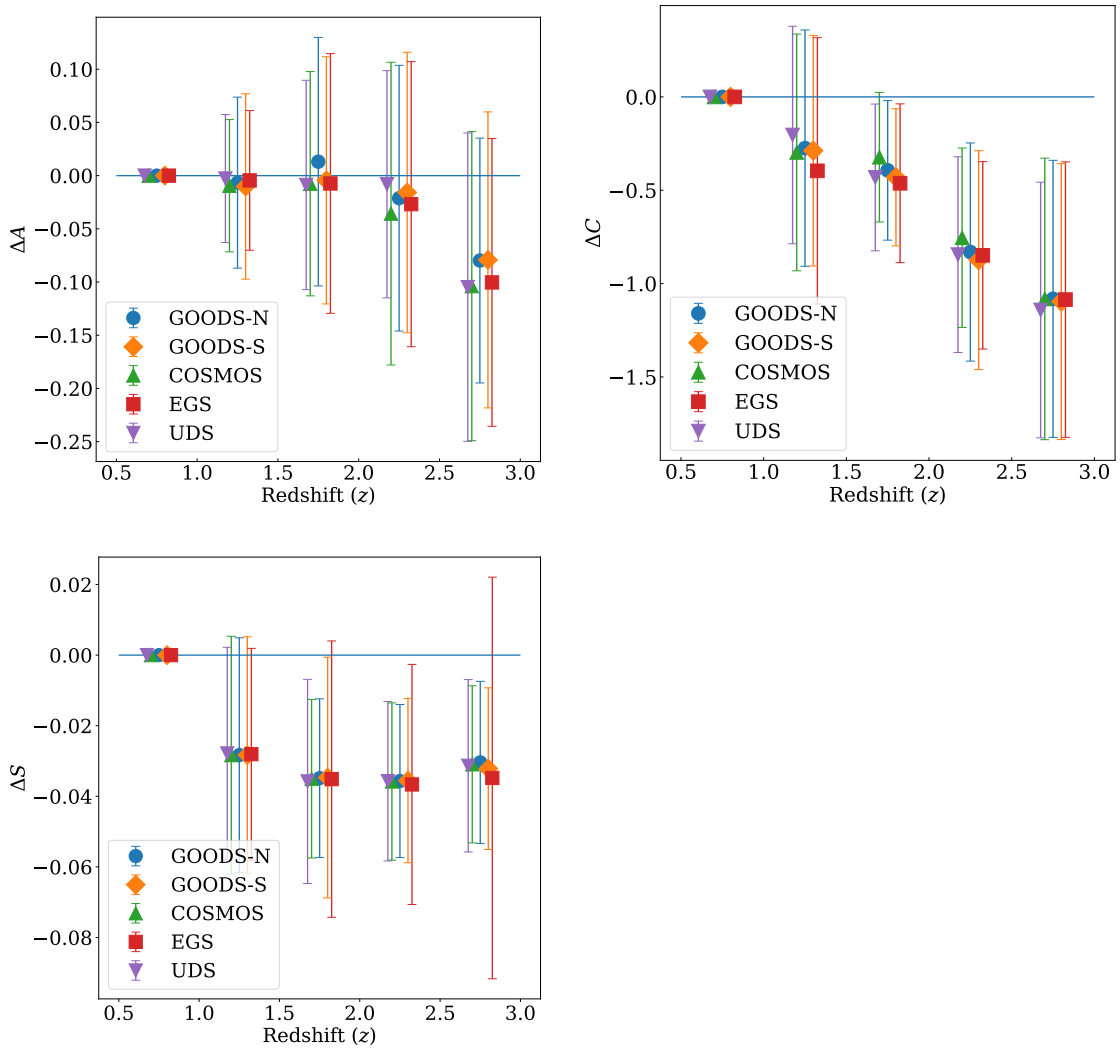

Figure 4.2: Top left: mean asymmetry correction applied to all five CANDELS fields. Top right: mean concentration correction for all CANDELS fields. Bottom left: mean clumpiness correction applied to the CANDELS fields. The error bars are equal to one standard deviation from the mean. In all panels, the GOODS-North correction is shown by a blue circle, GOODS-South by an orange diamond, COSMOS by a green triangle, EGS by a red square, and UDS by a purple inverted triangle.

4.2.4 Photometric Redshifts and Stellar Mass Fitting

To calculate the stellar masses and photometric redshifts of the glaxies within the sample, the same methods as in 2.2.1 are used.

Table 4.2: The asymmetry, concentration, and clumpiness corrections applied to each field at each redshift interval.

			Asymmetry		
z	GOODS-N	GOODS-S	COSMOS	EGS	UDS
0.75	0	0	0	0	0
1.25	-0.010	-0.010	-0.009	-0.004	-0.007
1.75	0.008	-0.004	-0.008	-0.007	-0.023
2.25	-0.032	-0.016	-0.036	-0.027	-0.060
2.75	-0.084	-0.079	-0.104	-0.100	-0.118
			Concentration		
0.75	0	0	0	0	0
1.25	-0.27	-0.29	-0.30	-0.40	-0.20
1.75	-0.39	-0.43	-0.32	-0.46	-0.43
2.25	-0.83	-0.87	-0.75	-0.85	-0.84
2.75	-1.08	-1.10	-1.08	-1.09	-1.14
			Clumpiness		
0.75	0	0	0	0	0
1.25	-0.028	-0.028	-0.028	-0.028	-0.028
1.75	-0.035	-0.035	-0.035	-0.035	-0.036
2.25	-0.036	-0.036	-0.036	-0.037	-0.036
2.75	-0.030	-0.032	-0.031	-0.035	-0.031

4.2.5 Illustris TNG300 Simulations

To interpret our results, we investigate how non-parametric morphologies change with redshift in a controlled manner with simulated galaxies. We do this as we want to disentangle real evolution effects from redshift effects. Additionally, by measuring these structural properties in simulated data we can estimate the observability timescales of galaxy mergers since it is possible to follow the time evolution of particular galaxies in this way (e.g., Lotz et al., 2008). With this goal in mind, we use data from the IllustrisTNG simulations (Pillepich et al., 2018; Springel et al., 2018; Nelson et al., 2018; Naiman et al., 2018; Marinacci et al., 2018; Nelson et al., 2019b; Nelson et al., 2019; Pillepich et al., 2019), which is a suite of cosmological, gravo-magnetohydrodynamical

simulation runs, ranging within a diverse set of particle resolutions for three comoving simulation boxes of size, 50, 100, 300 Mpc h^{-1}, named TNG50, TNG100 and TNG300, respectively.

Here we use data from both TNG50-1 and TNG300-1. For estimating the merging timescales we focus on the largest simulation box TNG300-1, as it provides us with a more mass complete sample at higher redshifts. However, when doing direct comparisons between the morphology measured in CANDELS and in the simulations we use data from TNG50-1 as its mass and spatial resolution produce more realistic morphologies. This enables us to generate images of simulated galaxies that are embedded in a cosmological context.

To measure the observability timescales of pair galaxy mergers discussed in §4.3.4.3, we select galaxies using the TNG300-1 merger trees by searching and locating galaxies in the simulation that have had only one major merger event within redshifts $z = 2$ to $z \sim 0$. This is to avoid contamination in the structure from past merger events. To balance any potential issues with the mass resolution of TNG300-1, we limit our analysis only to massive galaxies with $M_* > 10^{10} M_\odot$, which are in general represented by thousands of stellar particles. For these galaxies, we select all the snapshots and subhalos that are ± 2 Gyr of the snapshot from where the merger event takes place. We then narrow down our selection to 300 distinct galaxies, each with 35 different snapshots, resulting in a total of $\sim 10,000$ distinct objects. This ensures that we extensively probe not only around the merging event, but also the stages where the galaxies does not show signs of merging.

For a comparison between the non-parametric morphology and merger classifications of CANDELS galaxies and simulated galaxies we use the small box, high mass resolution TNG50-1 simulation, which is capable of producing output images in higher resolutions due to the high mass resolution and smaller gravitational softening length.

Here we do two different selections on TNG50-1 galaxies, which are described in §4.3.5.

The IllustrisTNG data contains the information from the stellar, gas, and dark matter particles for each source. However, to create mock broadband images from this information we post-process each stellar particle with a population synthesis process, as each particle represents a large region that can be described by a rich stellar population based on its age, mass, and metallicity. Instead of using the approach outlined in Ferreira et al. (2020), we follow the recipes from Trayford et al. (2017) and Vogelsberger et al. (2020) to post-process the simulation data with the Monte Carlo dusty radiative transfer code SKIRT (Camps & Baes, 2015, 2020). We also include the resampling of the star-forming regions outlined in Camps et al. (2016) and Trayford et al. (2017), as this is particularly important to avoid problems with the coarse representation of star forming regions. For each source simulated with SKIRT we produce observations in four different orientations in the 3D volume containing the galaxy cutout. Three of those are aligned with the simulation box axis: xy, xz and yz. We also include a fourth orientation covering an octant of the 3D volume. This post-processing step is independent of the simulation run used, the only difference being the number of stellar and gas particles available and the output size of the datacube.

The output from SKIRT is a datacube with a spectral energy distribution (SED) for each pixel, which is then convolved with the filter response function for the *HST* CANDELS filters used in this work, namely I_{814}, J_{125}, and H_{160}. The resulting broadband images are stored in two ways: without any observation effects and with *HST*-matched properties, including PSF, noise level, and sky background. The final images are then processed with MORFOMETRYKA to measure their CAS values. We later use these simulation outputs as a method for understanding our observational results.

4.3 Results

In the following subsections we discuss the results of our study in terms of the morphological and structural evolution of galaxies to $z = 3$. We first describe the visual morphological classification evolution of our sample of galaxies, while later we discuss the quantitative evolution using the CAS parameters. Finally we use these results to derive the merger fraction and merger rate evolution for our sample and the resulting number of mergers and mass accretion from mergers over this cosmic time.

4.3.1 Visual Classifications

Using the visual classifications for the CANDELS survey from Kartaltepe et al. (2015), we examine the fraction of each galaxy type within our sample. We consider those galaxies that are classified as the following: spheroid, disk, peculiar, and other. A galaxy is considered to have a classification if the fraction of classifiers within Kartaltepe et al. (2015) that deem it to be that particular type of object is greater than 0.6, and the fraction of all other classifications is less than 0.6. For peculiar galaxies, we consider any galaxy where the fraction of classifiers that consider that galaxy to be irregular in shape is greater than 0.6; no other conditions are required for this group. The other group consists of galaxies for which no consensus could be reached as to its morphological type, galaxies that were deemed unclassifiable, or galaxies that had no classification given. Figure 4.3 shows the evolution of the fraction of galaxies in each of these groups within our sample across the redshift range $0.5 < z < 2.5$. The spheroid galaxies are shown as red circles, disk galaxies as blue crosses, and peculiar galaxies as green triangles. The unclassifiable objects are shown as grey inverted triangles. We also fit power laws of the form $\alpha(1 + z)^{\beta}$ to the spheroid (solid line), disk (dashed line), and peculiar (dotted line) categories. We find that the fractions evolve as:

$$f_{\rm sp} = (0.73 \pm 0.09)(1+z)^{-0.95\pm0.16} \tag{4.5}$$

for the spheroid galaxies,

$$f_{\rm di} = (0.48 \pm 0.05)(1+z)^{-0.60\pm0.13} \tag{4.6}$$

for the disk galaxies, and

$$f_{\rm pe} = (0.11 \pm 0.01)(1+z)^{1.04\pm0.10} \tag{4.7}$$

for the peculiar galaxies. The fraction of both disk and spheroid galaxies increase with cosmic time, whereas the fraction of peculiar galaxies decreases as redshift decreases. Note that these fits are only valid down to $z \sim 0.5$ and it is at this redshift where the fractions sum to one. It is clear that extrapolating these to $z \sim 0$ would over-predict the number for each type. The fraction of 'other' galaxies evolves from ∼20% at $z \sim 2.25$ and decreases to ∼6% at $z \sim 0.75$ due to the fact that galaxy features will be more distinguishable at lower redshifts due to increased resolution and fewer effects such as surface brightness dimming. This increase in unknown classifications at high redshifts suggests the fractions of spheroid, disk, and peculiar galaxies are underestimated. The evolution seen here is broadly consistent with Mortlock et al. (2013), whereby the fractions of both disk- and spheroid-like galaxies increase with cosmic time whereas peculiar galaxies are more common at higher redshifts than lower redshifts.

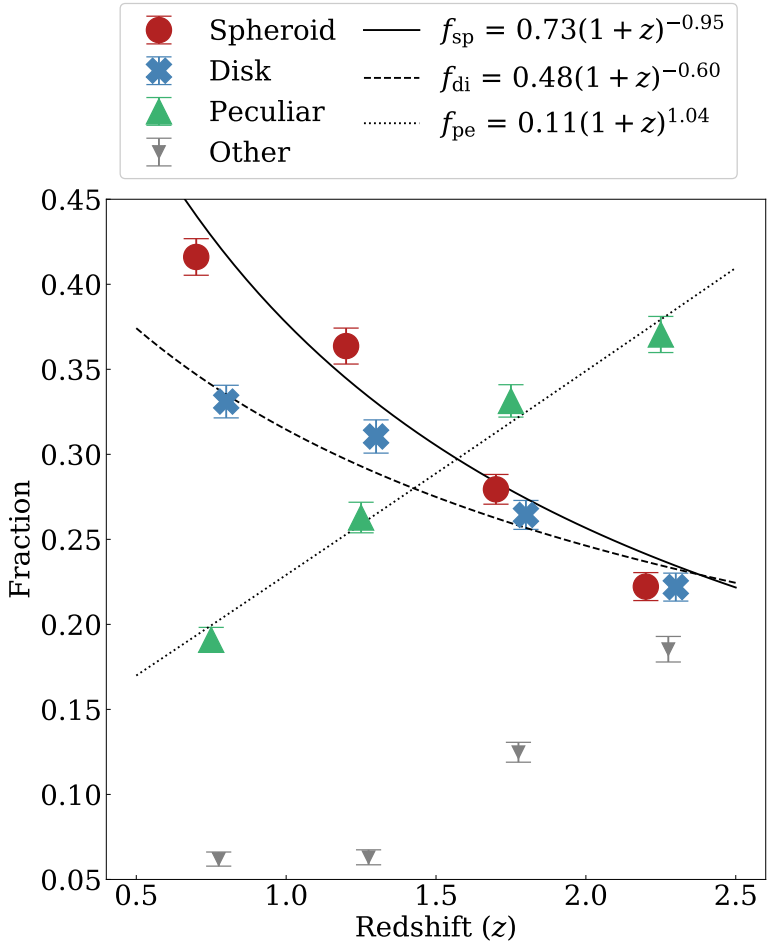

Figure 4.3: Evolution of the fractions of galaxies in our sample within a given visual morphological classification. Spheroid galaxies are shown as red red circles, disk galaxies as blue crosses, peculiar galaxies as green triangles, and unclassifiable objects as grey inverted triangles. Also shown are the power law fits to the spheroid (solid line), disk (dashed line), and peculiar categories (dotted line). For the error bars on these fitted parameters see the text.

4.3.2 Asymmetry and Concentration

We next explore the data by comparing the measured asymmetry and concentration values with the visual classifications from Kartaltepe et al. (2015) as described in the previous section. In this section we examine those galaxies that are identified as disk, spheroid, or peculiar galaxies. We first examine the uncorrected CAS parameters here, and later investigate a way to correct these parameters for redshift effects. Essentially,

the uncorrected values are comparable to each other at a given redshift (internally consistent), whereas the corrected values are comparable across all redshifts (externally and internally consistent).

In Figure 4.4, we show the evolution of the uncorrected concentration versus asymmetry for the galaxies within the sample that have one of our three main classifications. Red circles indicate a spheroid galaxy, blue crosses a disk galaxy, and green triangles a peculiar galaxy. Galaxies that fit none of these categories are shown as small grey circles. Also shown are the cuts between galaxy types taken from Bershady et al. (2000); the solid black line is the boundary between intermediate- and late-type galaxies whereby the galaxies that lay above this line are considered to be late-type galaxies, the dot dashed line is the boundary between early- and intermediate-type galaxies whereby galaxies below this line are considered to be early-type galaxies, and the dashed line is the boundary between mergers and non-mergers whereby galaxies that lie above this line are mergers.

At all redshifts, galaxies classified as spheroids tend to have a higher concentration and lower asymmetry, than the other classifications. Whereas peculiar galaxies have a higher asymmetry but lower concentration. This is consistent with the results found by Conselice (2003) for nearby galaxies. The range of concentration values increases with time but the overall distribution of these values for the spheroid and disk galaxies remains roughly constant with redshift. The asymmetry of the peculiar galaxies is centred on the $A > 0.35$ merger condition, however, the mean concentration changes from $\langle C \rangle = 3.52$ at $2.5 < z < 3.0$ to $\langle C \rangle = 2.49$ at $0.5 < z < 1.0$. The mean values for spheroid galaxies are $\langle C \rangle = 2.67$ and $\langle A \rangle = 0.16$ at the highest redshift. These values change to $\langle C \rangle = 3.10$ and $\langle A \rangle = 0.12$ at the lowest redshift. Galaxies classified as being disks have average concentration and asymmetry values of $\langle C \rangle = 2.52$ and $\langle A \rangle = 0.20$ at $2.5 < z < 3.0$ and these values do not change significantly within the lowest redshift bin

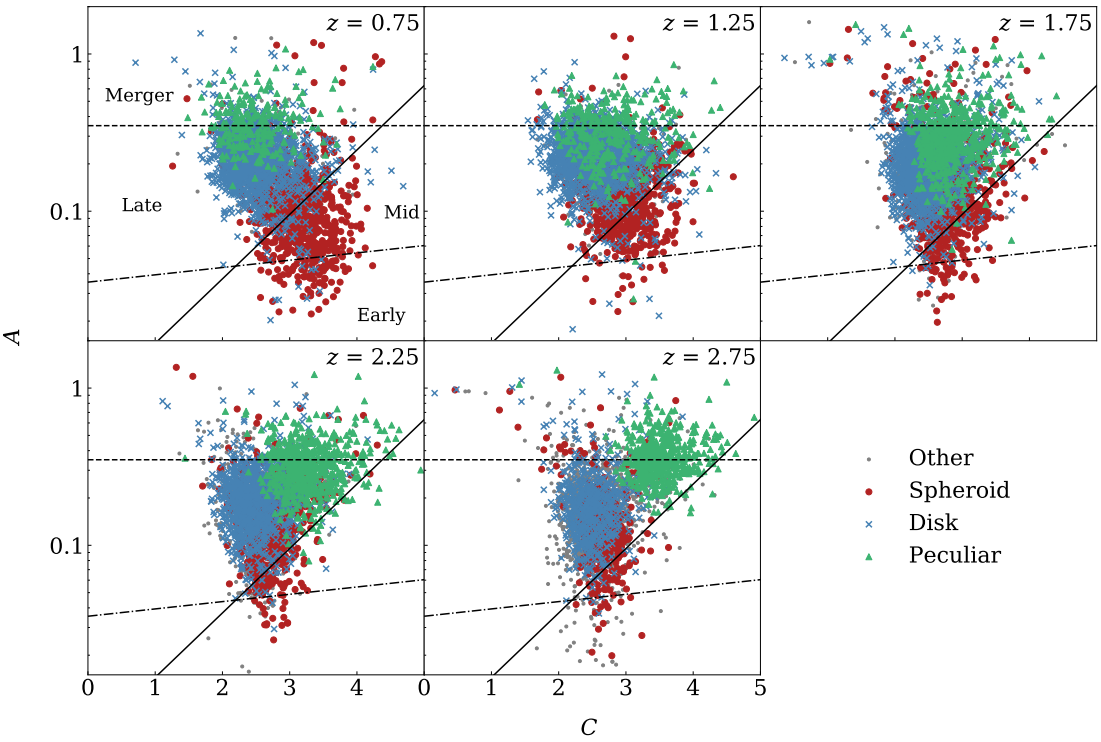

Figure 4.4: Evolution of the concentration-asymmetry plane with redshift, colour-coded by visual classification. Red circles are galaxies classified as spheroids, blue crosses as disks, and green triangles as peculiar galaxies. Any galaxies that do not fit within these three classifications are shown as small grey circles. The lines are boundaries between galaxy types derived from Bershady et al. (2000). Galaxies that are above the dashed line are considered to be mergers. The dot-dashed line is the boundary between early- and intermediate-type galaxies and the solid line is the boundary between late- and intermediate-type galaxies. The redshift indicated in the top right corner of each panel is the midpoint of the redshift bin whereby the upper and lower limits are 0.25 either side of this point.

of $0.5 < z < 1.0$ where $\langle C \rangle = 2.50$ and $\langle A \rangle = 0.23$. Thus the disks change their value the least and the spheroids the most. These results also show that galaxy classification is consistent and can be carried out to $z \sim 3$.

4.3.2.1 Disk/Bulge-dominated Galaxies

Within the catalog of Kartaltepe et al. (2015) every image has flags based on a number of interesting structural features present. Two of these flags indicated whether the galaxy

appears to be bulge- or disk-dominated. As with the visual morphological classifications, we assume a galaxy is bulge- or disk-dominated if the fraction of classifications that designate it to be such is greater than 0.6, and the other classification is less than 0.6. We show the evolution with redshift of the concentration-asymmetry plane for those galaxies classified as being bulge- or disk-dominated in Figure 4.5. Disk-dominated galaxies are shown as blue points and bulge-dominated galaxies are shown as red points. As with Figure 4.4, we also plot the boundaries between galaxy types. At higher redshifts there are fewer galaxies with either of the classifications in consideration here, likely due to greater noise and surface brightness dimming causing there to be less consensus among those classifying the images. This highlights the issues in classifying galaxy images and the need for a less subjective method of classifying galaxies.

Galaxies classified visually as disk-dominated predominantly lie in the late region of the concentration-asymmetry plane and the average values in the $0.5 < z < 1.0$ bin are $\langle A \rangle = 0.22$ and $\langle C \rangle = 2.68$. These values remain roughly constant across redshift and become $\langle A \rangle = 0.20$ and $\langle C \rangle = 2.69$ at $2.5 < z < 3.0$. At high redshifts, the bulge-dominated galaxies appear to lie in the late region but as redshift decreases, there are more galaxies in the intermediate and early regions of the plane. The average values of asymmetry and concentration of these bulge-dominated galaxies are $\langle A \rangle = 0.13$ and $\langle C \rangle = 3.14$ at $0.5 < z < 1.0$. The asymmetry value remains roughly constant to higher redshifts and becomes $\langle A \rangle = 0.14$ at $2.5 < z < 3.0$ but the concentration decreases with redshift and becomes $\langle C \rangle = 2.80$ at this redshift.

4.3.2.2 Clumpiness/Patchiness Matrix

Along with visual classifications of galaxies, classifiers involved in the work of Kartaltepe et al. (2015) also assigned flags based on how clumpy or patchy the distribution of the light within the galaxies is. Clumps are defined to be concentrated knots of light

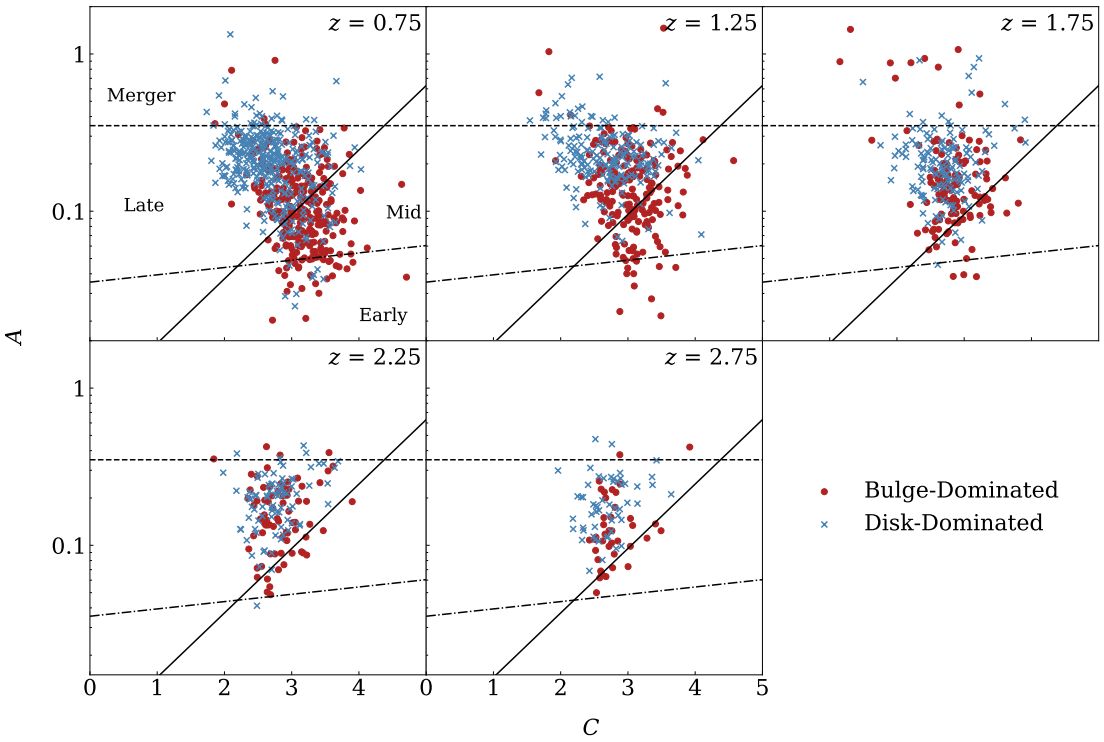

Figure 4.5: Evolution of the concentration-asymmetry plane with redshift for galaxies that have been given either a bulge-dominated flag (red circles) or a disk-dominated flag (blue crosses). Galaxies that have neither flag are not plotted. As with Figure 4.4, the lines are boundaries between galaxy types derived from Bershady et al. (2000). The redshift indicated in the top right corner of each panel is the midpoint of the redshift bin whereby the upper and lower limits are 0.25 either side of this point.

and patches are defined to be more diffuse structures of light. There are nine flags associated with this method of identifying features, with each flag denoting a different combination of the clumpiness (C) and patchiness (P). For example, a galaxy that exhibits no clumpiness and no patchiness will be labelled as 0C0P. A galaxy that appears to be extremely clumpy and patchy will be labelled as 2C2P. The levels of clumpiness and patchiness range between 0 and 2. As such we are able to organise the flags into a 3×3 grid with each square of the grid denoting the level of clumpiness or patchiness. Note, this clumpiness is not the same as the clumpiness, S, described in §4.2.2.3 and is a purely visual descriptor. A score of 0 indicates no clumpiness or patchiness and a score of 2 indicates a large amount of clumpiness or patchiness. In Figure 4.6, we show this

matrix of values and in each square of the grid, give the average concentration (top left, green), asymmetry (top right, red), and clumpiness (bottom left, blue). These average values are across all redshifts so any evolution in these parameters is not considered here. The lighter shades of colour denote a lower value of the CAS parameters while a darker shade denotes a higher value. In terms of concentration, the less clumpy or patchy a galaxy is, the higher its concentration on average. The opposite is true for the asymmetry and clumpiness; the more clumpy/patchy an image is, the higher the measured asymmetry and clumpiness.

4.3.3 CAS Parameter Evolution

We now investigate with our data the evolution of the CAS parameters. We ultimately use image simulations to determine how these parameters change with the effects of resolution and noise removed. Ultimately the evolution of these parameters will lead to a physical understanding of the driving forces behind galaxy formation over the epoch $0.5 < z < 3$.

4.3.3.1 Concentration Evolution

The concentration of a galaxy tells us important information about how the light is distributed within a galaxy, relative to its centre. We show the evolution of the corrected concentration index defined in §4.2.2.2 in Figure 4.7 for two different mass ranges across the redshift range $0.5 < z < 3$. The concentration values have been corrected using the method described in §4.2.3.

The first includes galaxies in the mass range $10^{9.5} M_{\odot} \leq M_{*} < 10^{10.5} M_{\odot}$ and the evolution of the mean concentration for this mass bin is shown as red crosses (see Figure 4.7). The second mass bin includes galaxies that have a mass $M_{*} \geq$

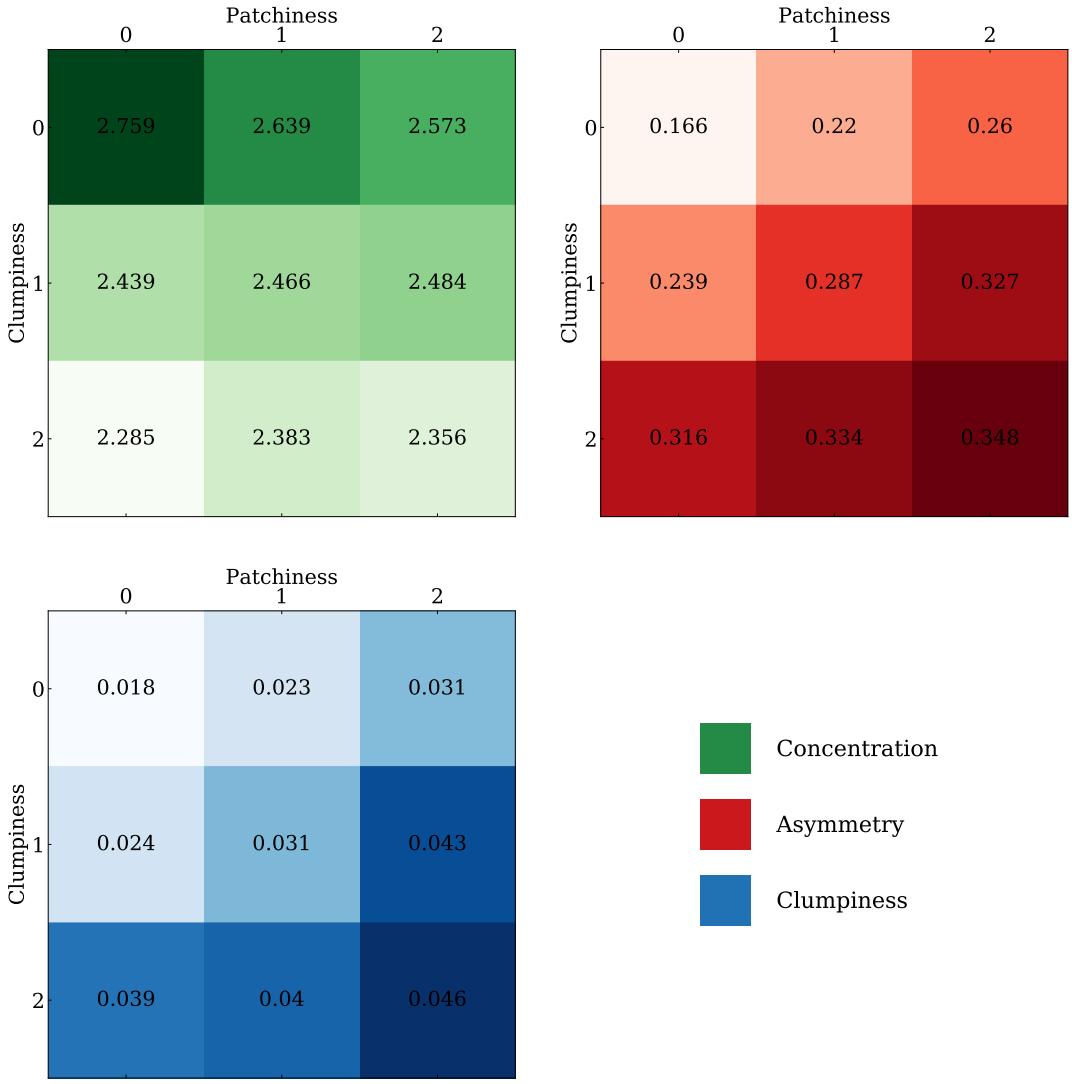

Figure 4.6: This figure shows the clumpiness (C) and patchiness (P) distribution visually vs. the CAS parameters. The values on the x- and y-axes are the visual estimates of clumpy galaxies, with high numbers denoting more visually looking clumpy systems. The clumpiness values on the y-axes are different to the clumpiness calculated by MORFOMETRYKA and are a purely visual score. Top left, green: mean concentration (C) values for each region of the clumpiness/patchiness matrix defined by Kartaltepe et al. (2015). Top right, red: mean asymmetry (A) values for each region of the clumpiness/patchiness matrix. Bottom left, blue: mean clumpiness (S) values for each region of the clumpiness/patchiness matrix. In each panel, a darker colour indicates a larger value of the relevant CAS parameter. Each three by three grid represents the clumpiness/patchiness matrix whereby a higher value on each axis represents a higher clumpiness or patchiness. The visual clumpiness/patchiness criteria appear to correlate well with the measured A and S values whilst concentrated galaxies are not visually clumpy or patchy.

$10^{10.5} M_{\odot}$. This mass bin is plotted as the blue triangles. For both, the error bars represent one standard deviation from the mean. The lower mass galaxies have a lower concentration than the higher mass galaxies, but both samples on average exhibit a decrease in concentration with time. This is opposite to what we find when we examine the uncorrected concentration index evolution. This therefore deserves some attention to try to understand the origin of this, and whether it is in fact a real effect.

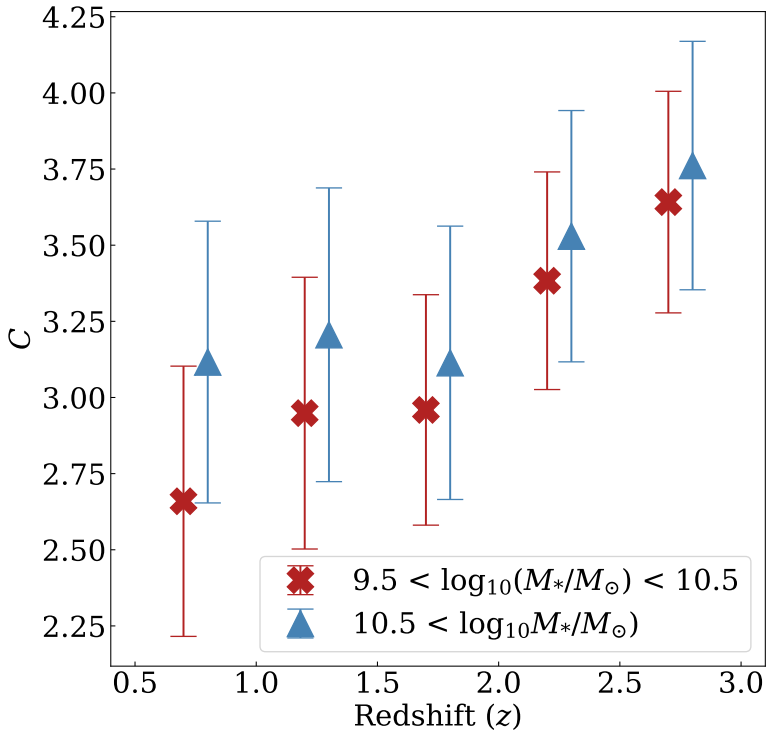

Figure 4.7: Evolution of the mean corrected concentration for both mass bins. The lower mass bin is shown as red crosses and the higher mass bin is shown by the blue triangles. The error bars represent one standard deviation from the mean. On average, the higher mass bin has a greater concentration than the lower mass bin at all redshifts, however both bins show a decrease in concentration with cosmic time.

4.3.3.2 Asymmetry Evolution

The asymmetry of a galaxy is a useful indicator as to whether a galaxy is undergoing any interactions or mergers with other galaxies (Conselice et al., 2000a,b). We explore

its use to define mergers in the following section, but first we examine the evolution of the corrected asymmetry for our sample of galaxies in the redshift range $0.5 < z < 3$. Figure 4.8 shows this evolution for two different mass ranges. As in Figure 4.7, the lower mass bin is shown as red crosses, the higher mass bin is shown as blue triangles, and the error bars represent one standard deviation from the mean. On average, the asymmetry decreases with cosmic time for both mass bins, with the higher mass bin exhibiting a steeper decrease.

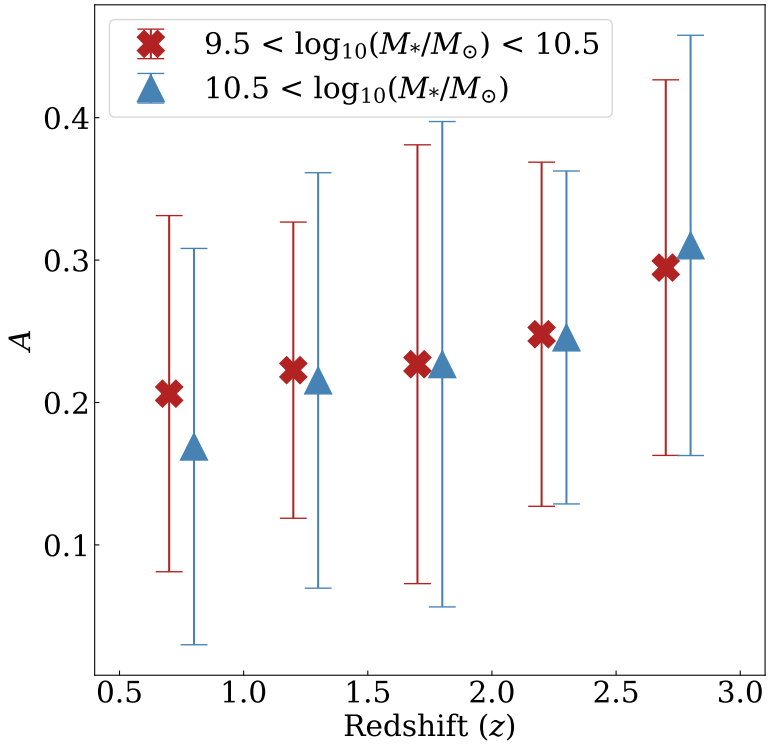

Figure 4.8: Evolution of the mean corrected asymmetry with redshift. As with Figure 4.7, the lower mass bin is shown as red crosses and the higher mass bin is shown by the blue triangles. The error bars represent one standard deviation from the mean. Both mass bins show a decrease in asymmetry with decreasing redshift.

4.3.3.3 Concentration-Asymmetry Plane

In Figure 4.9, we show the evolution of the concentration-asymmetry plane for the corrected values with redshift. As with Figures 4.4 and 4.5, we show the boundaries between the galaxy types. We also plot the three visual classifications for each galaxy, along with the position of any galaxy that does not fit these three categories within this plane. Spheroid galaxies are shown as red circles, disks as blue crosses, and peculiar galaxies as green triangles. Any other galaxies are shown as small grey circles. The spread in distribution of both concentration and asymmetry increases at lower redshifts, leading to the evolution of the average of both these parameters as seen in Figures 4.7 and 4.8.

There are few galaxies that lie within the early region of the concentration-asymmetry plane and those that do, are typically spheroid galaxies. This suggests that the galaxies within our sample are more asymmetric than is typical for spheroids. Spheroid galaxies that do not lie in this early region are mostly within the intermediate region. Within the lowest redshift bin ($0.5 < z < 1.0$), spheroids have a mean asymmetry of $\langle A \rangle$ = 0.14 and a mean concentration of $\langle C \rangle$ = 3.03. At the highest redshift ($2.5 < z < 3.0$), these values change to $\langle A \rangle$ = 0.25 and $\langle C \rangle$ = 3.77 with a steady increase in both A and C at intermediate redshifts. Disk galaxies are primarily located within the late region, as to be expected. The mean values are $\langle A \rangle$ = 0.21 and $\langle C \rangle$ = 2.52 at $0.5 < z < 1.0$ and change to $\langle A \rangle$ = 0.28 and $\langle C \rangle$ = 3.62 at $2.5 < z < 3.0$. The change in C is a steady increase however asymmetry remains at an approximately constant value until the highest redshift bin. Peculiar galaxies lie around the merger limit of $A > 0.35$ with $29.20 \pm 0.01\%$ of galaxies classified as being peculiar lying within this merger region. If these corrections are right, we can see that there is a diversity already at $2.5 < z < 3.0$ in the galaxy population and that galaxies of all types are more asymmetric and more concentrated at higher redshifts.

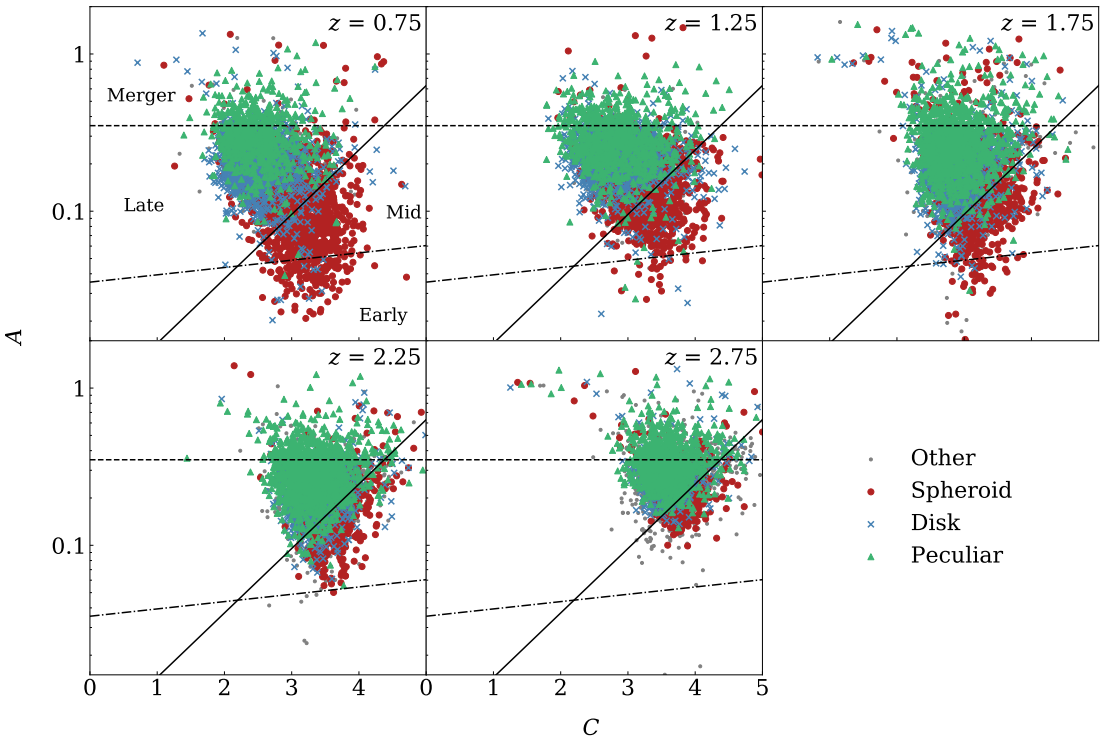

Figure 4.9: Evolution of the corrected concentration-asymmetry plane with redshift. As with Figure 4.4, the lines indicates the boundaries between galaxy types. Galaxies that lie above the dashed line are considered to be mergers. The dot-dashed line is the boundary between early- and intermediate-type galaxies and the solid line is the boundary between late- and intermediate-type galaxies. Spheroid galaxies are indicated by red circles, disks by blue crosses, and peculiar galaxies by green triangles. Galaxies that do not fall into any of the three categories are shown as small grey circles.

4.3.4 Merger Fractions and Rates

This section of the chapter describes our results of the merger history of galaxies within the five CANDELS fields using a CAS approach. The outline of this section is as follows: first we give a background description of the merger history of galaxies, including definitions of the merger process. We then describe in some detail how to measure the timescale for mergers and how these can then be used for measuring the merger rate of galaxies. Finally, from the merger rates we are able to say how many mergers these galaxies undergo on average and how much mass is added to galaxies

through this process.

4.3.4.1 Merger Fractions

In this subsection we investigate the observational quantity that we can obtain directly from the data. This is the merger fraction, which in this chapter we use the CAS parameters described in §4.2.2 to define. We later compare the merger fractions and the merger rates we derive using merger timescales to other measurements of the merger history using machine learning methods (Ferreira et al., 2020) and galaxies in pairs (Duncan et al., 2019). First we define what we mean by a merger fraction - that is, the fraction of galaxies within some galaxy sample which is undergoing a major merger.

In our sample, a merger is defined within the CAS system as a galaxy that satisfies the following criteria:

$$(A > 0.35)\ \&\ (A > S) \tag{4.8}$$

where A and S are the asymmetry and clumpiness values respectively. Both are corrected for redshift effects. This method predominantly identifies only major mergers where the ratio of the stellar masses of the progenitors is at least 1:4 (Conselice, 2003, 2006; Lotz et al., 2008). H_{160} band images of examples of galaxies we consider to be a merger, based on this system, are shown in Figure 4.10. The left two columns show lower redshift ($1 < z < 2$) galaxies, and the right two columns show higher redshift ($2 < z < 3$) galaxies. The redshift and asymmetry of each example are indicated on each postage stamp.

We calculate the merger fraction using the condition given in Equation 4.8 for each redshift bin, the evolution of which is shown in the left panel of Figure 4.12. The results

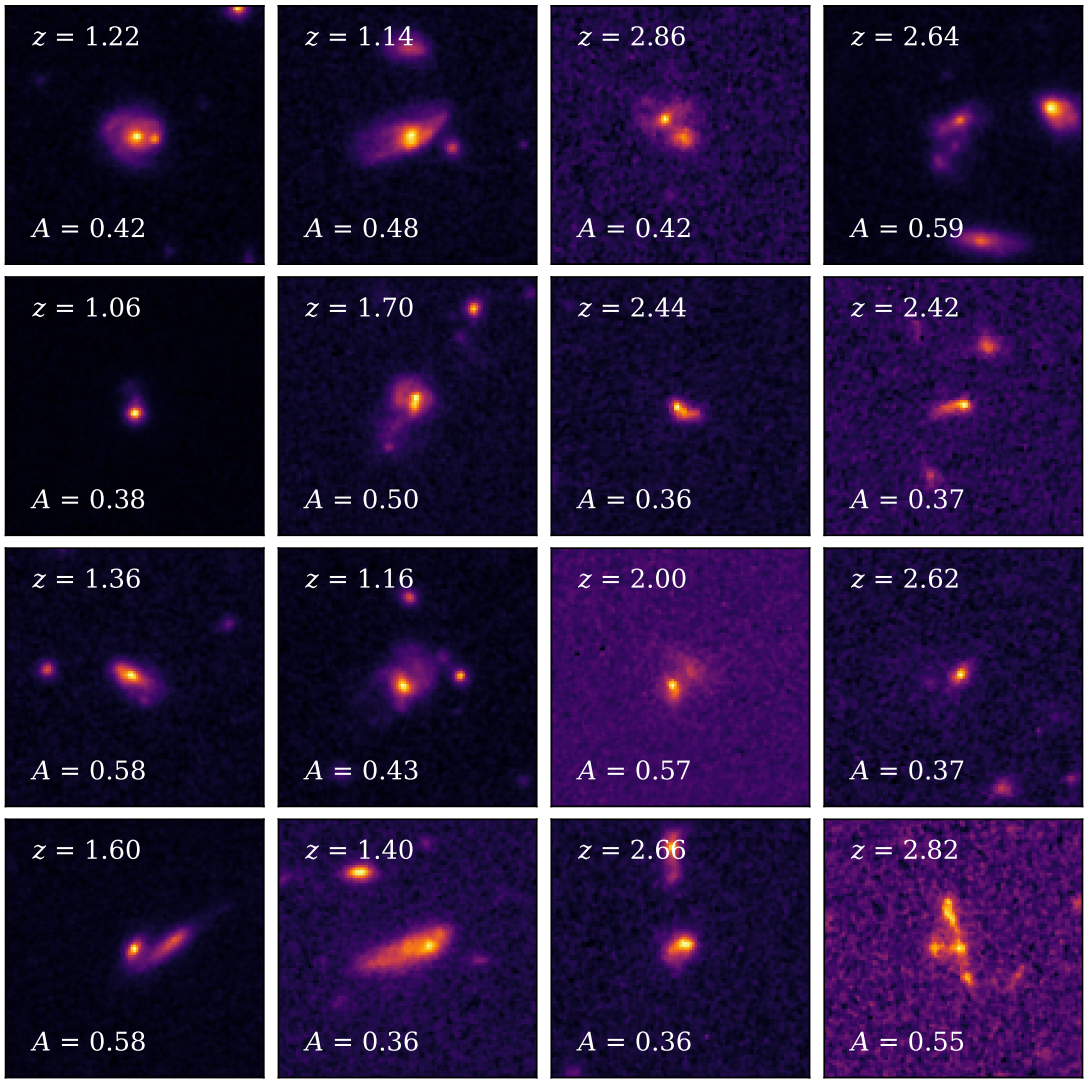

Figure 4.10: Examples of galaxies within our sample that are classified as a merger using the criteria given in Equation 4.8. Lower redshift ($1 < z < 2$) galaxies are shown in the left two columns and higher redshift ($2 < z < 3$) galaxies are shown in the right two columns. The redshift and asymmetry are given for each example.

for the low mass bin ($10^{9.5} M_\odot \leq M_* < 10^{10.5} M_\odot$) are shown as red crosses and the results for the higher mass bin ($M_* \geq 10^{9.5} M_\odot$) are shown as blue triangles. We fit a power law to the merger fraction evolution given by the form:

$$f_m(z) = f_0(1+z)^\beta \tag{4.9}$$

by applying a least squares fit to our data and setting f_0 to a fixed value of the merger fraction at $z = 0$. We take this $z \sim 0$ value to be 0.0193 ± 0.0028 from Casteels et al. (2014). This point is shown as a grey inverted triangle. We also include both mass bins in this fit. We find that the merger fraction, f_m evolves as

$$f_m = 0.019 \pm 0.004(1 + z)^{1.87 \pm 0.04}. \tag{4.10}$$

This fit is shown in the left panel of Figure 4.12 as a solid black line and one standard deviation from this fit is indicated by the grey shaded area. Also shown are the results of Duncan et al. (2019) (yellow circles) who identify mergers using pair statistics and fit a power law of the form $(1 + z)^{1.78^{+0.21}_{-0.20}}$. We also compare to Ferreira et al. (2020) (green diamonds) who identify mergers using a convolutional neural network and find that the merger fraction evolves as $(1 + z)^{2.82 \pm 0.46}$. Our merger fractions lie between these two examples. Our merger fractions and their errors are given in Columns 2 and 4 of Table 4.3 for both the lower and higher mass bins respectively.

4.3.4.2 IR Luminous Galaxies

One of the things that we need to consider in our approach is that some galaxies are invisible to optical/near-infrared light and are only detected in the far-infrared, sub-mm or radio (e.g., Wang et al., 2019). These are sometimes called H-band drop-outs and are of interest as they may in fact be galaxies that are massive, within our limits, but are not considered part of the merger fraction as they would not be added into our H-band selected sample.

A simple argument can be made to show that this concern is insignificant for our merger fractions. The study of Wang et al. (2019) found 39 galaxies across the same fields we study, which are not detected in the H-band, and thus would likely not be

within our sample. Wang et al. (2019) claim that these galaxies are typically massive ones at $z > 2$, with a median stellar mass of $10^{10.6} M_{\odot}$. Let us examine the results of assuming that all of these galaxies are mergers.

For our CANDELS sample, we have 6273 massive galaxies at $z > 2$, whilst the merger fraction we measure is $f_m = 0.183 \pm 0.005$ for these galaxies. This gives in total 1135 mergers within our sample. Then if we consider all 39 Wang et al. (2019) galaxies to be mergers at $z > 2$ and within the mass range we are looking at, then the new merger fraction with the Wang et al. (2019) drop-outs included would be (1135+39)/(6273+39) = 0.186. This gives a very small merger difference of ~ 0.003. The Poisson error on our measurements is also 0.005, at the same level. If we consider that these galaxies have the same merger fraction as the bulk of our systems, at $f_m = 0.183$, then the merger fraction would be: $f_m = 0.183$, a difference of < 0.001 - almost unchanged and vastly lower than our counting errors. We may be missing passive galaxies at $z > 3$ due to the UV selection however these will be a small fraction of the population if there are any missing at all. Therefore, this will not significantly affect our results.

Regardless, if we consider these far-infrared galaxies as mergers or that have a merger fraction higher than our measured one, it would only increase our values slightly and would be well within our current measurement errors.

4.3.4.3 Merger Timescales from IllustrisTNG

In this section we investigate the merger timescales for a sample of galaxies in the IllustrisTNG 300-1 simulation. The process we use to generate mock images is outlined in §4.2.5 and here we use only *HST*-matched mocks. We measure the observability timescales with a process similar to the one developed in Lotz et al. (2008) and Nevin et al. (2019). The main difference here is that the galaxies used in this evaluation are

generated as a result of a cosmological simulation instead of an isolated galaxy-galaxy merger simulation. Our sample is limited to massive $M_* > 10^{10} M_\odot$ major-mergers. We briefly outline our steps to measure the timescales below.

First, we follow each galaxy in the simulation for a variety of snapshots spanning ± 2 Gyr around each merger event (limited to $0 < z < 2$). The snapshot where the merger event happens is defined as the the central snapshot, S_c. This information is extracted from the merger trees in the simulation and is originally defined by the SubLink friends-of-friends algorithm (Rodriguez-Gomez et al., 2015). The snapshots after S_c are considered to be after the merger event, while the snapshot previous to S_c are classified as before the merger event. This is the only distinction done here for particular merger stages, which is fundamentally different to the stages assigned in Lotz et al. (2008).

Secondly, we select only the broadband images that correspond to the rest-frame optical at those redshifts. For these images, we measure the asymmetry using MORFOMETRYKA. Thus, for each source simulated in §4.2.5 we have A for each snapshot in four different orientations. By averaging A by the viewing angle, we find where the asymmetries of each individual galaxy falls below the $A > 0.35$ threshold for both sides of the merger event.

Finally, by comparing the time difference between where the $A > 0.35$ and $A > S$ criteria are no longer satisfied, and the redshift of the central snapshot, we estimate an observability timescale for the asymmetry, both for the post-merger stage and the before merger stage, and, if combined, for the total merger event. By doing this for all our sample, we have a statistical estimation of the merger timescales for the asymmetry in IllustrisTNG, as shown in Figure 4.11. We find a $\tau = 0.56$ Gyr, lower than the values reported in Lotz et al. (2008), but higher than the ones found in Nevin et al. (2019) for major-mergers. We find an asymmetric distribution in the timescales that is broad but not deep; there is an asymmetric tail at higher timescales. The mean timescale of this

distribution is ~20% greater than the median at 0.67 Gyr so the tail does not significantly impact the timescale used. We consider the tail in our error in the timescale by finding the differences between the median of the full sample of simulations and the median of the sample both above and below 0.56 Gyr. From this, we yield a timescale of $0.56^{+0.23}_{-0.18}$ Gyr. We find that this timescale does not vary with redshift unlike in the case of pair statistics (Snyder et al., 2017).

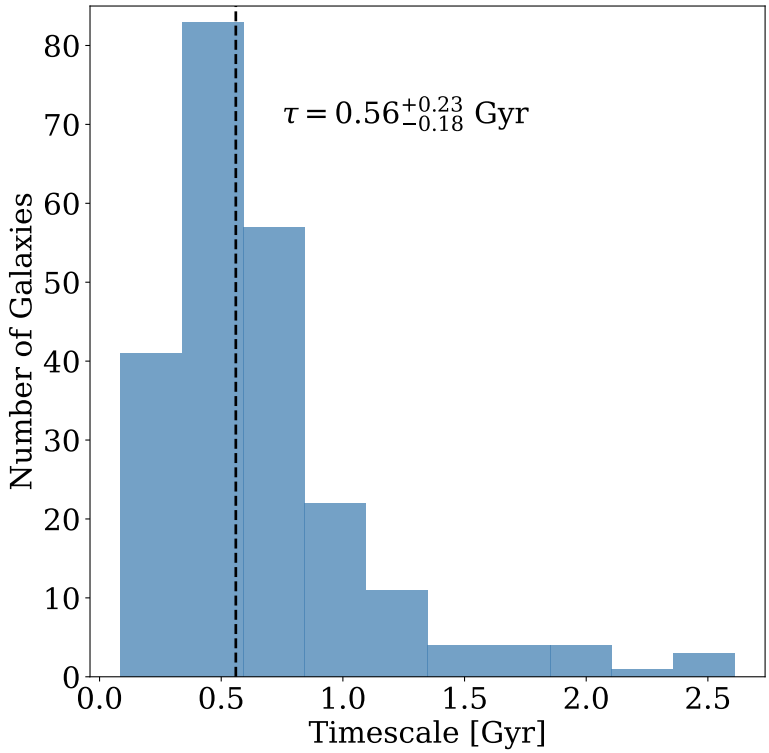

Figure 4.11: Distribution of the timescales for the total merger events within the IllustrisTNG sample. The dashed line indicates the median timescale used to determine the merger rates.

4.3.4.4 Merger Rates

Merger fractions are a solely observational quantity and can tell us little about the evolution of galaxy formation and evolution. The merger rate (time between mergers per galaxy) on the other hand is a fundamental parameter in galaxy evolution. We are

able to convert from a merger fraction to a the merger rate ($\mathcal{R}$) at each redshift using

$$\mathcal{R} = \frac{f_m}{\tau} \tag{4.11}$$

where f_m is the merger fraction and τ is the merger timescale.

We calculate the merger rate evolution for our sample of galaxies using a timescale of $\tau = 0.56^{+0.23}_{-0.18}$ Gyr found using mergers within the IllustrisTNG simulations as described above. The merger rate evolution is shown in the right panel of Figure 4.12. As with the merger fraction, we fit a power law to both the low-mass (red crosses) and high-mass (blue triangles) data of the form

$$\mathcal{R}(z) = \mathcal{R}_0(1+z)^{\beta} \text{ Gyr}^{-1} \tag{4.12}$$

where $\mathcal{R}_0$ is the local merger rate calculated using the local merger fraction, f_0, from Casteels et al. (2014) and the merger timescale we find using the IllustrisTNG simulations. This local merger rate is shown as a grey inverted triangle. We find that the merger rate evolves as:

$$\mathcal{R}(z) = 0.03 \pm 0.02(1+z)^{1.87\pm0.04} \text{ Gyr}^{-1}. \tag{4.13}$$

This fit is shown by a solid black line and one standard deviation from this fit is indicated by the grey shaded area in the right panel of Figure 4.12. As with the merger fractions, we also show the results of Duncan et al. (2019) and Ferreira et al. (2020). Due to the different methods used to identify mergers, different timescales must be used; Ferreira et al. (2020) use $\tau = 0.6$ Gyr and Duncan et al. (2019) use a timescale that varies with redshift such that $\tau = 0.17$ Gyr at $2.5 < z < 3.0$ and $\tau = 0.77$ Gyr at $0.5 < z < 1.0$

in order to calculate their merger rates.

Despite using a timescale that differs from other merger identification methods, our results are largely consistent with these previous results. Our merger rates and errors for the low and high mass bins are given in Columns 3 and 5 of Table 4.3 respectively. We also compare our results to those found by Rodriguez-Gomez et al. (2015) for the Illustris simulation. This fit is shown by a dashed line here. The fit, given in Table 1 of Rodriguez-Gomez et al. (2015), is a complex function of redshift, the descendent galaxy stellar mass M_*, and the progenitor stellar mass ratio μ_*. We show the results for a stellar mass of $1 \times 10^{10} M_\odot$ and a stellar mass ratio of 1/4 (consistent with major mergers, the type of mergers we are able to probe with our asymmetry selection). The Illustris fit is steeper than the results we find in this chapter and can be approximated as a power law of the form $\sim (1+z)^{2.7}$. These simulations also predict a smaller merger rate, particularly at the lowest redshifts, with the local merger rate predicted to be ∼3 times smaller than the value we use here.

4.3.4.5 Number of Mergers Since $z \sim 3$

From the merger rate we are able to calculate the number of mergers a galaxy at $0 < z < 3$ undergoes by integrating the inverse of the characteristic time between mergers, $\Gamma(z)$. First, we must convert the merger fraction, f_m, to the galaxy merger fraction, f_{gm}, which gives the number of galaxies merging as opposed to the number of mergers (Bluck et al., 2009). The galaxy merger fraction is given by

$$f_{gm} = \frac{2 \times f_m}{1 + f_m}. \tag{4.14}$$

We can then calculate Γ, which is essentially the time in between mergers, using this galaxy merger fraction:

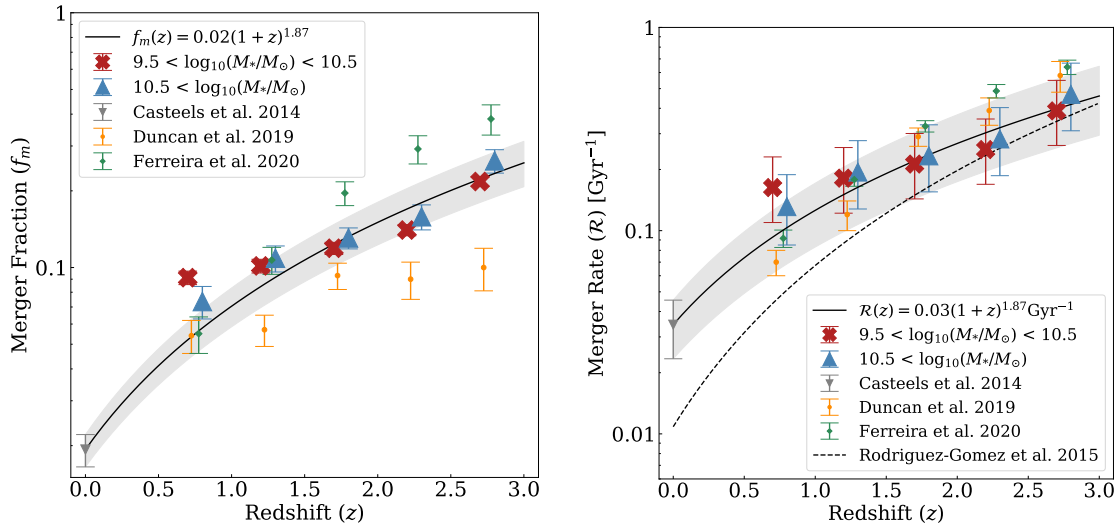

Figure 4.12: Left: evolution of the merger fraction. Right: evolution of the merger rate. The lower mass bin from this work is shown as a red cross and the higher mass bin from this work is shown as a blue triangle. The fit to both these points and a known local value from Casteels et al. (2014) (grey inverted triangle) is shown as a solid black line with the grey shaded area indicating one standard deviation from the fit. We find a fit of the form $f_m = 0.0193 \pm 0.004(1+z)^{1.87\pm0.04}$ for the merger fractions. For the merger rates, we find a fit of the form $\mathcal{R}(z) = 0.03 \pm 0.02(1+z)^{1.87\pm0.04}$ Gyr^{-1}. We compare our results to Duncan et al. (2019) (yellow circles) and Ferreira et al. (2020) (green diamonds). We also compare the merger rate to that found by Rodriguez-Gomez et al. (2015) for the Illustris simulation. This fit is given as a dashed line.

Table 4.3: Merger fractions and rates for each redshift bin and each mass bin, along with the number density-selected sample.

	$10^{9.5}M_\odot \leq M_* < 10^{10.5}M_\odot$		$10^{10.5}M_\odot \leq M_*$		Number Density-Selected	
z	f_m	$\mathcal{R}$ (Gyr^{-1})	f_m	$\mathcal{R}$ (Gyr^{-1})	f_m	$\mathcal{R}$ (Gyr^{-1})
0.75	0.091 ± 0.006	$0.163^{+0.068}_{-0.053}$	0.074 ± 0.011	$0.131^{+0.057}_{-0.046}$	0.084 ± 0.004	$0.149^{+0.062}_{-0.048}$
1.25	0.102 ± 0.006	$0.181^{+0.075}_{-0.059}$	0.108 ± 0.013	$0.194^{+0.083}_{-0.066}$	0.069 ± 0.003	$0.124^{+0.051}_{-0.040}$
1.75	0.119 ± 0.006	$0.213^{+0.088}_{-0.069}$	0.131 ± 0.012	$0.233^{+0.098}_{-0.078}$	0.081 ± 0.003	$0.145^{+0.060}_{-0.047}$
2.25	0.140 ± 0.007	$0.251^{+0.104}_{-0.082}$	0.158 ± 0.018	$0.283^{+0.120}_{-0.096}$	0.109 ± 0.003	$0.193^{+0.080}_{-0.063}$
2.75	0.217 ± 0.009	$0.388^{+0.160}_{-0.126}$	0.263 ± 0.028	$0.469^{+0.199}_{-0.158}$	0.171 ± 0.004	$0.306^{+0.126}_{-0.098}$

$$\Gamma = \frac{\tau}{f_{gm}} \tag{4.15}$$

where τ is the merger timescale. We are able to fit a power law to Γ of the form $\Gamma(z) = \Gamma_0(1+z)^{-m}$ Gyr and find that $\Gamma_0 = 14.4 \pm 0.7$ Gyr and $m = 1.96 \pm 0.13$. We calculate the number of mergers a given galaxy will undergo between redshifts z_1 and z_2, $N_{\rm m}$, using

$$N_{\rm m} = \int_{t_1}^{t_2} \frac{1}{\Gamma(z)} dt = \int_{z_1}^{z_2} \frac{1}{\Gamma(z)} \frac{t_H}{1+z} \frac{dz}{E(z)} \tag{4.16}$$

where t_H is the Hubble time, and $E(z) = [\Omega_m(1+z)^3 + \Omega_{\rm k}(1+z)^2 + \Omega_\Lambda]^{\frac{1}{2}} = \frac{H(z)}{H_0}$. We assume $\Omega_m = 0.3$, $\Omega_{\rm k} = 0$, and $\Omega_\Lambda = 0.7$.

The resulting number of mergers undergone between redshifts $z \sim 3$ and $z \sim 0$ using the time between mergers of $\Gamma(z) = 14.4 \pm 0.7(1+z)^{-1.96\pm0.13}$ Gyr is shown in Figure 4.13 as a solid red line. We estimate that a galaxy with mass $M_* > 10^{9.5} M_\odot$ will undergo $2.90^{+0.50}_{-0.41}$ major mergers on average between $z \sim 3$ and $z \sim 0$, with $1.87^{+0.39}_{-0.31}$ mergers occurring before $z \sim 1$. This result lies between some previous results; Bluck et al. (2009) find that massive ($M_* > 10^{11} M_\odot$) galaxies undergo 1.7 ± 0.5 major mergers with a timescale of $\tau = 0.4$ Gyr from $z \sim 3$ to $z \sim 0$. Conselice (2006) find that galaxies with $M_* > 10^{10} M_\odot$ undergo $4.4^{+1.6}_{-0.9}$ major mergers at $z > 1$ but undergo less than a single merger at $z < 1$. For comparison, we also plot the evolution of the number of mergers for a constant merger rate where we set $\Gamma(z)$ to be that at $z = 3$ to show how many mergers would occur without the observed decrease in merger rate. This is shown as a blue dashed line. The grey shaded areas on both lines indicate the error on the number of mergers.

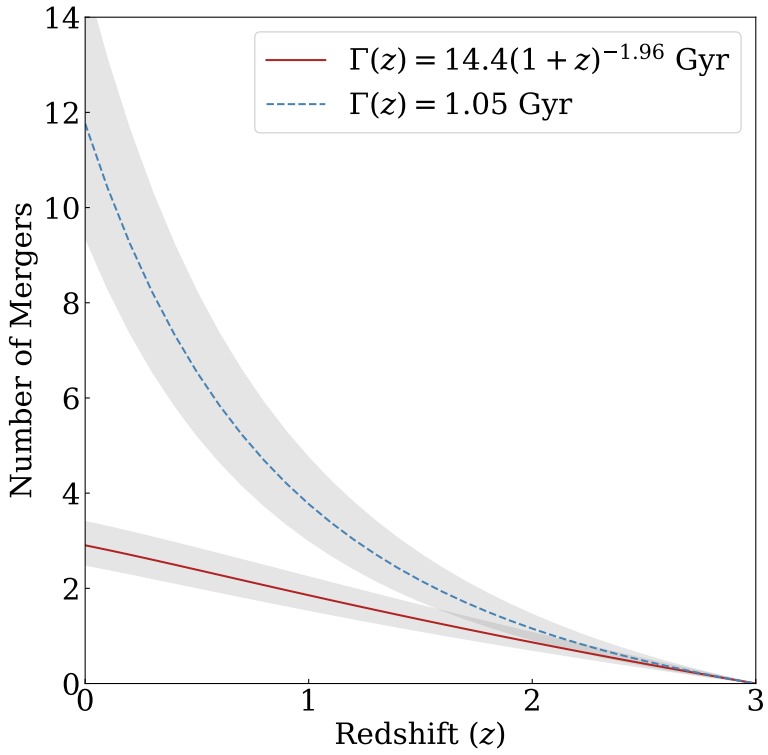

Figure 4.13: The total number of mergers since $z \sim 3$, as a function of redshift. The solid red line shows this quantity for $\Gamma = 14.4 \pm 0.7(1+z)^{-1.96\pm0.13}$ Gyr. We find that galaxies with $M_* > 10^{9.5} M_\odot$ undergo ~ 3 mergers on average since $z \sim 3$. For comparison, also shown is the evolution of the number of mergers for a constant merger rate of $\Gamma = 1.05$ Gyr, which is equal to the merger rate at $z = 3$. This is indicated by a blue dashed line. The grey shaded regions indicate the error range on the number of mergers.

We are then able to determine how much mass is added to a galaxy due to these mergers. Major mergers as identified by the CAS parameters are defined as galaxy mergers where the mass ratio between the progenitors is $\mu = 1/4$ or less and so the amount of mass added to a galaxy during a merger must be similar to the original galaxy's mass. We take the ratio between progenitor masses to be an average of 1:1.5, as in Conselice (2006), and we approximate the amount of stellar mass gained by a galaxy due to mergers by $\Delta M_{\rm merger} \sim 1.65^{N_m} \times M_0$, where N_m is the number of mergers and M_0 is the mass of the initial galaxy (Conselice, 2006). Therefore, a galaxy of mass $M_* = 10^{9.5} M_\odot$ at $z = 3$ will gain a of mass $M_* = 1.3 \times 10^{10} M_\odot$ by $z = 0$, giving a

relative mass increase from $z = 3$ to $z = 0$ of $\Delta M_{\rm merger}/M = 3.2$. A galaxy of initial mass $M_* = 10^{10.5} M_\odot$ will, on average, accumulate $M_* = 1.4 \times 10^{11} M_\odot$ by $z = 0$, giving a relative mass increase of $\Delta M_{\rm merger}/M = 4.1$. The mass accretion rate, in terms of the amount of mass accreted from mergers per unit time, is $\dot{M} \sim 10^9 M_\odot$ Gyr^{-1} at $M_* = 10^{9.5} M_\odot$, while for $M_* = 10^{10.5} M_\odot$ the mass accretion rate is a factor of ten times high, on average, giving $\dot{M} \sim 10^{10} M_\odot$ Gyr^{-1}.

These are simply the average mass accretion rates per Gyr. Naturally, this process is not smooth and mass will be added in discrete jumps during the 2.9 mergers at $z < 3$. However, this mass accretion rate due to mergers per galaxy is an average value for all galaxies that can be applied to a mass selected population.

4.3.5 Comparison to Simulations

We compare our results to simulations within IllustrisTNG. Instead of using TNG300-1 as we do to determine the merger timescale, we use the higher resolution TNG50-1. This is done to ensure that morphologies are not affected by mass or spatial resolution, especially in the central regions. For TNG300-1, the radius containing 20% of the light, R_{20}, is close to the softening length of the simulation for some galaxies, and as a result could impact the concentration measurement. The softening length is the scale at which gravity can no longer be considered to be Newtonian so particles might act differently to a real galaxy below this. From TNG50-1 we randomly select galaxies in the same mass range as our mass-selected sample, generate the mocks following the description in §4.2.5, and measure the CAS parameters using MORFOMETRYKA. In Figure 4.14, we show a comparison of the concentration evolution for our results from CANDELS and the IllustrisTNG simulations. The CANDELS results are corrected for redshift effects, as described in §4.2.3. The IllustrisTNG simulations images are produced to have at

least 3 times the resolution of the CANDELS images and have not been matched with *HST* realism as the concentration should be universal for all resolutions. The resulting images are 640 × 640 pixels and the spectra have been shifted to coincide with the same filters as in Table 4.1. As with Figure 4.7, the CANDELS low mass galaxies ($10^{9.5} M_{\odot} < M_{*} < 10^{10.5} M_{\odot}$) are shown as blue triangles and the CANDELS high mass galaxies ($10^{10.5.5} M_{\odot} < M_{*}$) are shown as red crosses. The low mass IllustrisTNG simulations are shown as a dashed orange line and the high mass simulations are shown as a solid green line. We find that the concentration of the simulations show very little evolution with redshift for both mass bins. This suggests that the galaxies are growing in size with the inner and outer regions growing at a similar rate whereas the trend in the CANDELS data suggests the galaxies are growing from the inside out.

We also compare the measured merger fractions within the simulations to the CANDELS data. For this, we randomly select 5% of all available galaxies in TNG50-1 in this mass range. As this naturally selects more galaxies in the low mass bin than in the high mass bin, we further select more galaxies for the high mass bin until both bins have the same number of galaxies. The simulations in this case are calibrated on *HST* resolution. This comparison is shown in Figure 4.15. As for Figure 4.12, the CANDELS data is shown as red crosses (low mass bin) and blue triangles (high mass bin). The IllustrisTNG merger fraction evolution determined using the same asymmetry condition as used for the CANDELS data for the low and high mass bins are shown as a solid orange line and a dashed green line respectively. We also determine the 'true' merger fraction within the simulation by using the merger labels produced based on the merger trees. We ensure we only select major mergers by selecting mergers that have a mass ratio greater than 1/4. We also select only those galaxies that are within 0.65 Gyr of their merging event, a time between the median and mean of our CAS merger time-scale. These 'true' merger fractions are shown as a purple dotted line and a dot-dashed yellow

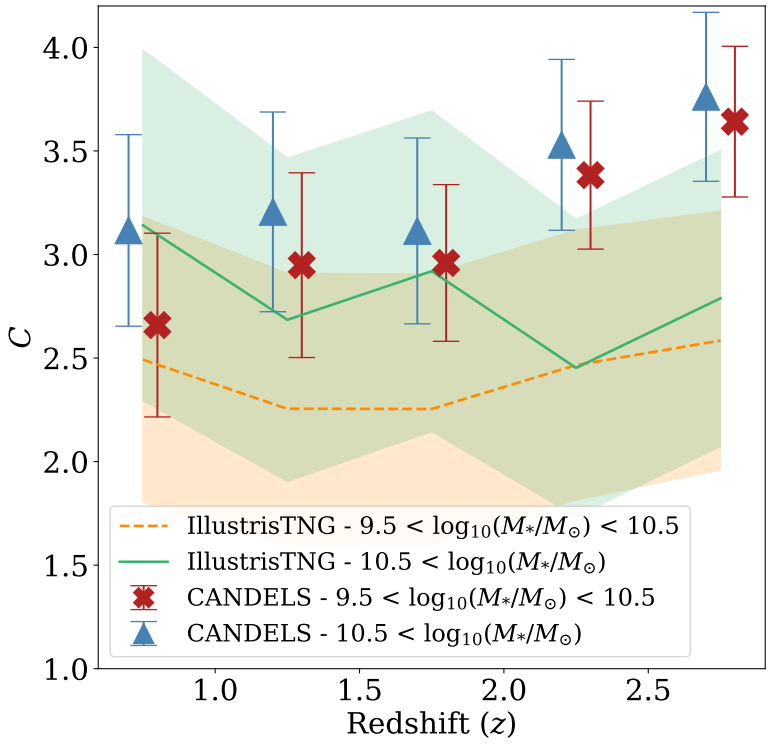

Figure 4.14: Comparison of the evolution of the concentration for our results from CANDELS (corrected for redshift effects) and the galaxies within the IllustrisTNG simulations. As with Figure 4.7, the CANDELS low mass ($10^{9.5} M_{\odot} < M_{*} < 10^{10.5} M_{\odot}$) galaxies are shown as blue triangles and the CANDELS high mass ($10^{10.5.5} M_{\odot} < M_{*}$) galaxies are shown as red crosses. The low mass IllustrisTNG simulations are shown as an dashed orange line and the high mass simulations are shown as a solid green line. The shaded regions indicate one standard deviation from the mean. The IllustrisTNG data is based upon high resolution images.

line for the low and high mass bins respectively. The shaded regions show the error on the merger fractions for the IllustrisTNG simulations. We find that the asymmetry defined merger fractions are largely consistent with the observations. However the 'true' and asymmetry defined mergers are not in agreement in terms of merger fraction at high redshift. As such, this could explain the high observed merger fraction in the final redshift bin; the observations are contaminated by false mergers at high-z, something also seen in the simulations. When selecting galaxies within a shorter timescale than the one chosen here, the number of galaxies in each redshift bin are too few and thus the

'true' merger fractions decrease and do not agree very well with the asymmetry selected mergers from IllustrisTNG or the CANDELS data. This in part happens due to the time resolution between snapshots in IllustrisTNG, which is roughly $\Delta t \sim 0.16$ Gyr.

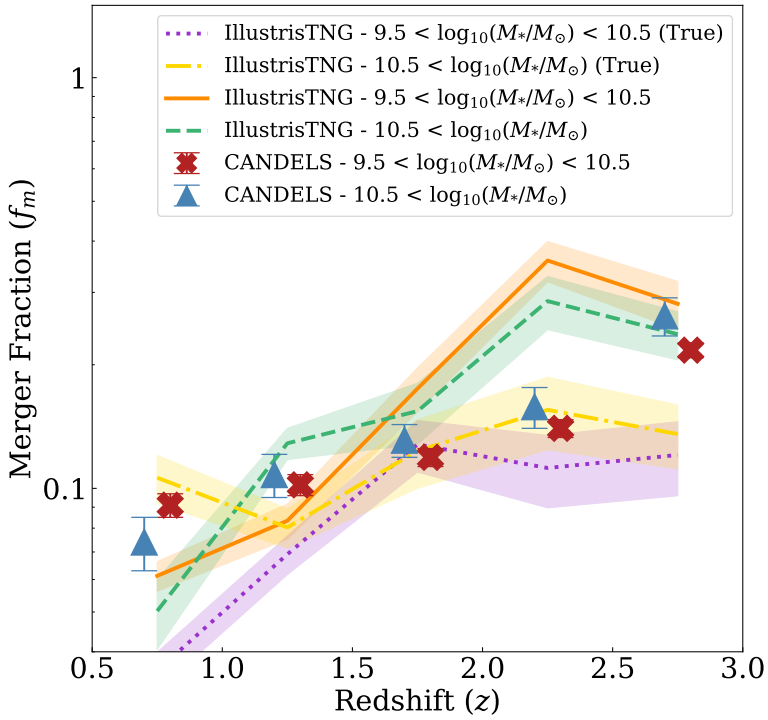

Figure 4.15: Comparison of the evolution of the merger fraction for our results from CANDELS and the galaxies within the IllustrisTNG simulations. The IllustrisTNG data is based upon *HST* matched mocks. As with Figure 4.7, the CANDELS low mass ($10^{9.5} M_\odot < M_* < 10^{10.5} M_\odot$) galaxies are shown as blue triangles and the CANDELS high mass galaxies ($10^{10.5.5} M_\odot < M_*$) are shown as red crosses. The merger fraction evolution for the simulations determined using the asymmetry condition is shown as a solid orange line and a dashed green line for the low and high mass bins respectively. Also shown are the 'true' merger fractions - the merger fraction determined based on the labels from the merger trees within the simulations. We select galaxies that are within 0.65 Gyr of a merging event, a value between the median and mean of the CAS timescale distribution. These merger fractions are shown as a purple dotted line and a dot-dashed yellow line for the low and high mass bins respectively. Our results are consistent with both the asymmetry defined mergers and the 'true' mergers from the simulations.

We explore how many of galaxies within the Illustris simulation have $A > 0.35$ and also are considered to be a 'true' major merger (with a mass ratio greater than 0.25). In this case we consider galaxies that are within 0.45 Gyr of a merger event, or 0.9 Gyr in

total, to be 'true' mergers in order to account for the time difference between snapshots within the simulation. We find that across all redshifts, an average of $\sim$ 37% of the 'true' major mergers lie above $A > 0.35$. This is slightly lower than the $\sim$ 50% found by Conselice (2006).

4.4 Discussion

In this chapter we have discussed and presented a number of observed features of galaxy evolution, as viewed through the structurally changes in galaxies over the past 11 Gyr. We carry this out through an analysis of all five CANDELS fields, examining the change in light concentration and asymmetry for these systems. As opposed to other studies of galaxy evolution at these epochs we take a largely structurally evolutionary view of galaxies, rather than one based on stellar populations. In this viewing of galaxies we are interested in the build up of stars in galaxies and how that affects the distribution of light within galaxies, rather than examining the type and distribution of stars themselves.

4.4.1 Concentration

We find that galaxies are more concentrated at higher redshifts when probing galaxy structure in the optical rest-frame. This is an interesting result and is somewhat different from expectations, so it is important to examine the reasons for this. We test this result by examining the evolution of the concentration calculated using various measures of size. First, we correct the radii R_{20} and R_{80} (where R_{20} is the radius containing 20% of the total light within a galaxy and R_{80} is the radius containing 80% of the light) using the same method as described in §4.2.3 and use the mean of these corrected values to calculate the concentration using Equation 4.2.

Examining the individual radii for our sample, we find that the evolution of the corrected R_{80} values remain roughly constant with redshift whereas R_{20}, on average, increases with redshift. Therefore, we see a lower concentration at lower redshifts. We show the evolution of the concentration calculated using the corrected values of R_{20} and R_{80} in Figure 4.16. As in Figure 4.7, the low mass bin is shown as red crosses and the high mass bin is shown as blue triangles. Also shown are power law fits to the concentrations, with the dotted line being for the low mass bin and the dashed line being for the high mass bin. For comparison, we show the evolution of the measured value of C for all masses as grey circles. This decrease in concentration is consistent with the corrected concentrations shown in Figure 4.7. However, there is some evidence that the relationship is shallower.

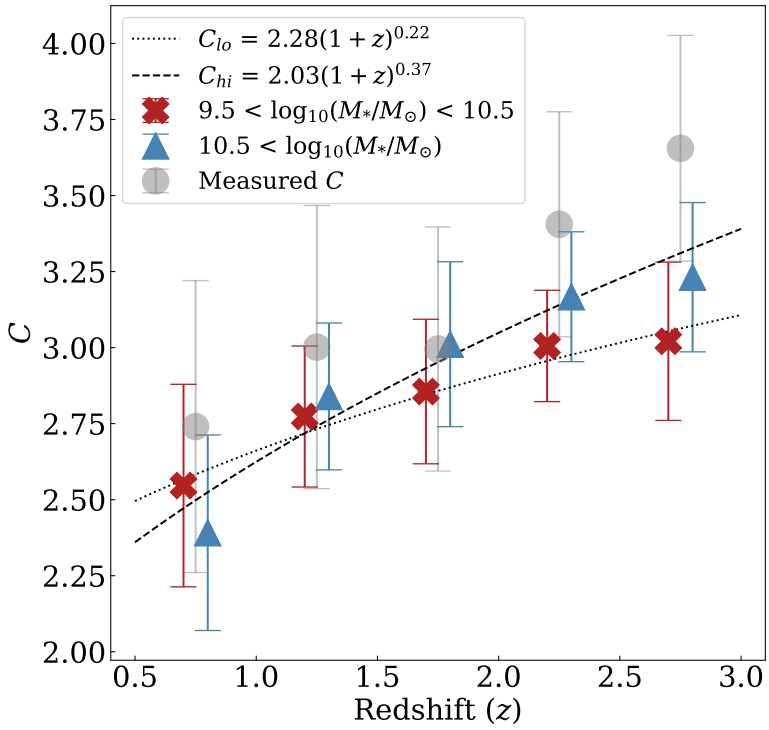

Figure 4.16: Evolution of the concentration as calculated from the corrected R_{20} and R_{80} growth radii. The low mass bin is shown as red crosses and the high mass bin is shown as blue triangles. The grey circles represent the evolution of the measured concentration across all masses.

We further explore this by examining the Petrosian radius, $R_{\rm Petr}(\eta)$. The Petrosian radius is defined to be the radius at which the surface brightness at a given radius is a specific fraction (η) of the surface brightness within that radius (e.g., Bershady et al., 2000; Conselice, 2003; Whitney et al., 2019). η is given by:

$$\eta(r) = \frac{I(r)}{\langle I(r) \rangle} \tag{4.17}$$

where $I(r)$ is the surface brightness at radius r and $\langle I(r) \rangle$ is the mean surface brightness within that radius. Using this definition, $\eta = 0$ at large radii. We consider $R_{\rm Petr}(\eta = 0.2)$ (the outer edge of a galaxy) and $R_{\rm Petr}(\eta = 0.8)$ (the inner region of a galaxy). Whitney et al. (2019) show that $R_{\rm Petr}(\eta = 0.2)$ grows more rapidly than $R_{\rm Petr}(\eta = 0.8)$ for a mass-selected sample (where the masses lie in the range $10^9 M_\odot < M_* < 10^{10.5} M_\odot$) across a redshift range of $1 < z < 7$ in the GOODS-North and GOODS-South CANDELS fields. So, one would expect the concentration at lower redshifts to be larger. In the same fashion as with the growth radii, we calculate the concentration of the galaxies in Whitney et al. (2019) with mass $\log_{10}(M_*/M_\odot) > 9.5$ using the Petrosian radii such that

$$C_{\rm P} = 5 \times \log_{10}\left(\frac{R_{\rm Petr}(\eta = 0.2)}{R_{\rm Petr}(\eta = 0.8)}\right). \tag{4.18}$$

The resulting concentration evolution is shown in Figure 4.17. We fit a power law to the entire redshift range from Whitney et al. (2019) (dotted line) and also the redshift range we consider in this chapter (solid line). We find that $C_{\rm P}$ goes as $(1+z)^{-0.09\pm0.06}$ for the redshift range of $1 < z < 6$ and goes as $(1+z)^{0.09\pm0.09}$ for the smaller redshift range of $1 < z < 3$, which is within 1σ of being considered a flat relation. The vertical dashed line indicates the redshift limit of this work. Whilst on average over the redshift range of $1 < z < 6$, the concentration decreases with redshift, when we consider the lowest

redshift bins, the concentration appears to increase with redshift, which is consistent with the results we find and show in Figure 4.7. This is due to the fact that the inner radius appears to grow more rapidly compared to the outer radius within this small redshift range. We find the same result when considering galaxies with $\log_{10}(M_*/M_\odot) > 10.5$. This difference in evolution at higher and lower redshift ranges could be highlighting a change in formation mechanisms at $z = 2 - 3$ whereby the outer regions grow more rapidly at earlier times and the inner regions grow more rapidly at later times.

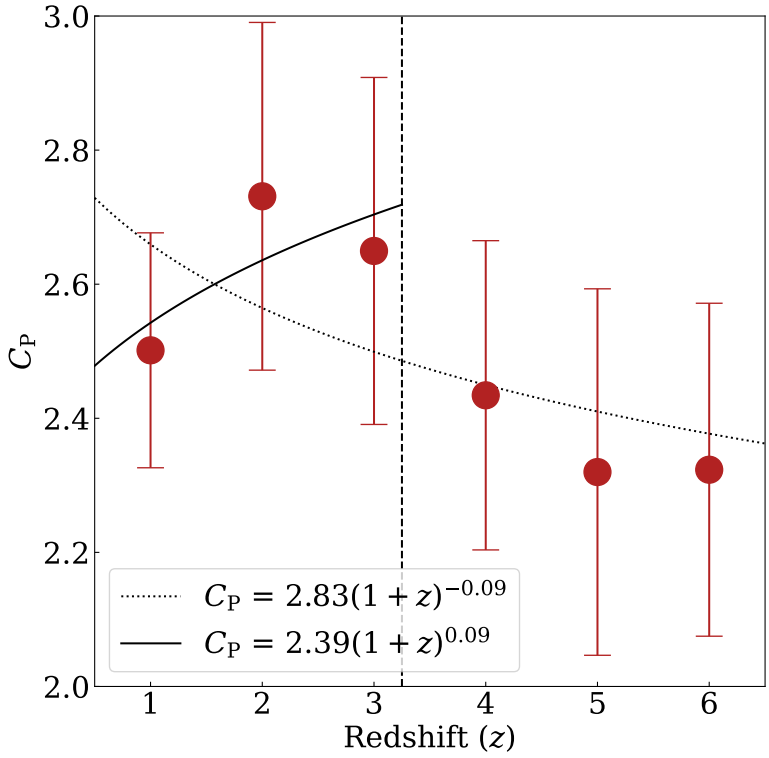

Figure 4.17: Evolution of the concentration calculated using the Petrosian radii at $\eta = 0.2$ and $\eta = 0.8$ as per Equation 4.18 for galaxies of mass $\log_{10}(M_*/M_\odot) > 9.5$ from Whitney et al. (2019). We fit a power law to the whole redshift range, shown as a dotted line, and also to the redshift range we consider here (solid line). We find that C_P goes as $(1+z)^{-0.09\pm0.06}$ for the redshift range of $1 < z < 6$ and as $(1+z)^{0.09\pm0.09}$ for the smaller redshift range of $1 < z < 3$. The vertical dashed line indicates the redshift limit of this work. On average, the concentration decreases at higher redshift however when considering the lowest redshifts, the concentration increases with redshift.

Alternatively, it might be the case that as we go to lower redshifts, we are sampling

more and more galaxies using a constant mass limit (Mundy et al., 2015). The result of this is that intrinsically lower halo mass galaxies will be entering our sample and these may have lower concentrations. In order to test whether the mass limits of our sample are creating an artificial trend, we instead select galaxies using a constant number density of 3×10^{-5} Mpc^{-3}. This yields galaxies in the mass range $10^{10.7} M_{\odot} \leq M_{*} < 10^{11.5} M_{\odot}$. This method avoids problems with having a fixed stellar mass bin that galaxies can enter at lower redshift, compared with those that are at higher redshifts (e.g., Mundy et al., 2015; Ownsworth et al., 2016). This has an effect such that by $z = 0$ only ~ 5 % of galaxies with a high mass selection would have been within the same mass selection at $z > 2.5$. However, by selecting through a constant co-moving number density we are able to remove this bias and always examine what are statistically the same number of massive galaxies at each redshift. Because there are so many 'new' galaxies in a mass-selected sample, it is possible that the relations we derive are biased by these new systems.

We determine the concentration evolution for this number density-selected sample, and compare it to the evolution seen for the mass selected-sample. We find that the evolution for the number density-selected sample is very similar to that of the mass-selected sample, as shown in Figure 4.18. Green circles indicate the concentration for the number density-selected sample, red crosses indicate the lower mass bin, and blue triangles the higher mass bin. Therefore our finding of a reduction in concentration using the mass selected sample is not due to new galaxies entering the criteria.

As a test for another key result, we examine how the merger fraction evolution would occur by using a selection based on this number density selection of 3×10^{-5} Mpc^{-3}. This is shown in Figure 4.19 where we find that the merger fraction is slightly lower for all but the final lowest redshift bin. The values for the merger fraction and merger rate for this number density-selected sample are shown in Table 4.3. However, the fitted

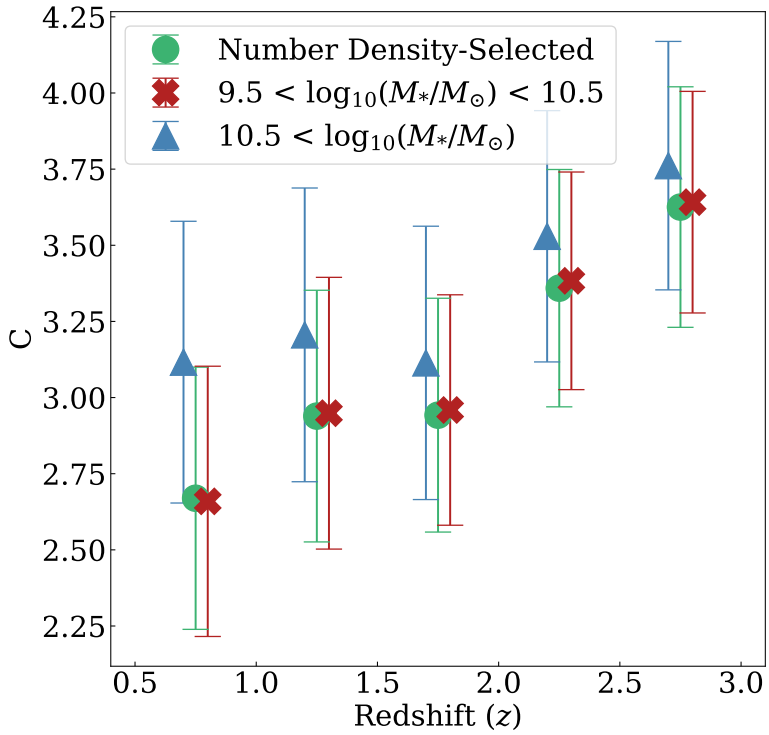

Figure 4.18: A comparison of the evolution of concentration for a number density-selected sample (green circles) and a mass-selected sample. The number density is kept constant at 3×10^{-5} Mpc^{-3}. As for Figure 4.7, red crosses indicate the lower mass bin and blue triangles indicate the higher mass bin. We find no significant difference in the evolution of the C parameter using these different selection methods.

merger fraction evolution and thus the corresponding merger rate is statistically very similar and does not give significantly different merger histories for galaxies. Thus, our result using a constant mass selection is a viable way in which to trace the evolution of the massive galaxy population, and our results are robust to galaxy selection methods.

Radius measurements of the inner regions can be inaccurate due to factors such as the size of the PSF. This could create inaccuracies in the concentration measurement. To ensure the concentration evolution we see is not an artefact of such issues, we also use R_{50} and R_{90} values in place of R_{20} and R_{80} in Equation 4.2. We find that the evolution of C_{59} exhibits similar behaviour to C_{28}, whereby the concentration increases by a factor of $\sim$1.5 over the redshift range $0.5 < z < 3$. We can therefore conclude that the evolution

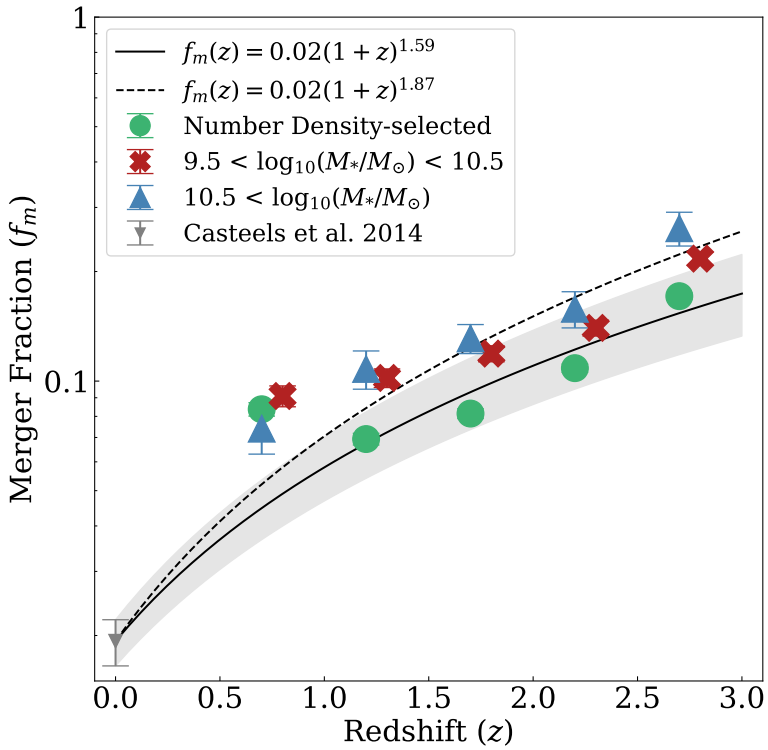

Figure 4.19: A comparison of the evolution of the merger rate for a number density-selected ($n = 3 \times 10^{-5}$ Mpc^{-3}) sample of galaxies (green circles), low mass galaxies (red crosses), and higher mass galaxies (blue triangles). The fit to the number density-selected sample is shown by the solid line and the fit to the mass-selected sample is shown by the dashed line.

in concentration we see is real and not as a result of problems with the inner radius measurement.

We interpret a decreasing concentration with lower redshift as an indication that a small initial galaxy will eventually grow in size as a result of galaxy mergers, as well as galaxy accretion. This growth is occurring in such a way that the inner regions of a galaxy grow more rapidly in comparison to the outer regions at $z < 3$. Examining the Petrosian radius evolution over a larger redshift range than is done here gives the opposite result.

4.4.2 Merger Consistency

Mergers can be identified in multiple ways such as pair statistics (e.g., Bundy et al., 2009; Man et al., 2016; Mundy et al., 2017; Duncan et al., 2019), CAS (e.g., Conselice & Arnold, 2009; Bluck et al., 2012), Gini-M_{20} (e.g., Lotz et al., 2008, 2010), and Deep Learning (e.g., Ferreira et al., 2020) with each of these methods yielding differing merger counts, and therefore fractions due to the different criteria. Using a power law fit, we find that the merger fraction goes as $(1+z)^{1.87\pm0.04}$ when fitting our data and setting the $z \sim 0$ merger fraction to a fixed value. This is shallower than that found by Conselice & Arnold (2009) who derive merger fractions using the CAS parameters for a sample of galaxies within the Extended Groth Strip and Cosmic Evolution Survey at $0.2 < z < 1.2$; they find a relation of $(1+z)^{2.3\pm0.4}$ using their data and by using a fixed value of the merger fraction at $z \sim 0$, the relation changes to $(1+z)^{3.8\pm0.2}$. Ferreira et al. (2020) use a convolution neural network trained on simulations from IllustrisTNG and applied to data from all five CANDELS fields and find an evolution of $(1+z)^{2.82\pm0.46}$, again slightly steeper than the results we find. Duncan et al. (2019) on the other hand find a shallower relation for their pair fractions of $(1+z)^{0.844^{+0.216}_{-0.235}}$ for galaxies with $\log_{10}(M_*/M_\odot) > 10.3$. In general, the morphologically defined mergers give a higher merger fraction than those derived through pairs (Conselice & Arnold, 2009). However, this is not unexpected, as different methods of finding mergers will give different results for the fractions.

Consistency is however expected when converting to merger rates and comparing these values. Along with different methods giving different merger fractions, different selection criteria within the same sample also give varying results; Man et al. (2016) examine the pair fraction evolution up to $z \sim 3$ using the UltraVISTA/COSMOS K_S-band selected catalog along with 3DHST+CANDELS H-band imaging and explore the effect of using the flux ratio versus the mass ratio in the selection. When selecting

via the stellar mass ratio, the merger fraction appears to increase with cosmic time in contradiction to the results we and others find. A selection via the H-band flux ratio however, the trend is similar to ours in that the merger fraction decreases.

As with merger fractions, merging timescales vary quite drastically depending on the selection method. For example, Lotz et al. (2008) use GADGET N-Body hydrodynamical simulations and the radiative transfer code SUNRISE to create a sample of galaxy mergers. These are used to determine the merging timescales for multiple methods of identifying mergers. Using the same asymmetry condition we use here, a timescale of 0.94 ± 0.13 Gyr is determined, whilst using a Gini and M_{20} condition, the timescale is found to be 0.26 ± 0.10 Gyr. Conselice et al. (2008) who examine the merger rate up to $z \sim 3$ in the Hubble Ultra-Deep Field use a merger time-scale of 0.34 Gyr, determined using the asymmetry condition. These methods all assume a constant timescale with redshift, however using a close pair method of identifying mergers, Snyder et al. (2017) find that the timescale varies with redshift as $\tau \propto (1+z)^{-2}$. These timescales all differ from the constant timescale of $\tau = 0.56^{+0.23}_{-0.18}$ Gyr we find using the asymmetry criteria.

Despite these differences in timescales and merger fractions for various methods of identifying mergers, merger rates are largely consistent with each other, as shown in Figure 4.12. The merger rates determined using the asymmetry condition to identify mergers as we have done here are, within the errors, similar to merger rates determined using other methods such as probabilistic pair-counts (Duncan et al., 2019) and finding mergers using Deep Learning (Ferreira et al., 2020). This is despite using different timescales for a merging event, showing that while different methods identify different numbers of mergers, our CAS method gives a consistent merger history for galaxies. The merger rates presented here have greater errors associated with them than previous work due to the consideration of the error in the merger timescale; the IllustrisTNG simulations used here to determine the merger timescale have an asymmetric distribution

in the timescale and so we therefore use an asymmetric error. Ferreira et al. (2020) use a timescale based on their selection and as such, do not have an associated error. Duncan et al. (2019) calculate the errors on their merger fractions using the bootstrap technique. The timescale taken from Snyder et al. (2017) does not have an associated statistical error so when determining the fit (by convolving the merger fraction fits with the redshift dependent timescale), the merger rates only consider the error in merger fraction. Therefore, we have found that using three independent methods that we are able to measure a consistent merger rate at $z < 3$, and therefore have a firm idea of what the history of galaxy major mergers are within this redshift range.

4.5 Conclusions

Galaxy structure is one of the most fundamental ways in which galaxies and their formation and evolution can be understood, yet there have been few systematic studies of this property at higher redshifts. In this chapter we collate the high resolution *HST* imaging of galaxies from all five fields of the CANDELS survey to determine the time evolution of galaxy structure to derive the processes for galaxy evolution. We combine these 16,778 galaxy structures, both visually based and quantitatively based, with stellar mass measurements and photometric redshifts to derive the evolution of galaxy structure. To aid our investigation of these morphologies we also utilise Illustris TNG300 simulations to calibrate timescales for morphological features and Illustris TNG50 for direct morphological comparisons with observations.

Our conclusions, based on a detailed non-parametric analysis of the structures of galaxies in all five CANDELS fields are as follows:

1. We find that galaxies are distributed in a concentration-asymmetry plane up to

$z \sim 3$ in a similar way as they do at lower redshifts. At these redshifts there is a continuum of parameters, suggesting unlike the colour-magnitude plane galaxies on this relation evolve continuously over time, rather than change dramatically.

2. Based on dynamical simulations with the IllustrisTNG simulation, we show that the evolution of galaxies within the $C - A$ plane over this time period is largely driven by galaxy formation processes, including the accretion of gas as well as galaxy mergers.

3. We find that galaxies are both more asymmetric and more concentrated at higher redshifts. This demonstrates that galaxies are assembled in a way where material is coming in through galaxy formation processes that are relatively changing the inner portions of galaxy light quicker than the outer radii at $z < 3$. The opposite is found when examining the evolution of the Petrosian radius, however the Petrosian radius concentration measure indicates a decreasing concentration at low redshifts.

4. Using merger timescales from Illustris TNG300 we determine how the morphological timescale for mergers evolves with time. We find that for the CAS system of finding mergers, the mean merger timescale is $0.56^{+0.23}_{-0.18}$ Gyr. We also find, that unlike in the galaxy pair situation, this merger timescale does not evolve with time.

5. Using these timescales we are able to determine the merger fraction evolution and the merger rate evolution up to $z \sim 3$. We find a good agreement between our merger rate calculations in comparison with previous work using pairs of galaxies and finding mergers based on Deep Learning. This is therefore a consistent merger history for galaxies as measured in three different ways. We now have a firm and consistent measure of the galaxy major merger history at $z < 3$.

Our results are the best measurements of the merger history using *HST* imaging that

will likely be possible unless a new large area survey in the near infrared is performed. When Euclid and *JWST* launch we will be able to expand these results in many ways. We will be able to measure the merger history in a similar way up to $z \sim 6$, and at lower redshifts we will be able to probe down to lower masses to find the evolution of a fuller sampling of the galaxy population. Euclid will allow us to examine the merger history over 15,000 deg^2, allowing detailed merger histories to be measured. The techniques and methods here can be used with both data sets, and others, to fully explore and measure this merger history, a principle part of the entire galaxy formation process.

Chapter 5

Conclusions and Future Work

This thesis utilises the deep *HST* imaging offered by the extensive CANDELS survey to explore galaxy evolution. In Chapter 2, I explore how the Petrosian radius evolves as a function of cosmic time for a sample of galaxies across a redshift range of $1 < z < 7$, in the rest-frame optical. I also describe the methods used to remove foreground objects from images of galaxies, making use of the Lyman break. In Chapter 3, I examine the evolution of galaxy surface brightness over a redshift range $1 < z < 6$ in the rest-frame UV and how this affects the detectability of galaxies at the highest redshifts. Finally, in Chapter 4, I present an analysis of non-parametric measures of galaxy structure for a low redshift sample of galaxies in the rest-frame optical.

In the following chapter I will outline the conclusions drawn from these results on the subject of galaxy evolution. I will also discuss possible future work that can build upon the results of this thesis.

5.1 How do the sizes of galaxies evolve at $1 < z < 7$?

In Chapter 2, I present an analysis of galaxy size evolution from $z = 7$ in the GOODS-North and GOODS-South fields of the CANDELS survey, using the Petrosian radius as a measure of size. Firstly, I describe a new method of removing foreground objects from images of galaxies that makes use of the Lyman break at 912 Å, reducing the risk of contamination from extraneous objects when measuring properties of the galaxies within the sample. The size evolution is determined in the rest-frame optical ($\lambda \sim$ 4000 Å) where the availability of *HST* bands allows. I test to determine whether this difference in wavelength probed at higher redshifts affects the measured size. I use both a mass-selected sample where galaxies have a stellar mass in the range $10^9 M_\odot < M_* < 10^{10.5} M_\odot$, and a number density-selected sample where a constant number density of 1×10^{-4} Mpc^{-3} is used. The size is shown to increase from $z = 7$ to $z = 1$ for both samples. As the Petrosian radius is used as a measure of size, it is possible to probe not only whether the size grows, but where within the galaxy the size is changing. I find that on average, the outer radii increase the most rapidly, suggesting an inside-out formation process is causing the observed growth at $z > 3$.

I also explore how this inside-out formation occurs by examining the difference in size growth between a sample of mergers and non-mergers identified using the CAS parameters. The mergers are, on average, larger than non-mergers at all redshifts and the outer radii increase in size more rapidly than the inner radii for the mergers. This further supports the inside-out formation process which could occur by the accretion of satellite galaxies, mergers, and accretion of gas from the intergalactic medium.

5.2 How does galaxy surface brightness evolve since $z = 6$?

In Chapter 3, I investigate the evolution of galaxy surface brightness in the rest-frame UV ($\lambda \sim 2000$ Å) in the redshift range $1 < z < 6$ and explore its relation with star formation. I also explore how surface brightness affects how well we are able to detect galaxies at high redshifts. Previous work has only probed low redshift galaxies, but with images from CANDELS it is possible to measure the surface brightness of galaxies out to $z = 6$. I select two samples; one with galaxies with stellar mass $10^{10} < M_*/M_\odot < 10^{11}$ and one with a constant number density of 1×10^{-4} Mpc^{-3} across all redshift bins.

I find that galaxies at the highest redshifts are intrinsically brighter than those at the lowest redshifts, with an evolution of the form $(1 + z)^{-\alpha}$ where $\alpha = 0.18 \pm 0.01$ for the mass-selected sample and $\alpha = 0.19 \pm 0.01$ for the number density-selected sample. A number of factors that could be contributing to such an evolution are considered. For example, in Chapter 2, I show that size evolves such that galaxies get larger with cosmic time. I test to determine whether this observed size evolution is causing this surface brightness evolution by setting the size of all galaxies to the mean size of galaxies at $z = 6$ and recalculating the surface brightness. I find that the evolution is not significantly altered by this, suggesting size evolution is not the primary cause of the surface brightness evolution. I also examine the effect of dust but find that it only contributes to a small amount of evolution for both samples.

The star formation rate density is shown to decrease with time but as with dust and size, the change does not entirely explain the surface brightness evolution. I conclude that the remainder of the evolution is due to an observational bias and therefore massive, high redshift galaxies are missing from observations.

Galaxy stellar mass is a known cause of differences in galaxy evolution and so I explore its relationship with intrinsic surface brightness. I find that the intrinsic surface brightness does not significantly depend on the stellar mass at all redshifts, suggesting that the two parameters do not correlate with each other. It also suggests that the selection in the UV does not give mass completeness at any mass. This is further explored by artificially redshifting a sample of galaxies from $z = 2$ to $z = 6$ and measuring their surface brightness. I find that the surface brightness of the redshifted galaxies is much lower than that of the real galaxies at the same redshift. Using a signal-to-noise cut, I find the fraction of detectable galaxies is much lower in the redshifted sample than the real sample, highlighting the fact that a significant number of galaxies are missing from high redshift observations.

Finally, I find that for the mass-selected sample at low redshift, the star formation rate and specific star formation rate depends strongly on the surface brightness. However, at high redshifts this relationship weakens. For the number density-selected sample, this relationship remains roughly constant with redshift.

5.3 How does galaxy structure change at $0.5 < z < 3$?

Chapter 4 focuses on a non-parametric method of quantifying galaxy structural evolution. It also explores the role of galaxy mergers in galaxy evolution. I present the analysis of the morphological and structural evolution of a mass-selected sample of galaxies from $z \sim 0$ to $z \sim 3$ in all five CANDELS fields in the rest-frame optical ($\lambda \sim 4000$ Å). In order to determine timescales for merging events, I make use of IllustrisTNG simulations of galaxy mergers.

I find that the distribution of galaxies on a concentration-asymmetry plane up to $z \sim 3$ is comparable to that at lower redshifts. There is a continuum of parameters, implying

that the galaxies evolve continuously with regards to this relation. For the sample of galaxies under consideration, I find that both the concentration and asymmetry decrease with decreasing redshift. This finding suggests that the assembly of galaxies occur in such a way that the inner regions are grow faster than the outer regions at these redshifts.

By using simulations of galaxy merging events within the Illustris TNG300 simulations, it is possible to determine the timescale of such events. For the CAS system of identifying mergers, I find that the mean merger timescale is $0.56^{+0.23}_{-0.18}$ Gyr. This timescale does not vary with redshift, unlike the timescale for mergers identified using pair statistics. This timescale can be used in conjunction with the calculated merger fraction to determine the merger rate. This merger rate is in good agreement with merger rates determined using different methods such as pair statistics and Deep Learning, giving a consistent merger history for three different methods of identifying mergers.

5.4 Future Work

This thesis takes advantage of *HST* to probe galaxy evolution at high redshifts in the context of size, surface brightness, and structure. However, despite the high quality of CANDELS and *HST*, newer, and more advanced technology such as the *James Webb Space Telescope* and Euclid is required to build upon the work presented in this thesis.

The *James Webb Space Telescope* is a state-of-the-art infrared observatory that will make it possible to look further than ever before and will answer some of the unanswered questions about galaxy formation and evolution with both photometric and spectroscopic data of extremely high quality. The Near Infrared Camera (NIRCam) and the Mid-Infrared Instrument (MIRI) will provide photometric observations in the wavelength range 0.5-28 μm. The Near Infrared Spectrograph (NIRSpec) and the Near Infrared Imager and Slitless Spectrograph (NIRISS) will provide spectroscopic

observations of unprecedented quality in the wavelength range 0.6-5 μm. Observations made with these instruments will enable the detection of the redshifted light from the most distant galaxies and enable the determination of how they formed, giving a better understanding of how the galaxies seen today were established. Planned surveys such as PRIMER: Public Release IMaging for Extragalactic Research will provide deep imaging using the NIRCam and MIRI instruments across 10 bands. It will enable the detection of distant galaxies out to $z \sim 12$, of which a predicted ~70% will be new detections. This will allow the determination of the evolution of various parameters across a wide range of redshifts, in consistent rest-frames.

Euclid is a space observatory that aims to explore the last 10 billion years of the Universe by examining the properties of dark energy, dark matter, and gravity. It will also allow further insight into the initial conditions of the Universe, giving a better understanding of the underlying causes of structure formation. Euclid will have two instruments on board that will allow observation in both the optical and infrared; the visible imager (VIS), observing in the wavelength range 0.55-0.9 μm in a single broadband filter, and the near infrared spectrometer and photometer (NISP), observing in the wavelength range 0.9-2 μm in three broadband filters. These instruments are key to measure the redshifts and shapes of distant galaxies.

Whilst *HST* is able to detect galaxies out to $z \sim 10$, it isn't without its limitations; the detections of the highest redshift galaxies within the CANDELS survey are only available in the reddest filter, H_{160}. NIRCam will give the opportunity to confirm these uncertain detections and push to even higher redshifts due to the longer wavelengths probed. The longer wavelengths reached by *JWST* will enable detections of galaxies in the optical rest-frame at higher wavelengths than currently available. Whilst I show that a galaxy's size does not depend on the observed wavelength to first order in Chapter 2, by measuring the size in a consistent rest-frame wavelength, the measurements will be

more robust and it will be possible to confirm the size evolution observed.

I show that a significant number of galaxies are missing from the highest redshift observations in Chapter 3. The large mirror and sensitivity to lower brightness galaxies of *JWST* will allow the detection of these distant galaxies. This will provide an opportunity to determine whether the evolution in surface brightness found is real and not due to missing the lowest surface brightness galaxies at high redshifts. By observing in longer wavelengths, such a study of surface brightness can be extended further back in time to the highest redshifts.

With *HST*, it is only possible to probe the optical rest-frame up to $z \sim 3$. Morphologies are significantly different at different wavelengths so it is crucial to observe in a consistent wavelength in order to extend the study of quantitative structure to higher redshifts to avoid any biases. At lower redshifts, *JWST* will be able to look at lower mass galaxies which will help to gain a fuller and more comprehensive understanding of structure and, by extension, galaxy merger history. Euclid aims to cover an area of 15,000 deg^2 which will provide much larger samples of galaxies than currently available, giving better and more detailed estimates of merger histories.

These new surveys and observatories will produce an extremely large amount of data and expanding sample sizes to billions of galaxies will require new ways of analysing the data due to constraints such as computational resources and time required to process data. Machine learning techniques such as convolutional neural networks are significantly more efficient than existing algorithms. Supervised machine learning is suitable for this new era of 'big data' as it would take humans a significant amount of time to classify every image by eye, but with a trained network, it is possible to classify galaxies in a short time. Once a network is trained, it can be applied to other datasets, further expanding sample sizes. Human classification methods have a risk of being biased and unsupervised machine learning methods can remove such biases and therefore improve

classifications. As such the analysis of both qualitative and quantitative measures of galaxy morphology will benefit from these new methods.

We are on the brink of some incredible discoveries with these new, state-of-the-art observatories, and in the near future it will be possible to further extend our understanding of the formation and evolution of galaxies and the Universe as a whole.

Bibliography

Abraham R.G., van den Bergh S., Glazebrook K. et al., 1996. *The Morphologies of Distant Galaxies. II. Classifications from the Hubble Space Telescope Medium Deep Survey*. ApJS, 107, 1.

Alam S., Ata M., Bailey S. et al., 2017. *The clustering of galaxies in the completed SDSS-III Baryon Oscillation Spectroscopic Survey: cosmological analysis of the DR12 galaxy sample*. MNRAS, 470, 3, 2617–2652.

Allen R.J., Kacprzak G.G., Glazebrook K. et al., 2017. *The Size Evolution of Star-forming Galaxies since $z \sim 7$ Using ZFOURGE*. ApJL, 834, L11.

Almosallam I.A., Jarvis M.J. & Roberts S.J., 2016. *GPZ: non-stationary sparse Gaussian processes for heteroscedastic uncertainty estimation in photometric redshifts*. MNRAS, 462, 1, 726–739.

Arnouts S., Schiminovich D., Ilbert O. et al., 2005. *The GALEX VIMOS-VLT Deep Survey Measurement of the Evolution of the 1500 Å Luminosity Function*. ApJ, 619, 1, L43–L46.

Barden M., Rix H.W., Somerville R.S. et al., 2005. *GEMS: The Surface Brightness and Surface Mass Density Evolution of Disk Galaxies*. ApJ, 635, 959–981.

Bennett C.L., Halpern M., Hinshaw G. et al., 2003. *First-Year Wilkinson Microwave Anisotropy Probe (WMAP) Observations: Preliminary Maps and Basic Results*. ApJS, 148, 1, 1–27.

Bershady M.A., Jangren A. & Conselice C.J., 2000. *Structural and Photometric Classification of Galaxies. I. Calibration Based on a Nearby Galaxy Sample*. AJ, 119, 2645–2663.

Bertin E. & Arnouts S., 1996. *SExtractor: Software for source extraction.* A&AS, 117, 393–404.

Beutler F., Blake C., Colless M. et al., 2011. *The 6dF Galaxy Survey: baryon acoustic oscillations and the local Hubble constant*. MNRAS, 416, 4, 3017–3032.

Bhatawdekar R., Conselice C.J., Margalef-Bentabol B. et al., 2019. *Evolution of the galaxy stellar mass functions and UV luminosity functions at $z = 6$-9 in the Hubble Frontier Fields*. MNRAS, 486, 3, 3805–3830.

Bluck A.F.L., Conselice C.J., Bouwens R.J. et al., 2009. *A surprisingly high pair fraction for extremely massive galaxies at $z \sim 3$ in the GOODS NICMOS survey*. MNRAS, 394, 1, L51–L55.

Bluck A.F.L., Conselice C.J., Buitrago F. et al., 2012. *The Structures and Total (Minor + Major) Merger Histories of Massive Galaxies up to $z \sim 3$ in the HST GOODS NICMOS Survey: A Possible Solution to the Size Evolution Problem*. ApJ, 747, 34.

Bouwens R. & Silk J., 2002. *Models of Disk Evolution: Confrontation with Observations*. ApJ, 568, 2, 522–538.

Bouwens R.J., Illingworth G.D., Blakeslee J.P. et al., 2004. *Galaxy Size Evolution at High Redshift and Surface Brightness Selection Effects: Constraints from the Hubble Ultra Deep Field*. ApJL, 611, L1–L4.

Bouwens R.J., Illingworth G.D., Blakeslee J.P. et al., 2006. *Galaxies at z ~ 6: The UV Luminosity Function and Luminosity Density from 506 HUDF, HUDF Parallel ACS Field, and GOODS i-Dropouts*. ApJ, 653, 1, 53–85.

Bouwens R.J., Illingworth G.D., Franx M. et al., 2009. *UV Continuum Slope and Dust Obscuration from z ~ 6 to z ~ 2: The Star Formation Rate Density at High Redshift*. ApJ, 705, 1, 936–961.

Bouwens R.J., Illingworth G.D., González V. et al., 2010. *z ~ 7 Galaxy Candidates from NICMOS Observations Over the HDF-South and the CDF-South and HDF-North Goods Fields*. ApJ, 725, 2, 1587–1599.

Bouwens R.J., Illingworth G.D., Oesch P.A. et al., 2012. *Lower-luminosity Galaxies Could Reionize the Universe: Very Steep Faint-end Slopes to the UV Luminosity Functions at z >= 5-8 from the HUDF09 WFC3/IR Observations*. ApJ, 752, 1, L5.

Bouwens R.J., Illingworth G.D., Oesch P.A. et al., 2015. *UV Luminosity Functions at Redshifts z ~ 4 to z ~ 10: 10,000 Galaxies from HST Legacy Fields*. ApJ, 803, 1, 34.

Bouwens R.J., Illingworth G.D., Rosati P. et al., 2003. *Star Formation at z~6: i-Dropouts in the Advanced Camera for Surveys Guaranteed Time Observation Fields*. ApJ, 595, 2, 589–602.

Brammer G.B., van Dokkum P.G. & Coppi P., 2008. *EAZY: A Fast, Public Photometric Redshift Code*. ApJ, 686, 1503–1513.

Bruce V.A., Dunlop J.S., Cirasuolo M. et al., 2012. *The morphologies of massive galaxies at 1 < z < 3 in the CANDELS-UDS field: compact bulges, and the rise and fall of massive discs*. MNRAS, 427, 2, 1666–1701.

Bruce V.A., Dunlop J.S., McLure R.J. et al., 2014. *The bulge-disc decomposed evolution of massive galaxies at 1 < z < 3 in CANDELS*. MNRAS, 444, 2, 1001–1033.

Bruzual G. & Charlot S., 2003. *Stellar population synthesis at the resolution of 2003*. MNRAS, 344, 1000–1028.

Buitrago F., Trujillo I., Conselice C.J. et al., 2008. *Size Evolution of the Most Massive Galaxies at 1.7 < z < 3 from GOODS NICMOS Survey Imaging*. ApJL, 687, L61.

Buitrago F., Trujillo I., Conselice C.J. et al., 2013. *Early-type galaxies have been the predominant morphological class for massive galaxies since only z ∼ 1*. MNRAS, 428, 1460–1478.

Buitrago F., Trujillo I., Curtis-Lake E. et al., 2017. *The cosmic assembly of stellar haloes in massive early-type Galaxies*. MNRAS, 466, 4, 4888–4903.

Bundy K., Fukugita M., Ellis R.S. et al., 2009. *The Greater Impact of Mergers on the Growth of Massive Galaxies: Implications for Mass Assembly and Evolution since z ∼ 1*. ApJ, 697, 2, 1369–1383.

Bunker A.J., Stanway E.R., Ellis R.S. et al., 2003. *A star-forming galaxy at z= 5.78 in the Chandra Deep Field South*. MNRAS, 342, 3, L47–L51.

Burles S., Nollett K.M. & Turner M.S., 2001. *Big Bang Nucleosynthesis Predictions for Precision Cosmology*. ApJ, 552, 1, L1–L5.

Camps P. & Baes M., 2015. *SKIRT: An advanced dust radiative transfer code with a user-friendly architecture*. Astronomy and Computing, 9, 20–33.

Camps P. & Baes M., 2020. *SKIRT 9: Redesigning an advanced dust radiative transfer code to allow kinematics, line transfer and polarization by aligned dust grains*. Astronomy and Computing, 31. ISSN 22131337.

Camps P., Trayford J.W., Baes M. et al., 2016. *Far-infrared and dust properties of present-day galaxies in the EAGLE simulations*. MNRAS, 462, 1, 1057–1075.

Carrasco E.R., Conselice C.J. & Trujillo I., 2010. *Gemini K-band NIRI Adaptive Optics Observations of massive galaxies at 1 < z < 2*. MNRAS, 405, 2253–2259.

Casertano S., de Mello D., Dickinson M. et al., 2000. *WFPC2 Observations of the Hubble Deep Field South*. AJ, 120, 6, 2747–2824.

Cassata P., Giavalisco M., Guo Y. et al., 2010. *The Morphology of Passively Evolving Galaxies at z ∼ 2 from Hubble Space Telescope/WFC3 Deep Imaging in the Hubble Ultra Deep Field*. ApJL, 714, L79–L83.

Cassata P., Giavalisco M., Williams C.C. et al., 2013. *Constraining the Assembly of Normal and Compact Passively Evolving Galaxies from Redshift z = 3 to the Present with CANDELS*. ApJ, 775, 106.

Casteels K.R.V., Conselice C.J., Bamford S.P. et al., 2014. *Galaxy And Mass Assembly (GAMA): refining the local galaxy merger rate using morphological information*. MNRAS, 445, 2, 1157–1169.

Chabrier G., 2003. *Galactic Stellar and Substellar Initial Mass Function*. PASP, 115, 809, 763–795.

Cheng T.Y., Conselice C.J., Aragón-Salamanca A. et al., 2020. *Optimizing automatic morphological classification of galaxies with machine learning and deep learning using Dark Energy Survey imaging*. MNRAS, 493, 3, 4209–4228.

Cimatti A., Cassata P., Pozzetti L. et al., 2008. *GMASS ultradeep spectroscopy of galaxies at z ∼ 2. II. Superdense passive galaxies: how did they form and evolve?* A&A, 482, 21–42.

Cole S., Lacey C.G., Baugh C.M. et al., 2000. *Hierarchical galaxy formation*. MNRAS, 319, 1, 168–204.

Conselice C.J., 2003. *The Relationship between Stellar Light Distributions of Galaxies and Their Formation Histories*. ApJS, 147, 1–28.

Conselice C.J., 2006. *Early and Rapid Merging as a Formation Mechanism of Massive Galaxies: Empirical Constraints*. ApJ, 638, 686–702.

Conselice C.J., 2014. *The Evolution of Galaxy Structure Over Cosmic Time*. ARA&A, 52, 291–337.

Conselice C.J. & Arnold J., 2009. *The structures of distant galaxies - II. Diverse galaxy structures and local environments at z = 4-6 implications for early galaxy assembly*. MNRAS, 397, 208–231.

Conselice C.J., Bershady M.A., Dickinson M. et al., 2003. *A Direct Measurement of Major Galaxy Mergers at z<∼3*. AJ, 126, 3, 1183–1207.

Conselice C.J., Bershady M.A. & Gallagher J. S. I., 2000a. *Physical morphology and triggers of starburst galaxies*. A&A, 354, L21–L24.

Conselice C.J., Bershady M.A. & Jangren A., 2000b. *The Asymmetry of Galaxies: Physical Morphology for Nearby and High-Redshift Galaxies*. ApJ, 529, 2, 886–910.

Conselice C.J., Blackburne J.A. & Papovich C., 2005. *The Luminosity, Stellar Mass, and Number Density Evolution of Field Galaxies of Known Morphology from z = 0.5 to 3*. ApJ, 620, 564–583.

Conselice C.J., Bluck A.F.L., Buitrago F. et al., 2011a. *The Hubble Space Telescope GOODS NICMOS Survey: overview and the evolution of massive galaxies at 1.5 < z < 3*. MNRAS, 413, 80–100.

Conselice C.J., Bluck A.F.L., Ravindranath S. et al., 2011b. *The tumultuous formation of*

the Hubble sequence at $z > 1$ examined with HST/Wide-Field Camera-3 observations of the Hubble Ultra Deep Field. MNRAS, 417, 4, 2770–2788.

Conselice C.J., Gallagher John S. I. & Wyse R.F.G., 2002. *Galaxy Populations and Evolution in Clusters. II. Defining Cluster Populations*. AJ, 123, 5, 2246–2260.

Conselice C.J., Mortlock A., Bluck A.F.L. et al., 2013. *Gas accretion as a dominant formation mode in massive galaxies from the GOODS NICMOS Survey*. MNRAS, 430, 1051–1060.

Conselice C.J., Rajgor S. & Myers R., 2008. *The structures of distant galaxies - I. Galaxy structures and the merger rate to $z \sim 3$ in the Hubble Ultra-Deep Field*. MNRAS, 386, 2, 909–927.

Conselice C.J., Wilkinson A., Duncan K. et al., 2016. *The Evolution of Galaxy Number Density at $z < 8$ and Its Implications*. ApJ, 830, 2, 83.

Crain R.A., Schaye J., Bower R.G. et al., 2015. *The EAGLE simulations of galaxy formation: calibration of subgrid physics and model variations*. MNRAS, 450, 2, 1937–1961.

Curtis-Lake E., McLure R.J., Dunlop J.S. et al., 2016. *Non-parametric analysis of the rest-frame UV sizes and morphological disturbance amongst L_* galaxies at $4 < z < 8$*. MNRAS, 457, 440–464.

Daddi E., Renzini A., Pirzkal N. et al., 2005. *Passively Evolving Early-Type Galaxies at $1.4 \lesssim z \lesssim 2.5$ in the Hubble Ultra Deep Field*. ApJ, 626, 680–697.

Damjanov I., McCarthy P.J., Abraham R.G. et al., 2009. *Red Nuggets at $z \sim 1.5$: Compact Passive Galaxies and the Formation of the Kormendy Relation*. ApJ, 695, 101–115.

Davis M., Guhathakurta P., Konidaris N.P. et al., 2007. *The All-Wavelength Extended Groth Strip International Survey (AEGIS) Data Sets*. ApJ, 660, 1, L1–L6.

de Albernaz Ferreira L. & Ferrari F., 2018. *The impact of redshift on galaxy morphometric classification: case studies for SDSS, DES, LSST and HST with MORFOMETRYKA*. MNRAS, 473, 2, 2701–2713.

de Vaucouleurs G., 1959. *Classification and Morphology of External Galaxies.* Handbuch der Physik, 53, 275.

Duncan K., Conselice C.J., Mortlock A. et al., 2014. *The mass evolution of the first galaxies: stellar mass functions and star formation rates at $4 < z < 7$ in the CANDELS GOODS-South field*. MNRAS, 444, 2960–2984.

Duncan K., Conselice C.J., Mundy C. et al., 2019. *Observational Constraints on the Merger History of Galaxies since $z \approx 6$: Probabilistic Galaxy Pair Counts in the CANDELS Fields*. ApJ, 876, 2, 110.

Fan L., Lapi A., De Zotti G. et al., 2008. *The Dramatic Size Evolution of Elliptical Galaxies and the Quasar Feedback*. ApJL, 689, L101.

Fan X., Carilli C.L. & Keating B., 2006. *Observational Constraints on Cosmic Reionization*. ARA&A, 44, 1, 415–462.

Ferguson H.C., Dickinson M., Giavalisco M. et al., 2004. *The Size Evolution of High-Redshift Galaxies*. ApJL, 600, L107–L110.

Ferguson H.C., Dickinson M. & Williams R., 2000. *The Hubble Deep Fields*. ARA&A, 38, 667–715.

Ferrari F., de Carvalho R.R. & Trevisan M., 2015. *Morfometryka—A New Way of Establishing Morphological Classification of Galaxies*. ApJ, 814, 1, 55.

Ferreira L., Conselice C.J., Duncan K. et al., 2020. *Galaxy Merger Rates up to z ∼ 3 Using a Bayesian Deep Learning Model: A Major-merger Classifier Using IllustrisTNG Simulation Data*. ApJ, 895, 2, 115.

Ferreras I., Lisker T., Pasquali A. et al., 2009. *On the formation of massive galaxies: a simultaneous study of number density, size and intrinsic colour evolution in GOODS*. MNRAS, 396, 3, 1573–1578.

Ferreras I., Trujillo I., Mármol-Queraltó E. et al., 2014. *Constraints on the merging channel of massive galaxies since z ∼ 1*. MNRAS, 444, 1, 906–918.

Finkelstein S.L., Papovich C., Giavalisco M. et al., 2010. *On the Stellar Populations and Evolution of Star-forming Galaxies at 6.3 < z <= 8.6*. ApJ, 719, 2, 1250–1273.

Freundlich J., Combes F., Tacconi L.J. et al., 2013. *Towards a resolved Kennicutt-Schmidt law at high redshift*. A&A, 553, A130.

Furlong M., Bower R.G., Crain R.A. et al., 2017. *Size evolution of normal and compact galaxies in the EAGLE simulation*. MNRAS, 465, 722–738.

Gavazzi G., Fumagalli M., Cucciati O. et al., 2010. *A snapshot on galaxy evolution occurring in the Great Wall: the role of Nurture at z = 0*. A&A, 517, A73.

Genel S., Nelson D., Pillepich A. et al., 2018. *The size evolution of star-forming and quenched galaxies in the IllustrisTNG simulation*. MNRAS, 474, 3, 3976–3996.

Giavalisco M., Dickinson M., Ferguson H.C. et al., 2004. *The Rest-Frame Ultraviolet Luminosity Density of Star-forming Galaxies at Redshifts z > 3.5*. ApJL, 600, L103–L106.

Giavalisco M., Steidel C.C. & Macchetto F.D., 1996. *Hubble Space Telescope Imaging of Star-forming Galaxies at Redshifts z > 3*. ApJ, 470, 189.

González Delgado R.M., Pérez E., Cid Fernand es R. et al., 2017. *Spatially-resolved star formation histories of CALIFA galaxies. Implications for galaxy formation*. A&A, 607, A128.

Grogin N.A., Kocevski D.D., Faber S.M. et al., 2011. *CANDELS: The Cosmic Assembly Near-infrared Deep Extragalactic Legacy Survey*. ApJS, 197, 35.

Guhathakurta P., Tyson J.A. & Majewski S.R., 1990. *A Redshift Limit for the Faint Blue Galaxy Population from Deep U Band Imaging*. ApJL, 357, L9.

Gunn J.E. & Gott J. Richard I., 1972. *On the Infall of Matter Into Clusters of Galaxies and Some Effects on Their Evolution*. ApJ, 176, 1.

Gunn J.E. & Peterson B.A., 1965. *On the Density of Neutral Hydrogen in Intergalactic Space.* ApJ, 142, 1633–1636.

Holwerda B.W., Bouwens R., Oesch P. et al., 2015. *The Sizes of Candidate z∼9-10 Galaxies: Confirmation of the Bright CANDELS Sample and Relation with Luminosity and Mass.* ApJ, 808, 6.

Hopkins A.M. & Beacom J.F., 2006. *On the Normalization of the Cosmic Star Formation History*. ApJ, 651, 1, 142–154.

Hubble E.P., 1926. *Extragalactic nebulae.* ApJ, 64, 321–369.

Huertas-Company M., Bernardi M., Pérez-González P.G. et al., 2016a. *Mass assembly and morphological transformations since z ∼ 3 from CANDELS*. MNRAS, 462, 4495–4516.

Huertas-Company M., Bernardi M., Pérez-González P.G. et al., 2016b. *Mass assembly and morphological transformations since z ~ 3 from CANDELS*. MNRAS, 462, 4, 4495–4516.

Huertas-Company M., Rodriguez-Gomez V., Nelson D. et al., 2019. *The Hubble Sequence at z ∼ 0 in the IllustrisTNG simulation with deep learning*. MNRAS, 489, 2, 1859–1879.

Ichikawa T., Kajisawa M. & Akhlaghi M., 2012. *A universal stellar mass-size relation of galaxies in the GOODS-North region*. MNRAS, 422, 2, 1014–1027.

Jonsson P., 2006. *SUNRISE: polychromatic dust radiative transfer in arbitrary geometries*. MNRAS, 372, 1, 2–20.

Kartaltepe J.S., Mozena M., Kocevski D. et al., 2015. *CANDELS Visual Classifications: Scheme, Data Release, and First Results*. ApJS, 221, 1, 11.

Kashikawa N., Takata T., Ohyama Y. et al., 2003. *Subaru Deep Survey. III. Evolution of Rest-Frame Luminosity Functions Based on the Photometric Redshifts for a K'-Band-Selected Galaxy Sample*. AJ, 125, 1, 53–65.

Kennicutt Robert C. J., 1998. *The Global Schmidt Law in Star-forming Galaxies*. ApJ, 498, 2, 541–552.

Kent S.M., 1985. *CCD surface photometry of field galaxies. II. Bulge/disk decompositions.* ApJS, 59, 115–159.

Koekemoer A.M., Faber S.M., Ferguson H.C. et al., 2011. *CANDELS: The Cosmic Assembly Near-infrared Deep Extragalactic Legacy Survey—The Hubble Space Telescope Observations, Imaging Data Products, and Mosaics*. ApJS, 197, 36.

Kron R.G., 1995. *Evolution in the Galaxy Population*, page 204.

Kulkarni G., Choudhury T.R., Puchwein E. et al., 2017. *Large 21-cm signals from AGN-dominated reionization*. MNRAS, 469, 4, 4283–4291.

Labbé I., Rudnick G., Franx M. et al., 2003. *Large Disklike Galaxies at High Redshift*. ApJL, 591, 2, L95–L98.

Lani C., Almaini O., Hartley W.G. et al., 2013. *Evidence for a correlation between the sizes of quiescent galaxies and local environment to $z \sim 2$*. MNRAS, 435, 207–221.

Larson R.B., Tinsley B.M. & Caldwell C.N., 1980. *The evolution of disk galaxies and the origin of S0 galaxies*. ApJ, 237, 692–707.

Law D.R., Steidel C.C., Erb D.K. et al., 2007. *The Physical Nature of Rest-UV Galaxy Morphology during the Peak Epoch of Galaxy Formation*. ApJ, 656, 1, 1–26.

Lawrence A., Warren S.J., Almaini O. et al., 2007. *The UKIRT Infrared Deep Sky Survey (UKIDSS)*. MNRAS, 379, 4, 1599–1617.

Lehnert M.D. & Bremer M., 2003. *Luminous Lyman Break Galaxies at $z > 5$ and the Source of Reionization*. ApJ, 593, 2, 630–639.

Leroy A.K., Walter F., Brinks E. et al., 2008. *The Star Formation Efficiency in Nearby Galaxies: Measuring Where Gas Forms Stars Effectively*. AJ, 136, 6, 2782–2845.

Lilly S., Schade D., Ellis R. et al., 1998. *Hubble Space Telescope Imaging of the CFRS and LDSS Redshift Surveys. II. Structural Parameters and the Evolution of disk Galaxies to $z \sim 1$*[1]. ApJ, 500, 1, 75–94.

Lintott C., Schawinski K., Bamford S. et al., 2011. *Galaxy Zoo 1: data release of morphological classifications for nearly 900 000 galaxies*. MNRAS, 410, 1, 166–178.

Lintott C.J., Schawinski K., Slosar A. et al., 2008. *Galaxy Zoo: morphologies derived from visual inspection of galaxies from the Sloan Digital Sky Survey*. MNRAS, 389, 3, 1179–1189.

López-Sanjuan C., Balcells M., Pérez-González P.G. et al., 2009. *The galaxy major merger fraction to {z} 1.* A&A, 501, 2, 505–518.

López-Sanjuan C., Le Fèvre O., Ilbert O. et al., 2012. *The dominant role of mergers in the size evolution of massive early-type galaxies since z ∼ 1.* A&A, 548, A7.

Lotz J.M., Jonsson P., Cox T.J. et al., 2008. *Galaxy merger morphologies and time-scales from simulations of equal-mass gas-rich disc mergers.* MNRAS, 391, 1137–1162.

Lotz J.M., Jonsson P., Cox T.J. et al., 2010. *The effect of gas fraction on the morphology and time-scales of disc galaxy mergers.* MNRAS, 404, 2, 590–603.

Lotz J.M., Jonsson P., Cox T.J. et al., 2011. *The Major and Minor Galaxy Merger Rates at z < 1.5.* ApJ, 742, 2, 103.

Lotz J.M., Primack J. & Madau P., 2004. *A New Nonparametric Approach to Galaxy Morphological Classification.* AJ, 128, 1, 163–182.

Madau P. & Dickinson M., 2014. *Cosmic Star-Formation History.* ARA&A, 52, 415–486.

Madau P., Ferguson H.C., Dickinson M.E. et al., 1996. *High-redshift galaxies in the Hubble Deep Field: colour selection and star formation history to z∼4.* MNRAS, 283, 4, 1388–1404.

Madau P., Pozzetti L. & Dickinson M., 1998. *The Star Formation History of Field Galaxies.* ApJ, 498, 1, 106–116.

Mager V.A., Conselice C.J., Seibert M. et al., 2018. *Galaxy Structure in the Ultraviolet: The Dependence of Morphological Parameters on Rest-frame Wavelength.* ApJ, 864, 2, 123.

Man A.W.S., Zirm A.W. & Toft S., 2016. *Resolving the Discrepancy of Galaxy Merger Fraction Measurements at z ~ 0-3*. ApJ, 830, 2, 89.

Margalef-Bentabol B., Conselice C.J., Mortlock A. et al., 2016. *The formation of bulges, discs and two-component galaxies in the CANDELS Survey at z < 3*. MNRAS, 461, 2728–2746.

Margalef-Bentabol B., Conselice C.J., Mortlock A. et al., 2018. *Stellar populations, stellar masses and the formation of galaxy bulges and discs at z < 3 in CANDELS*. MNRAS, 473, 4, 5370–5384.

Marinacci F., Vogelsberger M., Pakmor R. et al., 2018. *First results from the IllustrisTNG simulations: radio haloes and magnetic fields*. MNRAS, 480, 4, 5113–5139.

Mather J.C., Cheng E.S., Eplee R. E. J. et al., 1990. *A Preliminary Measurement of the Cosmic Microwave Background Spectrum by the Cosmic Background Explorer (COBE) Satellite*. ApJ, 354, L37.

McLure R.J., Cirasuolo M., Dunlop J.S. et al., 2009. *The luminosity function, halo masses and stellar masses of luminous Lyman-break galaxies at redshifts 5 < z < 6*. MNRAS, 395, 4, 2196–2209.

McLure R.J., Dunlop J.S., Bowler R.A.A. et al., 2013. *A new multifield determination of the galaxy luminosity function at z = 7-9 incorporating the 2012 Hubble Ultra-Deep Field imaging*. MNRAS, 432, 4, 2696–2716.

McLure R.J., Dunlop J.S., Cullen F. et al., 2018. *Dust attenuation in 2 < z < 3 star-forming galaxies from deep ALMA observations of the Hubble Ultra Deep Field*. MNRAS, 476, 3, 3991–4006.

Meurer G.R., Heckman T.M. & Calzetti D., 1999. *Dust Absorption and the Ultraviolet*

Luminosity Density at $z \sim 3$ as Calibrated by Local Starburst Galaxies. ApJ, 521, 1, 64–80.

Miller T.B., van Dokkum P., Mowla L. et al., 2019. *A New View of the Size–Mass Distribution of Galaxies: Using r_{20} and r_{80} Instead of r_{50}*. ApJL, 872, L14.

Miralda-Escudé J., 2003. *The Dark Age of the Universe*. Science, 300, 5627, 1904–1909.

Moore B., Katz N., Lake G. et al., 1996. *Galaxy harassment and the evolution of clusters of galaxies*. Nature, 379, 6566, 613–616.

Mortlock A., Conselice C.J., Hartley W.G. et al., 2013. *The redshift and mass dependence on the formation of the Hubble sequence at $z > 1$ from CANDELS/UDS*. MNRAS, 433, 2, 1185–1201.

Mosleh M., Williams R.J., Franx M. et al., 2012. *The Evolution of Mass-Size Relation for Lyman Break Galaxies from $z = 1$ to $z = 7$*. ApJ, 756, 1, L12.

Mundy C.J., Conselice C.J., Duncan K.J. et al., 2017. *A consistent measure of the merger histories of massive galaxies using close-pair statistics - I. Major mergers at $z < 3.5$*. MNRAS, 470, 3, 3507–3531.

Mundy C.J., Conselice C.J. & Ownsworth J.R., 2015. *Tracing galaxy populations through cosmic time: a critical test of methods for connecting the same galaxies between different redshifts at $z < 3$*. MNRAS, 450, 3696–3707.

Naab T., Johansson P.H. & Ostriker J.P., 2009. *Minor Mergers and the Size Evolution of Elliptical Galaxies*. ApJL, 699, L178–L182.

Naiman J.P., Pillepich A., Springel V. et al., 2018. *First results from the IllustrisTNG simulations: a tale of two elements - chemical evolution of magnesium and europium*. MNRAS, 477, 1, 1206–1224.

Nelson D., Pillepich A., Springel V. et al., 2018. *First results from the IllustrisTNG simulations: the galaxy colour bimodality*. MNRAS, 475, 1, 624–647.

Nelson D., Pillepich A., Springel V. et al., 2019. *First results from the TNG50 simulation: galactic outflows driven by supernovae and black hole feedback*. MNRAS, 490, 3, 3234–3261.

Nelson D., Springel V., Pillepich A. et al., 2019a. *The IllustrisTNG simulations: public data release*. Computational Astrophysics and Cosmology, 6, 1, 2. ISSN 2197-7909.

Nelson D., Springel V., Pillepich A. et al., 2019b. *The IllustrisTNG simulations: public data release*. Computational Astrophysics and Cosmology, 6, 1, 2. ISSN 2197-7909.

Nevin R., Blecha L., Comerford J. et al., 2019. *Accurate Identification of Galaxy Mergers with Imaging*. ApJ, 872, 1, 76.

Oesch P.A., Bouwens R.J., Carollo C.M. et al., 2010. *Structure and Morphologies of $z \sim 7$-8 Galaxies from Ultra-deep WFC3/IR Imaging of the Hubble Ultra-deep Field*. ApJL, 709, L21–L25.

Oesch P.A., Bouwens R.J., Illingworth G.D. et al., 2012. *The Bright End of the Ultraviolet Luminosity Function at $z \sim 8$: New Constraints from CANDELS Data in GOODS-South*. ApJ, 759, 2, 135.

Ono Y., Ouchi M., Curtis-Lake E. et al., 2013. *Evolution of the Sizes of Galaxies over $7 < z < 12$ Revealed by the 2012 Hubble Ultra Deep Field Campaign*. ApJ, 777, 155.

Ownsworth J.R., Conselice C.J., Mundy C.J. et al., 2016. *The evolution of galaxies at constant number density: a less biased view of star formation, quenching, and structural formation*. MNRAS, 461, 1112–1129.

Papovich C., Dickinson M., Giavalisco M. et al., 2005. *The Assembly of Diversity in the Morphologies and Stellar Populations of High-Redshift Galaxies*. ApJ, 631, 1, 101–120.

Papovich C., Finkelstein S.L., Ferguson H.C. et al., 2011. *The rising star formation histories of distant galaxies and implications for gas accretion with time*. MNRAS, 412, 1123–1136.

Papovich C., Giavalisco M., Dickinson M. et al., 2003. *The Internal Ultraviolet-Optical Color Dispersion: Quantifying the Morphological K-Correction*. ApJ, 598, 2, 827–847.

Partridge R.B. & Peebles P.J.E., 1967. *Are Young Galaxies Visible?* ApJ, 147, 868.

Patel S.G., van Dokkum P.G., Franx M. et al., 2013. *HST/WFC3 Confirmation of the Inside-out Growth of Massive Galaxies at $0 < z < 2$ and Identification of Their Star-forming Progenitors at $z \sim 3$*. ApJ, 766, 15.

Peebles P.J.E., 1968a. *Significance of the First Brightest Galaxies in Rich Clusters*. ApJ, 153, 13.

Peebles P.J.E., 1968b. *Significance of the First Brightest Galaxies in Rich Clusters*. ApJ, 153, 13.

Penzias A.A. & Wilson R.W., 1965. *A Measurement of Excess Antenna Temperature at 4080 Mc/s.* ApJ, 142, 419–421.

Petrosian V., 1976. *Surface brightness and evolution of galaxies*. ApJL, 209, L1–L5.

Pillepich A., Nelson D., Hernquist L. et al., 2018. *First results from the IllustrisTNG simulations: the stellar mass content of groups and clusters of galaxies*. MNRAS, 475, 1, 648–675.

Pillepich A., Nelson D., Springel V. et al., 2019. *First results from the TNG50 simulation: the evolution of stellar and gaseous discs across cosmic time*. MNRAS, 490, 3, 3196–3233.

Planck Collaboration, Ade P.A.R., Aghanim N. et al., 2014. *Planck 2013 results. I. Overview of products and scientific results*. A&A, 571, A1.

Planck Collaboration, Aghanim N., Akrami Y. et al., 2020. *Planck 2018 results. VI. Cosmological parameters*. A&A, 641, A6.

Ravindranath S., Ferguson H.C., Conselice C. et al., 2004. *The Evolution of Disk Galaxies in the GOODS-South Field: Number Densities and Size Distribution*. ApJ, 604, 1, L9–L12.

Ribeiro B., Le Fèvre O., Tasca L.A.M. et al., 2016. *Size evolution of star-forming galaxies with $2 < z < 4.5$ in the VIMOS Ultra-Deep Survey*. A&A, 593, A22.

Roberts M.S. & Haynes M.P., 1994. *Physical Parameters along the Hubble Sequence*. ARA&A, 32, 115–152.

Roche N., Ratnatunga K., Griffiths R.E. et al., 1998. *Galaxy surface brightness and size evolution to $z{\sim}4$*. MNRAS, 293, 2, 157–176.

Rodriguez-Gomez V., Genel S., Vogelsberger M. et al., 2015. *The merger rate of galaxies in the Illustris simulation: A comparison with observations and semi-empirical models*. Monthly Notices of the Royal Astronomical Society, 449, 1, 49–64. ISSN 13652966.

Sandage A., 1975. *Classification and Stellar Content of Galaxies Obtained from Direct Photography*, page 1.

Santini P., Ferguson H.C., Fontana A. et al., 2015. *Stellar Masses from the CANDELS Survey: The GOODS-South and UDS Fields*. ApJ, 801, 2, 97.

Schade D., Lilly S.J., Crampton D. et al., 1995. *Canada-France Redshift Survey: Hubble Space Telescope Imaging of High-Redshift Field Galaxies*. ApJL, 451, L1.

Schade D., Lilly S.J., Le Fevre O. et al., 1996. *Canada-France Redshift Survey. XI. Morphology of High-Redshift Field Galaxies from High-Resolution Ground-based Imaging*. ApJ, 464, 79.

Schaye J., Crain R.A., Bower R.G. et al., 2015. *The EAGLE project: simulating the evolution and assembly of galaxies and their environments*. MNRAS, 446, 1, 521–554.

Schechter P., 1976. *An analytic expression for the luminosity function for galaxies.* ApJ, 203, 297–306.

Schmidt M., 1959. *The Rate of Star Formation.* ApJ, 129, 243.

Schweizer F., 1982. *Colliding and merging galaxies. I. Evidence for the recent merging of two disk galaxies in NGC 7252.* ApJ, 252, 455–460.

Scolnic D.M., Jones D.O., Rest A. et al., 2018. *The Complete Light-curve Sample of Spectroscopically Confirmed SNe Ia from Pan-STARRS1 and Cosmological Constraints from the Combined Pantheon Sample*. ApJ, 859, 2, 101.

Scoville N., Aussel H., Brusa M. et al., 2007. *The Cosmic Evolution Survey (COSMOS): Overview*. ApJS, 172, 1, 1–8.

Shibuya T., Ouchi M. & Harikane Y., 2015. *Morphologies of ~190,000 Galaxies at z = 0-10 Revealed with HST Legacy Data. I. Size Evolution*. ApJS, 219, 15.

Simard L., Koo D.C., Faber S.M. et al., 1999. *The Magnitude-Size Relation of Galaxies out to z∼1*. ApJ, 519, 2, 563–579.

Snyder G.F., Lotz J.M., Rodriguez-Gomez V. et al., 2017. *Massive close pairs measure rapid galaxy assembly in mergers at high redshift*. MNRAS, 468, 1, 207–216.

Springel V., Pakmor R., Pillepich A. et al., 2018. *First results from the IllustrisTNG simulations: matter and galaxy clustering*. MNRAS, 475, 1, 676–698.

Springel V., White S.D.M., Jenkins A. et al., 2005. *Simulations of the formation, evolution and clustering of galaxies and quasars*. Nature, 435, 7042, 629–636.

Springel V., Yoshida N. & White S.D.M., 2001. *GADGET: a code for collisionless and gasdynamical cosmological simulations*. New Astron., 6, 2, 79–117.

Stanway E.R., Bunker A.J., McMahon R.G. et al., 2004a. *Hubble Space Telescope Imaging and Keck Spectroscopy of z ∼ 6 i-Band Dropout Galaxies in the Advanced Camera for Surveys GOODS Fields*. ApJ, 607, 2, 704–720.

Stanway E.R., Glazebrook K., Bunker A.J. et al., 2004b. *Three Lyα Emitters at z ∼ 6: Early GMOS/Gemini Data from the GLARE Project*. ApJ, 604, 1, L13–L16.

Steidel C.C., Adelberger K.L., Giavalisco M. et al., 1999. *Lyman-Break Galaxies at z>∼4 and the Evolution of the Ultraviolet Luminosity Density at High Redshift*. ApJ, 519, 1, 1–17.

Steidel C.C., Giavalisco M., Pettini M. et al., 1996. *Spectroscopic Confirmation of a Population of Normal Star-forming Galaxies at Redshifts z > 3*. ApJL, 462, L17.

Steidel C.C. & Hamilton D., 1992. *Deep Imaging of redshift QSO Fields Below the Lyman Limit. I. The Field of Q0000-263 and galaxies at Z= 3.4*. AJ, 104, 941.

Straatman C.M.S., Labbé I., Spitler L.R. et al., 2015. *The Sizes of Massive Quiescent and Star-forming Galaxies at z ∼ 4 with ZFOURGE and CANDELS*. ApJL, 808, L29.

Tacconi L.J., Neri R., Genzel R. et al., 2013. *Phibss: Molecular Gas Content and Scaling Relations in z ∼ 1-3 Massive, Main-sequence Star-forming Galaxies*. ApJ, 768, 1, 74.

Taylor-Mager V.A., Conselice C.J., Windhorst R.A. et al., 2007. *Dependence of Galaxy Structure on Rest-Frame Wavelength and Galaxy Type*. ApJ, 659, 1, 162–187.

Thomas R.M., Zaroubi S., Ciardi B. et al., 2009. *Fast large-scale reionization simulations*. MNRAS, 393, 1, 32–48.

Thompson R.I., 2003. *Star Formation History and Other Properties of the Northern Hubble Deep Field*. ApJ, 596, 2, 748–767.

Thompson R.I., Weymann R.J. & Storrie-Lombardi L.J., 2001. *Star Formation History in the NICMOS Northern Hubble Deep Field*. ApJ, 546, 2, 694–718.

Tohill C., Ferreira L., Conselice C.J. et al., 2021. *Measuring the structure of high-redshift galaxies with deep learning*. arXiv e-prints, arXiv:2012.09081.

Tolman R., 1934. *Relativity, Thermodynamics and Cosmology. (Scientific Books: Relativity, Thermodynamics and Cosmology)*. Science, 80, 358.

Tolman R.C., 1930. *On the Estimation of Distances in a Curved Universe with a Non-Static Line Element*. Proceedings of the National Academy of Science, 16, 511–520.

Toomre A. & Toomre J., 1972. *Galactic Bridges and Tails*. ApJ, 178, 623–666.

Trayford J.W., Camps P., Theuns T. et al., 2017. *Optical colours and spectral indices of z = 0.1 EAGLE galaxies with the 3D dust radiative transfer code SKIRT*. Monthly Notices of the Royal Astronomical Society, 470, 1, 771–799. ISSN 13652966.

Trujillo I. & Aguerri J.A.L., 2004. *Quantitative morphological analysis of the Hubble Deep Field North and Hubble Deep Field South - I. Early- and late-type luminosity-size relations of galaxies out to z∼ 1*. MNRAS, 355, 1, 82–96.

Trujillo I., Conselice C.J., Bundy K. et al., 2007. *Strong size evolution of the most massive galaxies since z ∼ 2*. MNRAS, 382, 109–120.

van den Bergh S., 1976. *A new classification system for galaxies.* ApJ, 206, 883–887.

van der Wel A., Franx M., van Dokkum P.G. et al., 2014. *3D-HST+CANDELS: The Evolution of the Galaxy Size-Mass Distribution since z = 3*. ApJ, 788, 28.

van der Wel A., Holden B.P., Zirm A.W. et al., 2008. *Recent Structural Evolution of Early-Type Galaxies: Size Growth from z = 1 to z = 0*. ApJ, 688, 48–58.

van Dokkum P.G., Franx M., Kriek M. et al., 2008. *Confirmation of the Remarkable Compactness of Massive Quiescent Galaxies at z ∼ 2.3: Early-Type Galaxies Did not Form in a Simple Monolithic Collapse*. ApJL, 677, L5.

van Dokkum P.G., Whitaker K.E., Brammer G. et al., 2010. *The Growth of Massive Galaxies Since z = 2*. ApJ, 709, 1018–1041.

Ventou E., Contini T., Bouché N. et al., 2019. *New criteria for the selection of galaxy close pairs from cosmological simulations: evolution of the major and minor merger fraction in MUSE deep fields*. A&A, 631, A87.

Vogelsberger M., Nelson D., Pillepich A. et al., 2020. *High-redshift JWST predictions from IllustrisTNG: dust modelling and galaxy luminosity functions*. Monthly Notices of the Royal Astronomical Society, 492, 4, 5167–5201. ISSN 0035-8711.

Wang T., Schreiber C., Elbaz D. et al., 2019. *A dominant population of optically invisible massive galaxies in the early Universe*. Nature, 572, 7768, 211–214.

Weinzirl T., Jogee S., Conselice C.J. et al., 2011. *Insights on the Formation, Evolution, and Activity of Massive Galaxies from Ultracompact and Disky Galaxies at z = 2-3*. ApJ, 743, 87.

Wellons S., Torrey P., Ma C.P. et al., 2016. *The diverse evolutionary paths of simulated high-z massive, compact galaxies to z = 0*. MNRAS, 456, 1, 1030–1048.

White S.D.M. & Frenk C.S., 1991. *Galaxy Formation through Hierarchical Clustering*. ApJ, 379, 52.

Whitney A., Conselice C.J., Bhatawdekar R. et al., 2019. *Unbiased Differential Size Evolution and the Inside-out Growth of Galaxies in the Deep CANDELS GOODS Fields at 1 ≤ z ≤ 7*. ApJ, 887, 2, 113.

Whitney A., Conselice C.J., Duncan K. et al., 2020. *Surface Brightness Evolution of Galaxies in the CANDELS GOODS Fields up to z ~ 6: High-z Galaxies Are Unique or Remain Undetected*. ApJ, 903, 1, 14.

Wilkins S.M., Bunker A., Coulton W. et al., 2013. *Interpreting the observed UV continuum slopes of high-redshift galaxies*. MNRAS, 430, 4, 2885–2890.

Wilkins S.M., Bunker A.J., Ellis R.S. et al., 2010. *Probing ~L_* Lyman-break galaxies at z ~ 7 in GOODS-South with WFC3 on Hubble Space Telescope*. MNRAS, 403, 2, 938–944.

Williams R.E., Blacker B., Dickinson M. et al., 1996. *The Hubble Deep Field: Observations, Data Reduction, and Galaxy Photometry*. AJ, 112, 1335.

Windhorst R.A., Taylor V.A., Jansen R.A. et al., 2002. *A Hubble Space Telescope Survey of the Mid-Ultraviolet Morphology of Nearby Galaxies*. ApJS, 143, 1, 113–158.